



저작자표시-비영리-변경금지 2.0 대한민국

이용자는 아래의 조건을 따르는 경우에 한하여 자유롭게

- 이 저작물을 복제, 배포, 전송, 전시, 공연 및 방송할 수 있습니다.

다음과 같은 조건을 따라야 합니다:



저작자표시. 귀하는 원저작자를 표시하여야 합니다.



비영리. 귀하는 이 저작물을 영리 목적으로 이용할 수 없습니다.



변경금지. 귀하는 이 저작물을 개작, 변형 또는 가공할 수 없습니다.

- 귀하는, 이 저작물의 재이용이나 배포의 경우, 이 저작물에 적용된 이용허락조건을 명확하게 나타내어야 합니다.
- 저작권자로부터 별도의 허가를 받으면 이러한 조건들은 적용되지 않습니다.

저작권법에 따른 이용자의 권리는 위의 내용에 의하여 영향을 받지 않습니다.

이것은 [이용허락규약\(Legal Code\)](#)을 이해하기 쉽게 요약한 것입니다.

[Disclaimer](#)

공학박사 학위논문

상분리를 고려한 고분자
나노복합재의 형상기억 거동에 대한
메조스케일 시뮬레이션 기반
멀티스케일 해석

**Mesoscale simulation-based multiscale analysis of
shape memory behavior of polymer nanocomposites
considering phase separation**

2023년 8월

서울대학교 대학원

기계항공공학부

박 성 우

상분리를 고려한 고분자 나노복합재의
형상기억 거동에 대한 메조스케일
시뮬레이션 기반 멀티스케일 해석

**Mesoscale simulation-based multiscale analysis of shape
memory behavior of polymer nanocomposites considering
phase separation**

지도교수 이 윤 석

이 논문을 공학박사 학위논문으로 제출함
2023년 4월

서울대학교 대학원
기계항공공학부
박 성 우

박성우의 공학박사 학위논문을 인준함
2023년 6월

위 원 장 _____ 양 진 규 _____ (인)

부위원장 _____ 이 윤 석 _____ (인)

위 원 _____ 김 태 용 _____ (인)

위 원 _____ 양 승 화 _____ (인)

위 원 _____ 신 현 성 _____ (인)

Abstract

Shape-memory polyurethane is a promising material that undergoes large reversible deformation in response to external heat, and includes a urethane bond inside the polymer structure. These polymer materials can be applied to diverse applications, including sensors, actuators, and biomaterials, owing to their cost-effectiveness, lightweight nature, high strain capacity, and ease of processing. In addition, studies on the design of nanocomposites with nanoparticles added to compensate for the low mechanical properties of pure polymer materials are also being actively conducted.

In order to obtain the thermal response shape memory effect of polyurethane nanocomposites, two structural conditions are required: a net point and a molecular switch. The hard segment, which remembers its original shape through physical entanglement, covalent bonding, or cross-linking, acts as a netpoint, and the flexible soft segment, which recovers its shape through a phase change in which polymer crystallization occurs at a transition temperature, acts as a molecular switch. Phase separation occurs between the two segments due to inherent incompatibility, and the microstructure change according to the ratio greatly affects the behavior of the polymer system. In addition, the clustering phenomenon of nanoparticles due to the chemical dissimilarity between the polymer matrix and the nanoparticles has been attention as a challenge to overcome to improve the mechanical properties of nanocomposites.

Atomistic simulation models that analyze the structure-property relationship of polymer systems or simulation methodologies that analyze mechanical properties according to the distribution of nanoparticles have been studied for a long time, but there are limitations in simulating and designing the behavior of actual nanocomposites. Motivated by this, this paper proposes a design method that comprehensively simulates the polymer crystallization, phase separation behavior, and nanoparticle distribution analysis of shape-memory polyurethane nanocomposites. In this study, a multi-scale analysis from the molecular dynamics level to the continuum level was performed through mesoscale simulations.

In this study, a CG MD model was developed to overcome the scale issues of existing molecular dynamics models. The polymer crystallization and shape memory cycles were simulated at the mesoscale level through a bead model to analyze the thermo-mechanical properties of polyurethane and the effect of adding nanoparticles according to the ratio of each segment in the polymer. This model model was verified by qualitatively and quantitatively comparing the thermo-mechanical trends according to the temperature and molecular composition reported in the experiment.

In addition, a dissipative particle dynamics simulation model was constructed to analyze the phase separation and nanoparticle distribution of polyurethane nanocomposites. Using the solubility of each material calculated at the molecular level as a parameter of the simulation, the phase shape of the polymer and the actual nanoparticle distribution of the nanocomposite according to the segment ratio were accurately predicted. In addition, surface treatment materials were introduced into

the silica nanoparticles to design an optimal nanoparticle distribution.

A continuum model that reflects the geometry obtained through the phase separation simulation of the polyurethane nanocomposite was constructed. In order to predict mechanical properties according to the degree of dispersion of nanoparticles, a finite element-based homogenization technique was introduced, and this paper presented it as a design methodology capable of designing various types of nanocomposites.

Through the mesoscale simulation-based multiscale analysis method presented in this paper, it is expected that more research will be conducted in the future to be used in actual nanocomposite design and application to obtain target properties.

Keyword : Shape-memory polyurethane, Nanocomposites, Coarse-grained molecular dynamics, Mesoscale simulation, Dissipative Particle Dynamics, Nanoparticle surface treatment, Finite element homogenization

Student Number : 2017-23073

Table of Contents

Abstract	i
Contents	iv
List of Figures	vii
List of Tables	xiv
Chapter 1. Introduction	18
1.1 Shape-memory polyurethane (SMPU) nanocomposites	18
1.2 Issues and Challenges of conventional computational models on design of SMPU nanocomposites	22
1.3 Mesoscale-based multiscale analysis strategy	26
1.4 Thesis Outline	29
Chapter 2 . Shape-memory behaviors of SMPU nanocomposites.....	31
2.1 Coarse-grained (CG) modeling of SMPU–Silica nanocomposites	31
2.1.1 Iterative Boltzmann inversion (IBI) method.....	32
2.1.2 CG modeling for thermoplastic polyurethane copolymer .	35

2.1.3	CG modeling for silica nanoparticle	41
2.2	Effect of molecular compositions on thermo-mechanical behaviors of pristine SMPU	48
2.2.1	Crystallinity.....	49
2.2.2	Melting temperature.....	52
2.2.3	Mechanical behaviors	52
2.2.4	Shape-memory properties	58
2.3	Effect of incorporation of silica nanofiller.....	67
2.3.1	SMPU microstructure on silica surface	67
2.3.2	Effect of silica nanoparticle content.....	72
Chapter 3 . Phase separation behaviors of SMPU.....		83
3.1	Dissipative particle dynamics (DPD) simulation	84
3.2	Derivation of solubility parameters for SMPU copolymer.....	87
3.3	Morphologies of phase-separated SMPU	91
Chapter 4 . Multiple phase separation behaviors of SMPU – Silica nanocomposites		99
4.1	Morphologies of phase-separated SMPU nanocomposites.....	99
4.1.1	Mixing energy and Flory-Huggins parameters between silica nanoparticle and polymer.....	99
4.1.2	Nanoparticle clustering density.....	103
4.2	Effect of silica nanoparticle surface treatment.....	110

4.3	Multiscale continuum model for mechanical properties.....	120
4.3.1	Multiscale homogenization modeling and verification....	120
4.3.2	Development of interphase for nanoparticulate agglomeration effect	124
4.3.3	Reinforcement effect of anisotropic nanofiller	131
Chapter 5 . Conclusions		140
Bibliography.....		142
국문 요약		159

List of Figures

Figure 1.1	Mechanism of shape memory behavior of SMPU.	19
Figure 1.2	Mesoscale simulation-based strategy for multiscale analysis of SMPU nanocomposites.	29
Figure 2.1	Chemical structures and bead-mapping of the SMPU copolymer.	36
Figure 2.2	Atomistic and coarse-grained (CG) MD models of the SMPU reference unit cell.	37
Figure 2.3	Example of the bond length distribution obtained from the AA reference model at 300 K and corresponding CG potential energy curve derived from the Boltzmann inversion.	38
Figure 2.4	Example of the bending angle distribution obtained from the AA reference model at 300 K and corresponding CG potential energy curve derived from the Boltzmann inversion.	38
Figure 2.5	The process of RDF converging to the target RDF through the IBI equation.	40
Figure 2.6	Comparison between the target RDF obtained through the AA	

	reference model and the RDF obtained through the CG model where the IBI process was completed.	41
Figure 2.7	Core-shell bead mapping strategy for CG model of silica nanoparticle.	42
Figure 2.8	AA and CG MD configurations of the referenc unit cells for deriving CG potentials (a) between SMPU matrix and silica nanoparticle, and (b) between silica nanoparticles.	43
Figure 2.9	Results of bond length distribution and derived CG potential energy of silica nanoparticle (Co-Co, Co-S, S-S).	44
Figure 2.10	Results of bending angle distributions and derived CG potential energies of silica nanoparticle.	44
Figure 2.11	Comparisons between the target RDFs and CG RDFs (IBI-PC completed) for matrix-naniparticle interactions obtained from the reference unit cells (Figure 2.8a).	46
Figure 2.12	Comparison between the target RDFs and CG RDFs (IBI-PC completed) for interparticle interactions obtained from the reference unit cells (Figure 2.8b), and the corresponding CG nonbonded energy curves.	47
Figure 2.13	A depiction of the reference axis and direction vector within the polymer, which were used to define the crystallinity in the CG model.	50

Figure 2.14	Crystallinity of the pristine SMPU copolymers with various hard-segment contents (HSCs) during the 80 ns of relation at 300 K.	51
Figure 2.15	CG MD configurations of semi-crystalline SMPU with (a) HSC = 15 wt.% , (b) HSC = 15 wt.% , and (c) HSC = 32 wt.% and their specific volume change during the heating-up simulation.	53
Figure 2.16	CG configurations of PU15 (HSC = 15 wt.%) undergoing uniaxial tensile deformation at (a) T=300 K and (b) 410 K. .	54
Figure 2.17	(a) Crystallinity and orientational order parameter of PU15 (HSC: 15 wt.%) under the uniaxial tensile test at T=300 K and 410 K. (b) RDF of the hard segment beads with different HSCs at T=410 K.....	56
Figure 2.18	Elastic modulus results of the SMPU copolymers according to HSCs and external temperatures.....	58
Figure 2.19	CG simulation process of the 4-step shape-memory thermo-mechanical cycle.....	60
Figure 2.20	3-D plot (strain-temperature-crystallinity) of the SMPU with HSC = 15 wt.% during the 4-step thermo-mechanical shape memory cycles.....	61
Figure 2.21	Shape-memory 3-D plots of the SMPU with three different	

	HSCs (15, 45, and 70 wt.%).	62
Figure 2.22	Changes in the radius of gyration (R_g) of the hard segment during shape recovery.	66
Figure 2.23	Changes in the mean square displacement (MSD) in the loading direction (x-axis) of each segment of the SMPU copolymer during shape recovery.	66
Figure 2.24	CG configurations of the SMPU nanocomposites with different HSCs (15, 32, 50, 70 wt.%) containing single silica nanoparticles with a radius of 30 Å	67
Figure 2.25	Radial density of the SMPU matrix and the high-density interphase region.	68
Figure 2.26	S value of each bead of SMPU matrix in PU15/Silica nanocomposite model. The average S value of the total matrix is 0.451, and the average S value of the 10 Å thick region around the silica nanoparticle is 0.231.	70
Figure 2.27	Comparisons between radial crystallinity distributions of the SMPU from the center of unitcell for pristine SMPU and from the center of the nanoparticle for SMPU/Silica nanocomposites.	71
Figure 2.28	Changes in fractional free volume (FFV) during shape-memory cycles for silica content 3 wt.% and 15 wt.% of the (a) PU15, (b)	

	PU32, and (c) PU50 nanocomposites.	75
Figure 2.29	Formation of free volume by nanoparticles in semi-crystalline polymer chains.....	77
Figure 2.30	Nanoparticle agglomeration according to silica content and consequent formation of vacancy zone.	77
Figure 2.31	Probability distribution of $R_{Silica-Silica}$ (the distance between silica nanoparticles) for silica content (a) 6 wt.% and (b) 15 wt.% in undeformed and deformed shapes.....	78
Figure 2.32	(a) Comparison between the original shape and recovered shape of PU15 and PU15 with 15 wt.% of silica. (b) Changes in the mean square displacement (MSD) in the loading direaction (x-axis) of the hard segment of PU50/Silica nancomposites.	81
Figure 3.1	Atomistic configurations of pure MDI and PEO MD unit cells. A detailed information is listed in Table 3.1.	88
Figure 3.2	Modelling of the SMPU copolymer chains for DPD simulations.	92
Figure 3.3	Phase separation morphology of PU15 according to time step by DPD simulation. Yellow bead represents MDI bead and green bead represents PEO bead. To illustrate the phase domain more effectively, PEO beads are hidden from the unit cell.	93
Figure 3.4	Hard domain connections and distributions of the SMPU	

	according to the HSCs (15, 21, 32, 45, and 50 wt.%) in $2 \times 2 \times 2$ periodic unit cells.	95
Figure 3.5	Summarization of the architectural evolution of phase morphologies according to HSC of the SMPU.	98
Figure 4.1	Molecular unit segments constituting each bead of DPD. ..	100
Figure 4.2	Multiple phase separation morphology of PU15/Silica nanocomposite according to time step by DPD simulation. Yellow bead represents MDI bead, green bead represents PEO bead, and navy beads represent silica Core beads.. ..	105
Figure 4.3	Final snapshots of DPD simulation results for different HSCs and silica nanoparticle contents (Silica with only Core beads).	106
Figure 4.4	Phase domain morphologies of the SMPU matrix and silica nanoparticle distributions (10 wt.%) for HSC (a) 15 wt.%, (b) 32 wt.%, and (c) 50 wt.% in $2 \times 2 \times 2$ periodic unit cells.	108
Figure 4.5	Clustering density results as a function of HSC at different silica contents.	110
Figure 4.6	Chemical structure of silica surface treatment materials (a) silanol groups (Shell bead), (b) polydimethylsiloxane (PDMS bead), (c) Octylsilane (OS bead), and (d) 3-aminopropyltrimethoxysilane (APTS bead).	111

Figure 4.7	DPD modeling of silica surface treatment of SMPU/silica nanocomposites.	114
Figure 4.8	Distributions of silica nanoparticles as a result of DPD simulation according to HSC (a) 15 wt.%, (b) 32 wt.%, and (c) 50 wt.% and silica surface treatment of SMPU/Silica nanocomposites.	115
Figure 4.9	Clustering density change according to nanoparticle surface treatment of SMPU/Silica nanocomposites.	116
Figure 4.10	Nanoparticle distribution improvement effect by optimal silica surface treatment in (a) PU15 and (b) PU50.	119
Figure 4.11	Configurations of DPD model of PU15/Silica nanocomposites and equivalent finite element model: (a) silica 3 wt.%, (b) silica 6 wt.%, and (c) silica 10 wt.%.	121
Figure 4.12	Homogenized (a) Young's modulus and (b) shear modulus of neat SMPU and nanocomposites with the silica contents without considering interphase.	123
Figure 4.13	Equivalent finite element model for 3-phase (matrix, particle, and interphase) systems.	127
Figure 4.14	Changes of particle distribution and interphase area in 3-phase FEM model according to the surface treatment for (a) PU15, (b) PU32, and (c) PU50.	129

Figure 4.15	Homogenized Young's modulus of SMPU nanocomposites and volume fraction of interphase region considering interphase effect and silica surface treatment for (a) PU15, (b) PU32, and (c) PU50.	130
Figure 4.16	DPD modeling of silica surface treatment of cylindrical nanofiller.	131
Figure 4.17	Clustering density change of cylindrical nanofiller.	133
Figure 4.18	Cylinder distribution improvement by optimal surface treatment in (a) PU15 and (b) PU50.	134
Figure 4.19	Distributions of cylindrical nanofillers, and corresponding volume fraction of interphase (V_{int}) and mechanical properties for (a) PU15 and (b) PU50.	134
Figure 4.20	(a) Bridging architectural morphology of cylindrical nanofillers in lamellar structure, and (b) $3 \times 2 \times 2$ periodic unit cells. .	136
Figure 4.21	(a) Distributions of cylindrical nanofillers, and corresponding volume fraction of interphase (V_{int}) and mechanical properties for PU32 nanocomposites, and (b) Anisotropy of nanocomposites.	139

List of Tables

Table 2.1	Bond length CG potential energy coefficients for SMPU copolymer.	39
Table 2.2	Bending angle CG potential energy coefficients for SMPU copolymer.	39
Table 2.3	Bond length CG potential energy coefficients for silica nanoparticle.	45
Table 2.4	Bending angle CG potential energy coefficients for silica nanoparticle.	45
Table 2.5	Information on the mesoscale CG models with different HSCs. All models have the same number of soft-segment beads = 8320 beads.	49
Table 2.6	Shape-memory performances and crystallinity during the shape-memory cycle.	63
Table 2.7	Modeling of the mesoscale CG SMPU/Silica nanocomposites.	72
Table 2.8	Shape-fixity ratio (R_f) of the SMPU/Silica nanocomposites accordint to HSC (15, 32, and 50 wt.%) and silica content (3, 6,	

	10, 15 wt.%).	73
Table 2.9	Shape-recovery ratio (R_r) of the SMPU/Silica nanocomposites accordint to HSC (15, 32, and 50 wt.%) and silica content (3, 6, 10, 15 wt.%).	73
Table 2.10	Fractional free volume (FFV) change during the shape-memory thermo-mechanical cycle.....	75
Table 2.11	Characterization of the probability distribution (Figure 2.30) of $R_{Silica-Silica}$	79
Table 3.1	DPD bead modeling with similar molecular volume for each segment of the SMPU.....	87
Table 3.2	Information on the AA MD unit cells of each segment component of the SMPU copolymer (see atomistic configuration in Figure 3.1).....	88
Table 3.3	Solubility parameter (δ) of pure MDI and PEO system cacluated from AA MD simulations.	90
Table 3.4	Repulsion parameter (a_{ij}) between SMPU DPD beads.	90
Table 3.5	Information on the reduced units of DPD simulation.....	91
Table 4.1	DPD bead modeling of silica nanoparticle system.	100
Table 4.2	Flory-Huggins parameter (χ_{ij}) between DPD beads of SMPU/Silica nanocomposites.	102

Table 4.3	Repulsion parameter (a_{ij}) between DPD beads of SMPU/Silica nanocomposites.	103
Table 4.4	Flory-Huggins parameter (χ_{ij}) for silica surface treatment materials.	112
Table 4.5	Repulsion parameter (a_{ij}) for silica surface treatment materials.	112
Table 4.6	Young's modulus and shear modulus of SMPU/Silica nanocomposites with the Mori-Tanaka model (Unit: MPa).123	
Table 4.7	Young's modulus and shaer modulus of neat SMPU amd nancomposites obtained from CG MD and Mori-Tanaka models.	125
Table 4.8	Properties of interphase region for different HSCs of the SMPU.	127

Chapter 1

Introduction

1.1 Shape-memory polyurethane (SMPU) nanocomposites

Shape-memory polymer (SMP) is an intelligent material that exhibit responses to external stimuli like heat, light, moisture, and electricity [1–3]. In comparison to shape-memory alloys, offer several benefits such as being biocompatible, cost-effective, lightweight, and having high strain capacity and processability. As a result, SMPs find wide applications in biomaterials, sensors, micro-actuators, and textile fibers [3–5]. Heat-induced SMPs, which are responsive to heat, are particularly popular due to their simplicity in operation. To achieve the desired thermo-responsive shape-memory effect, two structural conditions are necessary: a netpoint and a molecular switch [6]. The netpoint, responsible for memorizing the original shape, can be achieved through physical entanglement, covalent crosslinking, or

physical crosslinking. The molecular switch, also known as a switching segment, initiates shape recovery at the transition temperatures like glass-transition temperature or melting temperature. One example of a thermo-responsive SMP is the semi-crystalline thermoplastic polyurethane (TPU), which is a physically crosslinked copolymer with the melting temperature (T_m) as the transition temperature [7–9]. The shape-memory polyurethane (SMPU) contains a urethane linkage formed by combining an N–C–O bonded isocyanate group with a polyol containing an OH group. In the SMPU copolymers developed in this study, the isocyanate groups with aromatic ring structures and the urethane linkages capable of hydrogen bonding create a rigid hard-segment functioning as the netpoint. The soft-segment polyether (or polyester) diol forms a flexible chain structure that can undergo polymer crystallization (Figure 1.1).

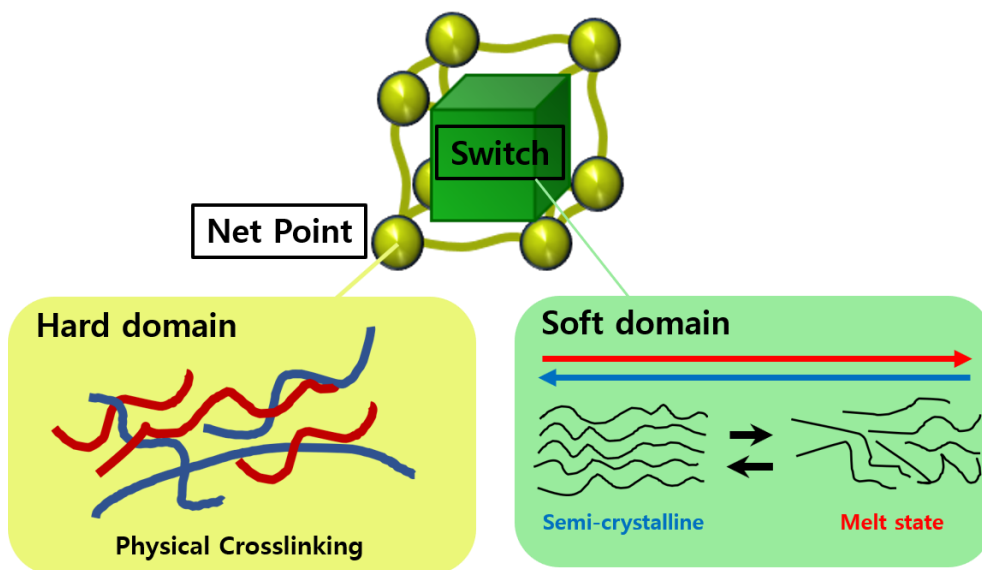


Figure 1.1 Mechanism of shape memory behavior of SMPU.

Compared to other SMPs, the polymer chains of T_m -dependent SMPU copolymers exhibit better mobility at temperatures above T_m , and the melting temperature can be easily adjusted by modifying the structures or composition [10,11]. As SMPU copolymers have a phase-separated (hard-soft) copolymer structure, the microscale features can significantly impact the macroscopic characteristics of thermo-responsive actuators, such as mechanical rigidity, operation temperature, and final deformed shape. Hence, the ratio of each segment in each polymer chain plays a crucial role in SMPU material design. Several researchers have studied the effects of hard-segment content (HSC) in polymer chains on the morphology and shape-memory behavior of SMPU copolymers [3,12]. For instance, Lin et al. [12] conducted experimental investigations on the effect of HSC on the thermodynamic properties and shape-memory behavior of polyurethanes, while Li et al. [13] explored the effects of HSC and the length of soft-segment on the crystallinity and morphology of dual-segment polyurethanes.

Despite the wide range of possible shapes that shape-memory polymers (SMPs) can adopt, they have significant limitations including low stiffness and tensile strength, restricted actuation due to heat-treatment, slow response time, low recovery stress, and limited recovery at physiological temperatures [14,15]. Similarly, shape-memory polyurethane (SMPU) also has drawbacks such as low stiffness [16,17], weak recovery performance [18-20], and limited responsiveness to electrical, light, or magnetic stimuli.

To overcome these limitations, researchers have turned to shape-memory

polymer nanocomposites by incorporating one or more types of nanofillers, such as nanotubes, nanofibers, nanospheres, or nanorods, into the polymer matrix to improve shape-memory properties, recovery stress, or to modify the operating temperature and expand the range of actuation [1,6]. However, the introduction of nanofillers into SMPs can present drawbacks, notably in the disruption of the polymer networks that govern the shape memory capabilities, particularly at elevated filler concentrations. Achieving the appropriate equilibrium between recovery stress and recovery strain when using fillers remains an active area of research. Polyurethane and its composites filled with particles have been popular choices for SMPs due to their versatility and ease of preparation. Some studies [21,22] have reported negative impacts of fillers on shape memory properties in composites, while others [16,23-25] have shown improved mechanical properties and recovery ratios with the incorporation of nanofillers, such as SiC or carbon nanotubes.

Therefore, researches on the relationship between the structure and properties of SMP nanocomposites and the cutting-edge development are steadily attracting attention as an important issue. Therefore, through comprehending the basic correlation between the structure and properties of SMPU nanocomposites and the effect of various nanofillers on SMP properties, the development of a computational model that can be used to design, develop, and program SMPU systems more accurately and precisely is essential. In addition, we need to focus on strategies that can uniformly disperse nanofillers to improve the properties of nanocomposites, and modeling methods are needed to design shape-memory polymer systems and devices

with superior performance.

1.2 Issues and Challenges of conventional computational models on design of SMPU nanocomposites

The all-atom (AA) molecular dynamics (MD) simulation has been extensively utilized by researchers to investigate the thermo-mechanical properties or molecular mechanisms of SMPs without the need for time-consuming experiments. However, conventional AA MD models have limitations in describing the global motion of polymer chains and mesoscopic phenomena associated with shape-memory behavior in semi-crystalline copolymers. Polymer chain crystallization, which involves complex and slow processes, is challenging to observe using AA MD simulations owing to the significant computational cost required for long polymer chains. This often results in only local ordering behavior being observable, or the need to use artificially pre-oriented models for polymer crystallization simulations [26,27]. Additionally, structural transitions may not occur adequately at high temperatures in conventional AA MD models due to the extremely fast heating rates applied. As a result, accurate prediction of transition behavior and switching temperature range is difficult. To address these challenges, it is necessary to accelerate polymer dynamics for the phase transition behaviors by reducing the number of degrees of freedom (DOFs) of the atomistic model [28,29].

Researchers have employed coarse-grained molecular dynamics (CG MD) simulations to address the scale restrictions of all-atom (AA) MD simulations when

investigating thermo-responsive shape-memory polymers (SMPs). [30-34]. For instance, Uddin et al. [30] developed a CG MD model for thermoplastic polyurethane (TPU) to determine its mechanical properties and explore the impact of hard segments on equilibrium structures. Abberton et al. [32] also developed a CG model for a generalized hard-soft copolymer system to replicate the glassy-transition and shape-memory performance, and customized shape-programming conditions to modify the recovery characteristics of heat-activated SMPs. These CG models have been useful in simulating the phase-separated morphology and thermodynamic behavior of copolymer-type SMPs and inducing shape recovery through the glassy-to-rubbery transition. However, challenges remain in obtaining a comprehensive description of the shape-memory cycle for semi-crystalline polymers at the mesoscopic level because the low level of polymer crystallization in longer chains requires a CG model that elaborately reflects the interaction at the atomistic level.

As mentioned above, the shape memory mechanism and structure-property analysis are required at the mesoscale level through the crystallization behavior of the soft segment, which acts as a switch, and the behavior of the hard segment, which serves as a netpoint. The SMPU chains lead to phase separation due to the intrinsic chemical dissimilarity between these two segments and has each domain. Therefore, not only understanding the behavior and molecular structure of each segment, but also understanding the phase structure of the system in the microdomain is essential for SMPU design. In some cases, the shape memory and mechanical properties of polymeric materials are greatly influenced by the degree of structural completeness

and phase separation. Therefore, understanding and optimizing this phase separation is very important to determine the performance of polymer systems. Zhang et. al. [120] introduced a styrene–butadiene–styrene (SBS) copolymer and poly(ϵ -caprolactone) (PCL) blend for its shape memory properties, and demonstrated the phase morphologies of the immiscible blend contributed to the shape recovery and fixing performances. The effect of phase separation is also very significant in the mechanical properties of polymer-based materials such as Mater-Bi type bioplastic [121], and various additives were tested to improve the miscibility and solubility between the gum rosin and its derivatives. The shape-memory behaviors and thermo-mechanical properties of SMPU are also affected by the phase separation morphology, which are in turn related to the HSCs.

Since AA MD simulation, which considers all atomic degrees of freedom and observes local motion, is not suitable for observing the phase separation behavior of the SMPU copolymer, a coarse-grained MD model should be used as well. At this time, the focus is on the polymer mixing phenomenon rather than the molecular behavior of each polymer chain. Therefore, it is efficient to use a CG model that reflects the solubility of each component in order to observe the phase separation behavior and phase morphology on the scale of tens of nanometers.

From the point of view of nanocomposites design, many multiscale computational models are also being developed to analyze nanocomposites in which nanoparticles are added to polymer materials [35-38]. The area of the polymer matrix surrounding the surface of filler is referred to as the interphase. The interactions in

this region influence the physical properties of the polymer nanocomposites. When the dimensions of the filler decrease to the nanometer scale, the interfacial interactions become more significant because nanoparticles exhibit a high surface area to volume ratio. [39].

Attaining a uniform distribution of nanofillers within polymer resins is of paramount importance processing nanocomposites. The even distribution of nanofillers is crucial for attaining ideal multifunctional characteristics, particularly when dealing with low concentrations [40,41]. When filler particles agglomerate, they obstructs the effective penetration and crystallization of polymer segments, and also restrict the movement of nanoparticles [42-44]. As a consequence of this inadequate penetration, a void area forms within the clusters, which is widely believed to negatively impact the mechanical properties in general.

The problem of interphase zone degradation caused by agglomeration is important, but traditional micromechanics models cannot account for how agglomeration affects composite properties overall. As a solution, a new method called inverse multiscale modeling has been introduced and utilized to explore different aspects of nanocomposites. This approach employs molecular dynamics simulation alongside continuum modeling techniques like micromechanics solutions or finite element methods to study characteristics such as elasticity, thermoelasticity, and thermal conductivity [45,46]. Furthermore, the effective creation of interfacial regions is restricted by substantial potential barriers caused by repulsive forces between neighboring nanoparticles [47,48]. As a result, there are overlapping and

gallery regions with lower densities than bulk polymers. To address this, Baek et al proposed a modified interphase model that recognizes the variation in density between the conventional high-density interphase without overlapping and the overlapping interphase [47]. To analyze the mechanical, thermal, or electrical properties of nanocomposites in terms of the degree of nanoparticle agglomeration, some research suggests employing a multiscale framework that accounts for the properties of the nanoscale interphase region. This model does not reveal how the actual distribution of nanoparticles occurs through the chemical interaction between the matrix and nanoparticles in the fabrication of nanocomposites. In addition, from the point of view of complete nanocomposite design, they do not suggest a chemical treatment method to improve the nanoparticle agglomeration phenomenon and a method to improve the properties of the nanocomposite accordingly. To solve this problem, multi-scale analysis through expansion from atomistic level to mesoscale level is necessary, rather than the existing multi-scale framework leading directly from the molecular dynamics to continuum modeling, and this work was performed in this study.

1.3 Mesoscale-based multiscale analysis strategy

In this computational study, as shown in Figure 1.2, a sequential multiscale framework was proposed, involving all-atom molecular dynamics (AA MD), coarse-grained MD (CG MD), dissipative particle dynamics (DPD), and finite element method (FEM).

To bridge the chemical interaction in atomistic level with the design of polymer nanocomposites in continuum scale, we established a mesoscale simulation-based multiscale strategy for SMPU nanocomposites. Here, mesoscale simulation refers to CG MD and DPD models that treat multiple atoms as one bead, reducing the degree of freedom and dramatically increasing the time/length scale. At this time, to improve the dependability of the constructed multiscale model, scale bridging was conducted, involving the transfer of physical properties from the lower scale to the upper scale. First, we developed a coarse-grained MD model by using the iterative Boltzmann inversion (IBI) technique. At this time, a reference atomistic model was established, and the CG model was upscaled to equally simulate the structural conformations, radial distribution density (RDF), and density of the polymer chain at the atomistic level. The phase transition (polymer crystallization) of SMPU was simulated through the developed CG model, and the resulting thermo-mechanical properties and shape memory mechanism were investigated. In addition, the effect of nanoparticles on the shape-memory performance was investigated through the addition of silica nanoparticles.

Next, the phase separation of SMPU nanocomposites was investigated through the DPD model. Here, DPD is an extended scale that can observe phase architectural evolution in tens of nanometers by treating larger atomistic units as beads than general CG models developed through the IBI method. DPD simplifies potential energy between beads and focuses only on phase mixing between different components through relatively soft nonbonded repulsion. Here too, the difference in

solubility and mixing energy between each component calculated through AA MD is upscaled as a variable for calculating the DPD repulsion parameter. Through the developed DPD model, the two-phase morphology according to the HSC of SPMU was investigated. In addition, by adding silica nanoparticles, the distribution of nanoparticles in the polymer matrix could be derived through multiple phase separation. Additionally, the nanoparticle clustering behavior was controlled by surface treatment of silica. The presented study can provide a guideline for designing uniform distribution of nanoparticles to improve the electrical, mechanical, and thermal characteristics of nanocomposites. The geometry of the nanocomposite derived through DPD is upscaled to the FEM mesh at the continuum scale. This overcomes the limitations of conventional nanocomposite theoretical models assuming well-dispersed nanoparticles or existing multi-scale models that derive nanocomposite properties according to user-controlled particle agglomeration.

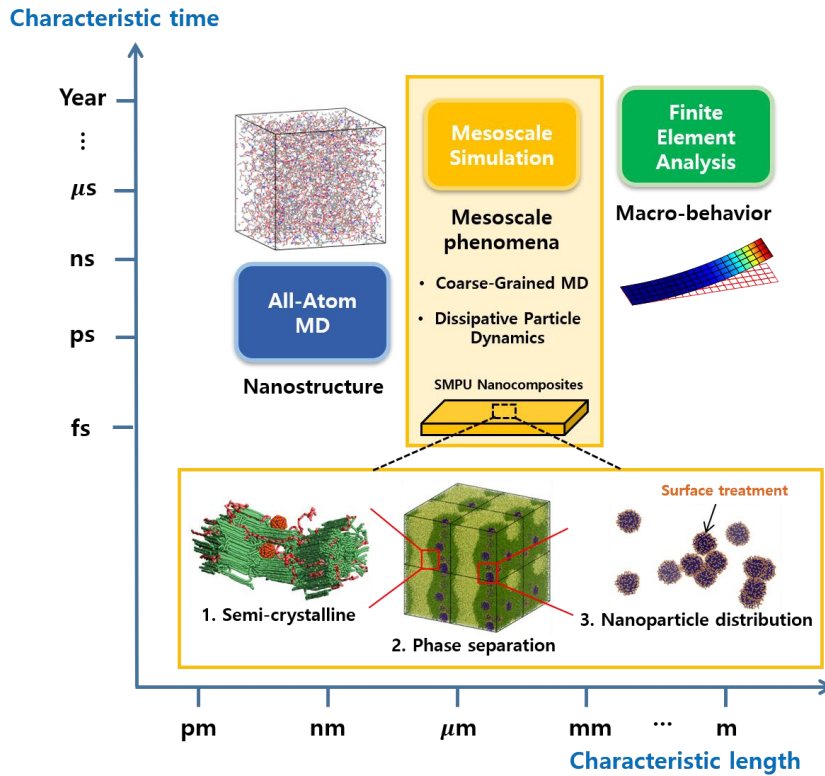


Figure 1.2 Mesoscale simulation-based strategy for multiscale analysis of SMPU nanocomposites.

1.4 Thesis Outline

The dissertation is organized as follows; In Chapter 2, the basic mesoscale behavior of shape-memory polyurethane (SMPU) nanocomposites is described. A coarse-grained MD model was built using the iterative Boltzmann inversion (IBI) technique to investigate the molecular structure of each segment of the SMPU. And the thermo-mechanical properties and shape-memory performance according to the HSC are described. Furthermore, changes in microstructure and shape-memory

behavior are shown with the addition of silica nanoparticles. Chapter 3 focuses on the phase separation of the SMPU copolymer by building a dissipative particle dynamics (DPD) model. By introducing the solubility parameter calculated through AA MD, we predict the architectural evolution of the phase domain according to the SMPU HSC. Chapter 4 shows the multiple phase separation of the SMPU/Silica nanocomposites considering the nanoparticle agglomeration in DPD simulation. Uniform distribution is obtained through surface treatment of silica nanoparticle, and the degree of improvement in nanoparticle distribution improvement is quantified through clustering density. Finally, finite element-based homogenization is combined with DPD resulting geometries to derive the mechanical properties of SMPU nanocomposites considering the interphase zone. The conclusions are given in Chapter 5.

Chapter 2

Shape-memory behaviors of SMPU nanocomposites

2.1 Coarse-grained (CG) modeling of SMPU–Silica nanocomposites

Coarse-grained molecular dynamics simulation is an efficient modeling method that enables simulation and analysis of desired mesoscale behavior or properties of polymer nanocomposite systems. This model plays a role of scale bridging for mesoscale phenomena that have limitations in interpretation with the existing full atomistic model and cannot be applied to the continuum theory. Coarse-grained models treat multiple atoms as a bead to dramatically increase the time scale and

length scale of computation. Existing all-atom MD has the advantage of precisely mimicking the local motion of a polymer nanocomposite through realistic molecular structure modeling, whereas the CG model implements the global motion of a polymer through a reduced degree of freedom, resulting in phase transition, phase separation, Mesoscale phenomena such as nanoparticle aggregation can be efficiently simulated. In order to build an accurate CG model, it is necessary to develop potential energy between the constituent beads that equally simulate the structure or physical properties of the all-atom model according to the desired analysis goal.

2.1.1 Iterative Boltzmann inversion (IBI) method

To create a CG model with fewer DOFs, a new set of potentials must be created between the beads. The energy of the entire bead system can be categorized into two parts: bonded energy and non-bonded energy.

$$\sum U_{CG} = \sum U_{CG}^{bonded} + \sum U_{CG}^{nonbonded} \quad (2.1)$$

First, the bonded potential is created to ensure that the bead model has the same conformational distribution as the reference AA MD model. Then, the non-bonded potential is derived using the Iterative Boltzmann Inversion (IBI) method to match the structural and thermodynamic properties, such as radial distribution function and density. This structure-based bottom-up approach is to accurately simulate the behavior of the SMPU-silica nanocomposite at the bead level. Similar optimization techniques have been used to link atomic and mesoscopic properties of various

polymeric molecules. [49-53].

Bonded potential can be divided into the energy associated with the bond length of adjacent two beads (l) and the bending-angle of adjacent three beads (θ). The probability distributions of the intramolecular conformations ($P(l)$ and $P(\theta)$) were obtained from the NVT trajectory of the reference model. The CG potentials ($U_{CG}^{bonded}(l)$ and $U_{CG}^{bonded}(\theta)$) can be derived from the obtained probability distribution via Boltzmann inversion :

$$\begin{aligned} U_{CG}^{bonded}(l) &= -k_B T \ln(P(l)/l^2) \\ U_{CG}^{bonded}(\theta) &= -k_B T \ln(P(\theta)/\sin\theta) \end{aligned} \quad (2.2)$$

where k_B is the Boltzmann constant, and T is the temperature. The bonded potentials, which depend on the bond length and bending angle, were calibrated using a technique called multi-centered Gaussian fitting method [33], expressed as:

$$\begin{aligned} U_{CG}^{bonded}(l) &= -k_B T \ln \left[\sum_{i=1}^n a_i \exp \left\{ - \left(\frac{l - l_i}{b_i} \right)^2 \right\} \right] \\ U_{CG}^{bonded}(\theta) &= -k_B T \ln \left[\sum_{i=1}^n a_i \exp \left\{ - \left(\frac{\theta - \theta_i}{b_i} \right)^2 \right\} \right] \end{aligned} \quad (2.3)$$

where l_i and θ_i represent the central positions of each Gaussian function, and a_i and b_i are coefficients. This method is more sophisticated in describing the multiple equilibrium states compared with just using a simple harmonic function.

The non-bonded potentials are created so that they can match the target radial distribution function (RDF) and density of the atomistic model at the reference temperature of 300K. The RDF is calculated using CG reference trajectories derived from all-atomistic MD simulations. An initial guess ($U_{CG,0}^{nonbonded}(r)$) for the non-

bonded potential is estimated by utilizing the target RDFs and employing Boltzmann inversion;

$$U_{CG,0}^{nonbonded}(r) = -k_B T \ln(g_{target}(r)) \quad (2.4)$$

where r is the distance between CG beads, and $g_{target}(r)$ is the target RDF. We used the IBI method to optimize the non-bonded potential energy between beads. The initial potential in the CG model did not match the target RDF, so we had to optimize the CG potential energy iteratively using a formula that included a constant value and the RDF from each iteration as follow:

$$U_{CG,i+1}^{nonbonded}(r) = U_{CG,i}^{nonbonded}(r) - \beta k_B T \ln\left(\frac{g_i(r)}{g_{target}(r)}\right) \quad (2.5)$$

We stopped the iteration process when the target function, which measures the degree of error with the target RDF, fell below a certain value. To calculate the target function, we followed the given formula.

$$f_{target} = \int_0^{r_c} \exp(-r) \{g_i(r) - g_{target}(r)\}^2 dr \quad (2.6)$$

where r_c is the cut-off distance, which is 20 Å in this study.

While the RDFs of the IBI-completed bead model matche the desired outcome well, the potential based on IBI alone is not enough to replicate the density of the AA reference model. As a result, an extra correction for pressure is required to achieve a density match [34]. To derive the pressure-corrected potential ($U_{CG}^{PC}(r)$), the following formula is used.

$$U_{CG}^{PC}(r) = U_{CG}^{nonbonded}(r) - \gamma k_B T \left(1 - \frac{r}{r_c}\right) \quad (2.7)$$

The process of adjusting the CG system continues repeatedly until its pressure

matches the desired pressure of 0.1 MPa.

2.1.2 CG modeling for thermoplastic polyurethane copolymer

Figure 2.1 represents the chemical structure of the SMPU copolymer adopted in this study, and the CG bead mapping is indicated. The copolymer is made up of urethane linkages formed by combining 4,4'-diphenylmethane diisocyanate (MDI) and poly (ethylene oxide) (PEO), where MDI forms the hard segment and PEO forms the soft segment. Various CG mapping schemes have been developed to describe the molecular interaction and structure of polyurethane- and polyurea-based materials. Agrawal and co-workers [49] used two types of beads to represent the hard and soft segments of oligomeric polyurea chains. Cui et al. [32] also used a two-bead system to study the mechanical properties of hard-soft copolymers. But it was found that using only two beads to represent the hard and soft segments is not sufficient to accurately replicate the strong adhesion between the hard segments induced by the hydrogen bonding between the urethane linkages. Zhang et al. [50] found that multiple bead types were necessary to accurately replicate the packing behavior and interaction characteristics of rigid biphenyl groups. Therefore, this study constructed a system with three different beads, with bead A representing one monomer of PEO, bead B representing the center part of the hard component, and bead C representing the remaining part of the benzenes and the urethane linkage. Beads A, B, and C correspond to 7, 13, and 10 atoms, respectively. Uddin et al. [30] also used three types of beads on thermoplastic polyurethane and were able to effectively observe

the phase transition behavior with their mesoscale model. So as to simplify the process of deriving the coarse-grained potential and mesoscale model, the chain extender between the hard groups was disregarded in their study.

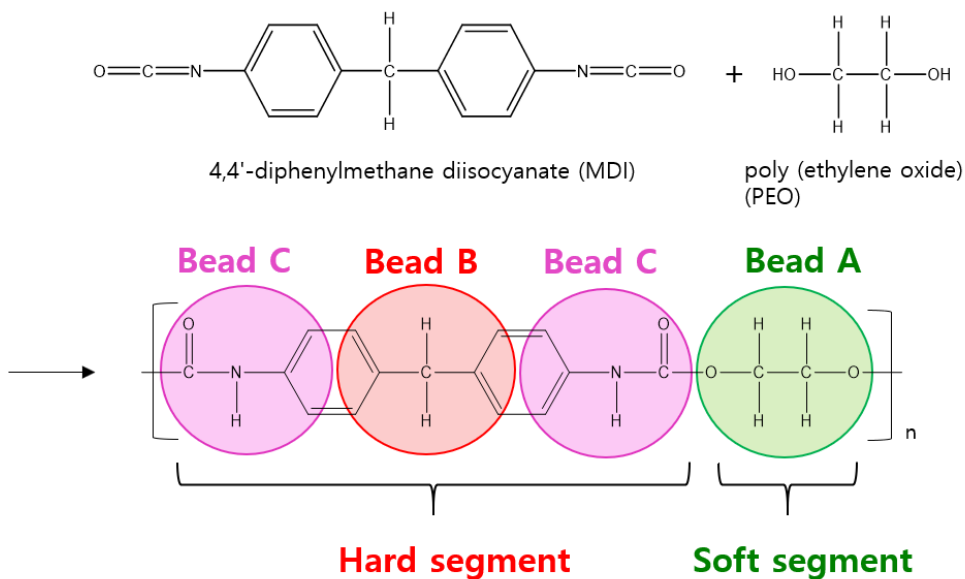


Figure 2.1 Chemical structures and bead-mapping of the SMPU copolymer.

We prepared a target reference structure of the SMPU to derive CG potentials by using the AA MD simulation as shown in Figure 2.2. We used the Theodorou-Suter [54] method of the Amorphous Cell Tools of Materials Studio 5.5 to create a unit cell made up of 80 polymer chains, each with a molecular weight of 1277.39g/mol and a hard-segment content of 65 wt.%. The LAMMPS [55] code developed by the Sandia National Laboratory was then used to relax the initial cell, with a polymer consistent force field (PCFF) [56] describing intra- and inter-

atomistic potentials. A cut-off distance of 9.5 Å was set for both non-bonded van der Waals and Coulombic interactions, utilizing a timestep of 1.0 fs and a dielectric constant value for the Coulombic interactions set to 1.0. To obtain clear peak values in radial distribution functions (RDFs), the reference AA model was equilibrated at high temperature ($T=550$ K) for 10 ns to avoid local minimization of the initial randomly generated polymer configuration., and then equilibrated for an additional 20 ns at 300 K and 0.1 MPa. Then, NVT ensemble was performed at 300 K for 2 ns to obtain structural properties through reference CG trajectories. Our methodology was similar to that of Agrawal et al. [49] who also equilibrated their system at an elevated temperature and then quenched it to 300 K.

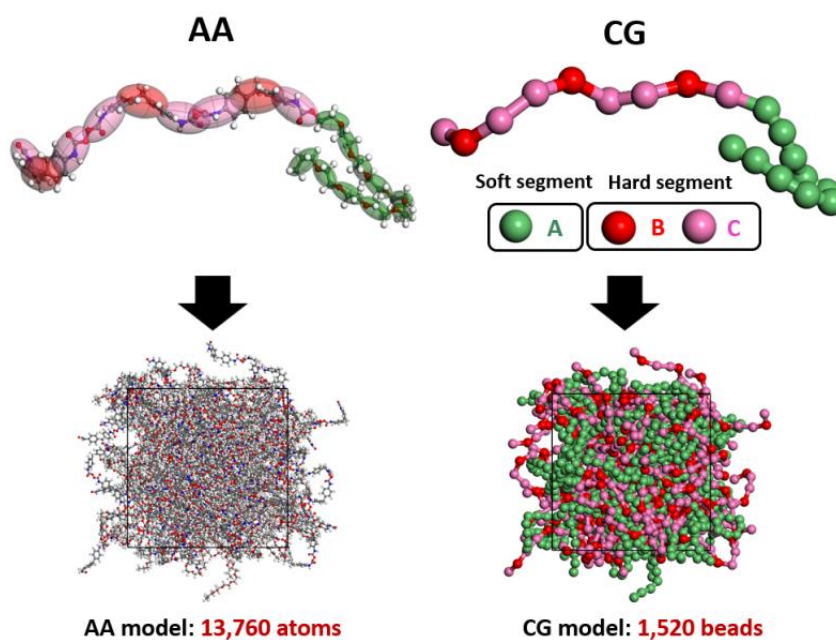


Figure 2.2 Atomistic and coarse-grained (CG) MD models of the SMPU reference unit cell.

The potential energy between the beads was developed through the process described in section 2.1.1. Examples of bond length and bending angle distributions are shown in Figures 2.3 and 2.4, respectively.

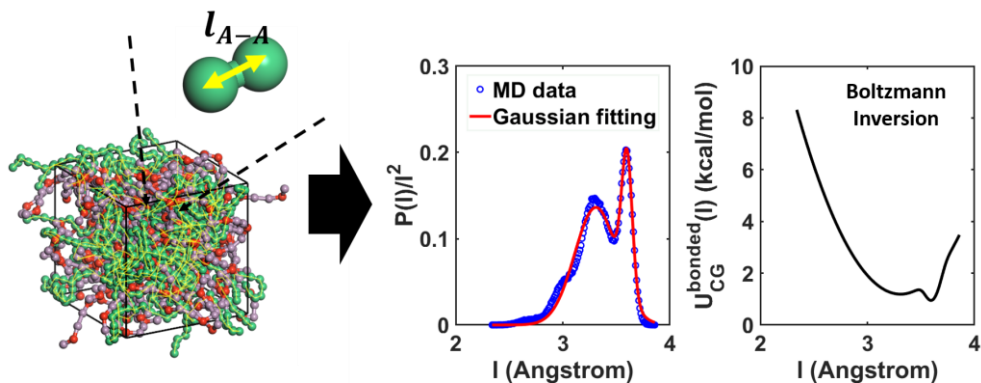


Figure 2.3 Example of the bond length distribution obtained from the AA reference model at 300 K and corresponding CG potential energy curve derived from the Boltzmann inversion.

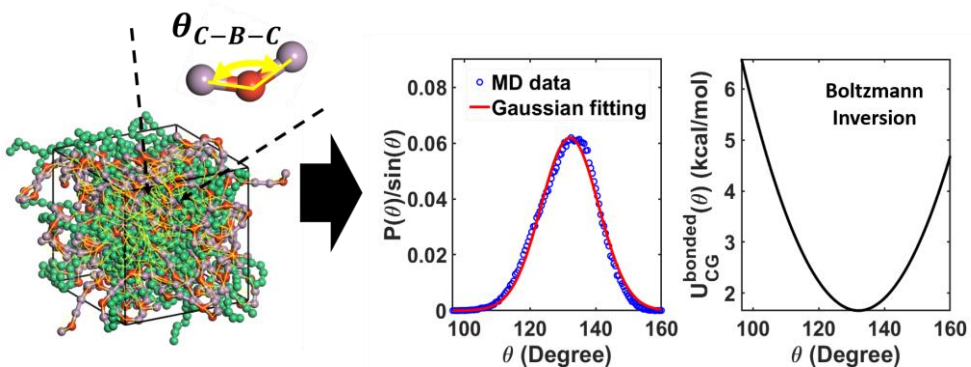


Figure 2.4 Example of the bending angle distribution obtained from the AA reference model at 300 K and corresponding CG potential energy curve derived from the Boltzmann inversion.

The MD data marked with a blue circle was fitted to a multi-centered Gaussian using a red line. Tables 2.1 and 2.2 contain coefficients for analytically parameterized bond

length and bending angle pairs, respectively. On the right, each CG potential obtained from the red line through Boltzmann inversion is shown by a black line. The CG potentials obtained through Boltzmann inversion are extrapolated by polynomial functions at both ends.

Table 2.1 Bond length CG potential energy coefficients for SMPU copolymer.

Bond length	a_1	b_1 [Å]	l_1 [Å]	a_2	b_2 [Å]	l_2 [Å]	a_3	b_3 [Å]	l_3 [Å]
A-A	0.157	0.070	3.600	0.136	0.281	3.310			
A-C	0.060	0.131	4.374	0.070	0.080	4.689	0.041	0.412	4.170
B-C	0.121	0.173	5.147						
C-C	0.048	0.158	5.412	0.039	0.273	4.917	0.030	0.144	4.514

Table 2.2 Bending angle CG potential energy coefficients for SMPU copolymer.

Bending angle	a_1	b_1 [°]	θ_1 [°]	a_2	b_2 [°]	θ_2 [°]	a_3	b_3 [°]	θ_3 [°]
A-A-A	0.134	13.79	179.5	0.019	18.97	160.5	0.014	36.26	140.5
B-C-A	0.297	18.62	179.5						
C-A-A	0.033	16.49	179.4	0.029	45.31	158.2			
C-B-C	0.062	12.37	132.1						
C-C-B	0.155	18.86	177.9	0.012	29.53	133.6	0.001	3.435	119.3

After applying all the derived bonded potentials to the bead system, the IBI procee begins. In this system, there are three types of beads, which necessitates six non-bonded potentials (A-A, B-B, C-C, A-B, B-C, C-A). Figure 2.5 shows the RDF

convergence process during IBI implementation, expressed as equation (2.5) in section 2.1.1. The comparison of the target radial distribution functions (RDFs) from the all-atom reference model and the IBI-completed CG model is shown in Figure 2.6, along with the final target function values of each bead pair. The density of the CG system was 1.211 g/cc at 300 K with the additionally the pressure-corrected potentials, which is in precise agreement with the atomistic model's density of 1.210 g/cc.

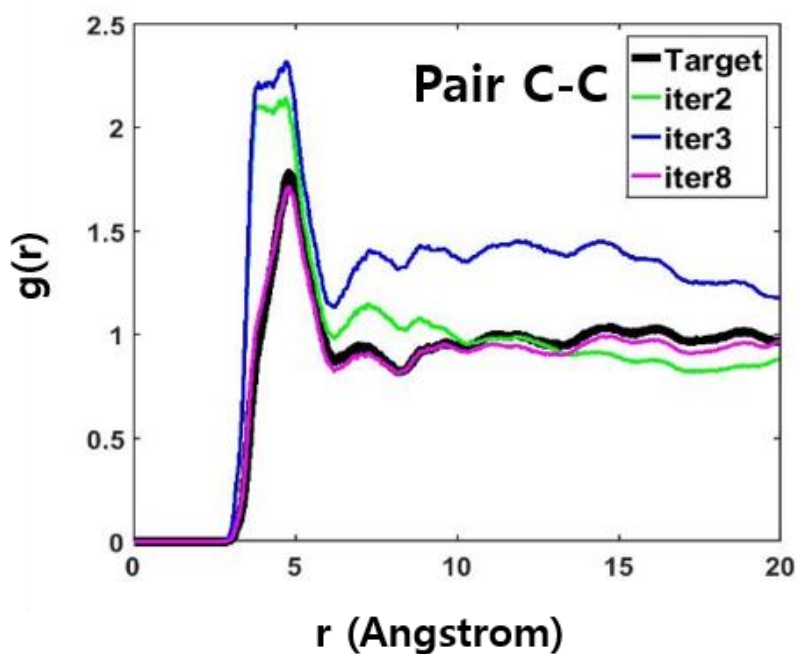


Figure 2.5 The process of RDF converging to the target RDF through the IBI equation.

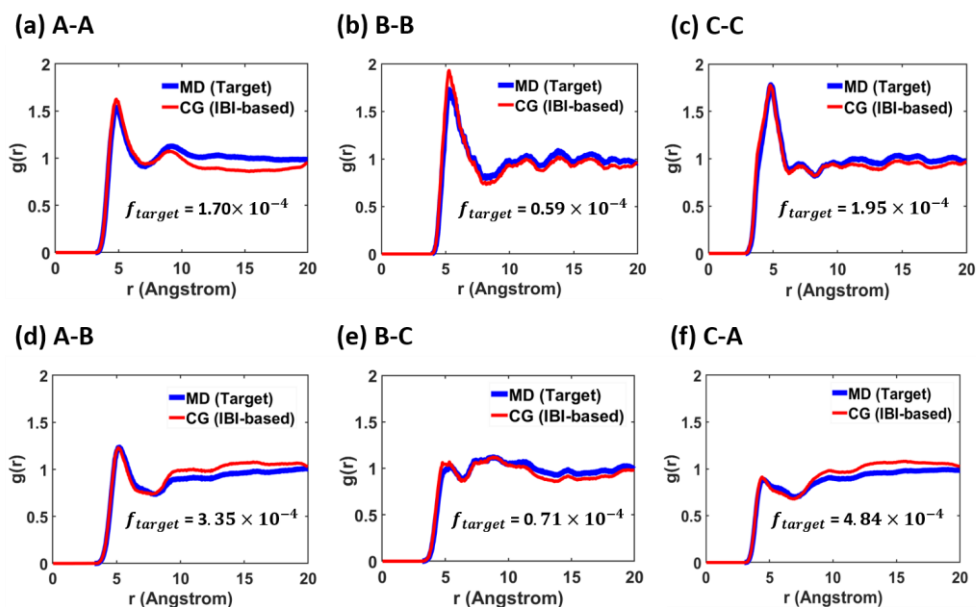


Figure 2.6 Comparison between the target RDF obtained through the AA reference model and the RDF obtained through the CG model where the IBI process was completed..

2.1.3 CG modeling for Silica nanoparticle

To simulate the CG SMPU-silica nanocomposite system, we have to derive the new CG potentials that represent the interaction between the nanoparticle and polymer chains. Figure 2.7 shows the chemical structure of SiO_2 silica nanoparticle and the bead mapping strategy. In order to accurately reflect the interaction between the nanoparticle and the SMPU chain, it is necessary to capture a clear RDF peak between the nanoparticle and the SMPU chain, it is necessary to capture a clear RDF peak between the surface part of the nanoparticle and the PU matrix [57]. Therefore, we mapped the particle into two kinds of beads. The positions of the outmost Si atom was treated as shell (S) beads, and the remaining Si atom was treated as core (Co) beads.

As in section 2.1.2, an all-atom reference structure was established to develop SMPU-silica CG potentials. As shown in Figure 2.8a, it consists of the same 80 polymer chains as in section 2.1.2 and a SiO₂ nanoparticle with a radius of 12.91 angstroms. In order to investigate the nanoparticle clustering behavior, not only the SMPU-silica interaction, but also the interaction between particles is important. To induce the interparticle CG potential, a unit cell composed of 7 identical SiO₂ nanoparticles was additionally constructed (Figure 2.8b). The relaxation process of the unit cell to obtain reference trajectories for deriving structural conformations and target RDFs is the same as in section 2.1.2.

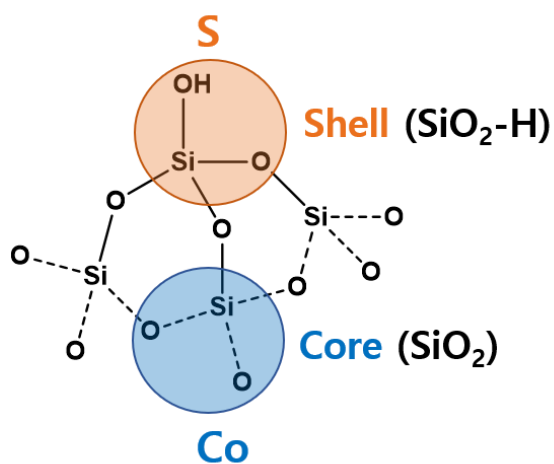


Figure 2.7 Core-shell bead mapping strategy for CG model of silica nanoparticle.

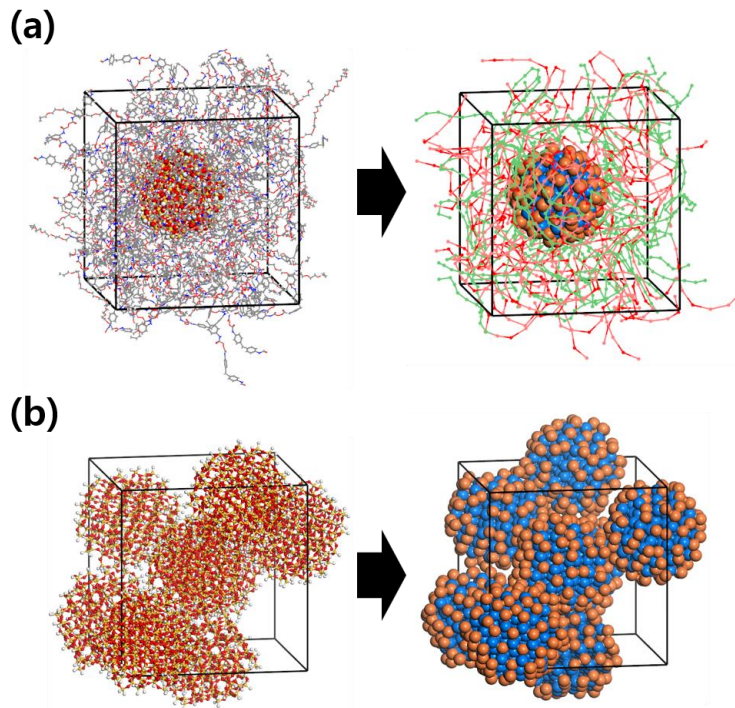


Figure 2.8 AA and CG MD configurations of the referenc unit cells for deriving CG potentials (a) between SMPU matrix and silica nanoparticle, and (b) between silica nanoparticles.

Bonded potentials for beads (Co, S) of silica nanoparticle were derived through the same process as in section 2.1.2 by using the reference trajectories. Figure 2.9 shows the same CG potentials for bond lengths between Co-Co, Co-S and S-S. Figure 2.10 shows the CG bending angle potentials for angles in all cases that can com from silica nanoparticles. Tables 2.3 and 2.4 also shows the parameterized coefficients for multi-centered gaussian funtions of bond length and bending angle CG potentials.

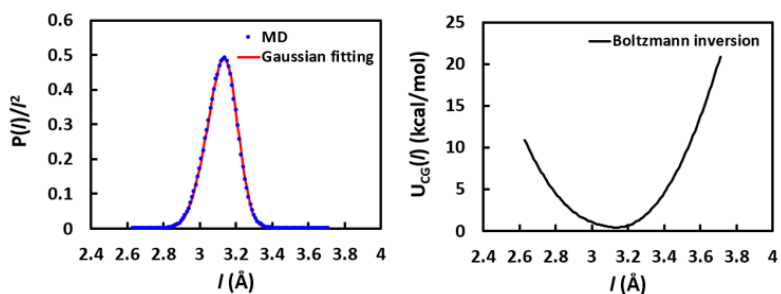
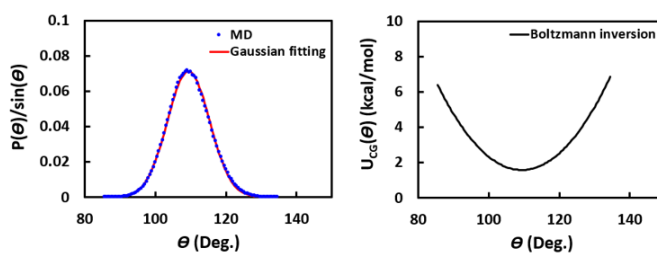
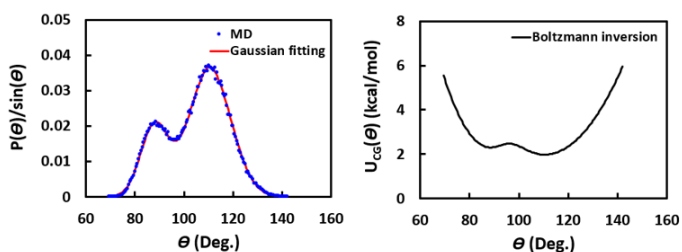


Figure 2.9 Results of bond length distribution and derived CG potential energy of silica nanoparticle (Co-Co, Co-S, S-S).

(a) Bending Angle (Co-Co-Co, Co-S-Co, S-Co-S)



(b) Bending Angle (Co-Co-S, Co-S-S)



(c) Bending Angle (S-S-S)

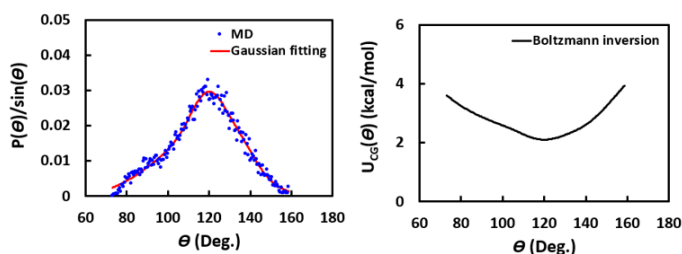


Figure 2.10 Results of bending angle distributions and derived CG potential energies of silica nanoparticle.

Table 2.3 Bond length CG potential energy coefficients for silica nanoparticle.

Bond length	a_1	b_1 [Å]	l_1 [Å]	a_2	b_2 [Å]	l_2 [Å]	a_3	b_3 [Å]	l_3 [Å]
Co-Co,									
Co-S,	0.409	0.096	3.151	0.180	0.104	3.051			
S-S									

Table 2.4 Bending angle CG potential energy coefficients for silica nanoparticle.

Bending angle	a_1	b_1 [°]	θ_1 [°]	a_2	b_2 [°]	θ_2 [°]	a_3	b_3 [°]	θ_3 [°]
Co-Co-Co,									
Co-S-Co,	0.071	8.418	109.4						
S-Co-S									
Co-Co-S,									
Co-S-S	0.001	2.769	110.2	0.020	7.930	87.92	0.036	12.21	110.5
S-S-S	0.065	13.47	126.7	-0.050	12.19	127.5	0.015	29.23	112.3

In order to derive the nonbonded potentials between nanoparticle and polymer chains, we obtained the target RDFs by using all-atom MD simulation (Figure 2.8a). There are six new RDFs between nanoparticle(Shell(S), Core (Co)) and polymer chains (A, B, and C) ; S-A, S-B, S-C, Co-A, Co-B, Co-C.

Figure 2.11 shows the target RDFs between nanoparticle and polymer matrix obtained from the all-atom MD. The polymer chains interact mainly with the shell part of the nanoparticle, so the RDFs between the chains and the shell of the particle have the clear peaks. Whereas, the RDFs between the chains and the core part of the particle have unclear shape, which indicates a relatively weak interactions.

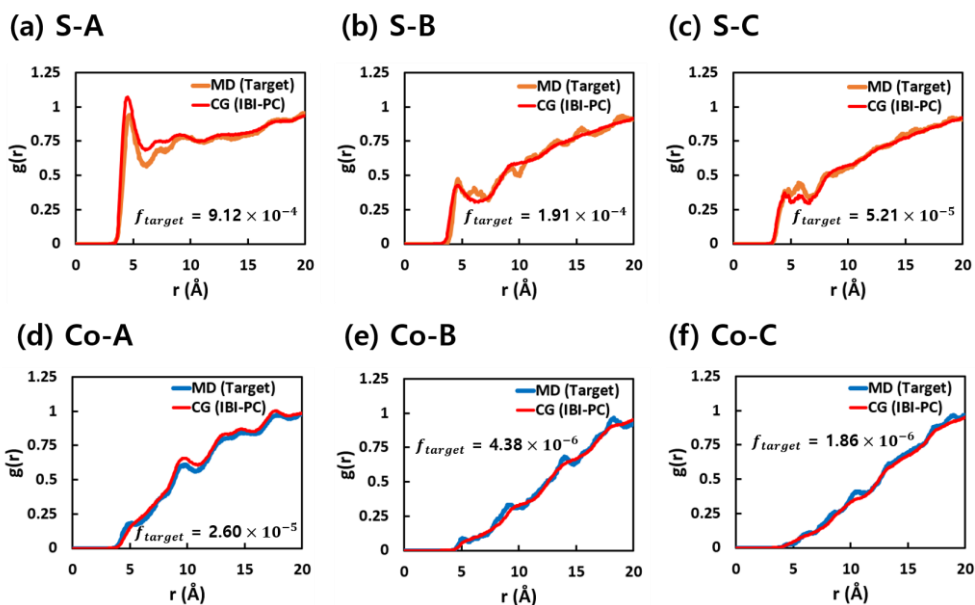
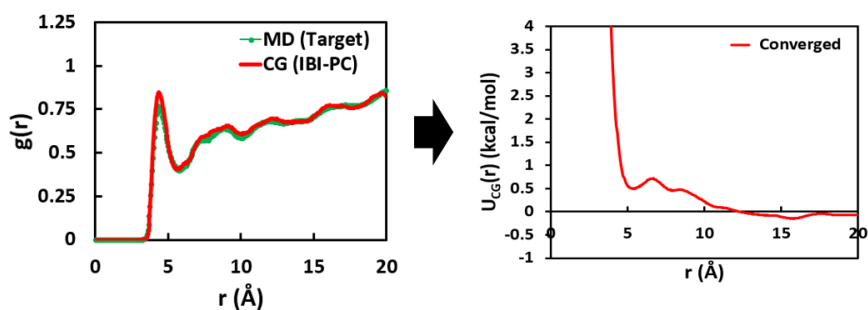


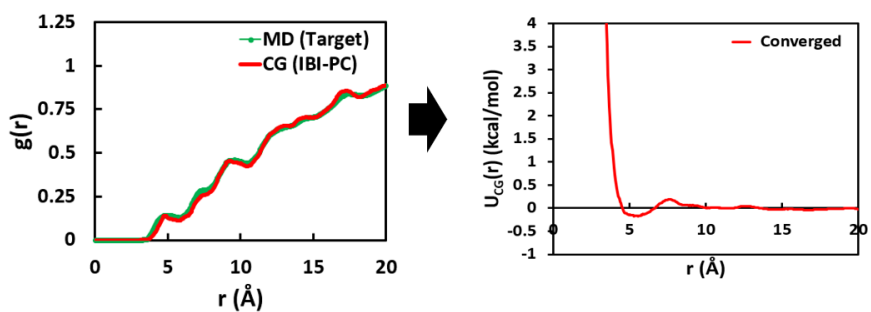
Figure 2.11 Comparisons between the target RDFs and CG RDFs (IBI-PC completed) for matrix-naniparticle interactions obtained from the reference unit cells (Figure 2.8a).

The RDFs between beads derived from the bead model where both IBI and pressure correction are completed matches the target RDFs well, and the target function value for each pair is also shown in Figure 2.11. The density of the SMPU-silica nanocomposites system calculated by using the CG potentials was 1.228 g/cc at 300 K, which is which is comparable to that of the reference atomistic model (1.233 g/cc). Finally, interparticle nonbonded potentials (S-S, S-Co, Co,Co) were developed. Figure 2.12 shows the final RDF comparisons derived through the reference model of Figure 2.8b and the completed CG nonbonded potential energies.

(a) S-S



(b) S-Co



(c) Co-Co

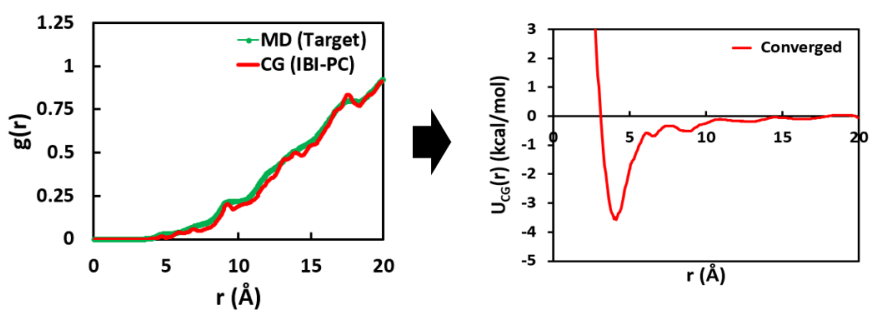


Figure 2.12 Comparison between the target RDFs and CG RDFs (IBI-PC completed) for interparticle interactions obtained from the reference unit cells (Figure 2.8b), and the corresponding CG nonbonded energy curves.

2.2 Effect of molecular compositions on thermo-mechanical behaviors of pristine SMPU

After completing the derivation of all CG potentials, new bead models were created for mesoscale analysis at increased length and time scale. The Mesocite module in the Materials Studio package (BIOVIA, Inc.) was employed to construct CG models with different segment ratios of polyurethane copolymer. The CG bulk unit cells have 9,022-17,446 beads, which are equivalent to 65,962-158,626 atoms. The molecular weight of soft-segment (bead A) for all CG models was fixed at 640 beads (4480 atoms, 28193.9 g/mol) to focus solely on the effect of the HSC on the molecular behavior. The hard-segment's (bead B and C) molecular weight was gradually increased, resulting in seven different HSC models. Table 2.5 presents the specific HSC values and detailed information for each CG model. Each model underwent equilibration using sequential steps that included energy minimization, the NPT ensemble for 80 ns at 300 K and 0.1 MPa with a timestep of 10 fs. During the CG MD simulations, the Langevin thermostat [58] controlled the temperature, and the Berendsen barostat [59] controlled the pressure.

Table 2.5 Information on the mesoscale CG models with different HSCs.

(All models have the same number of soft-segment beads = 8320 beads)

Model	HSC [wt. %]	No. of hard- segment beads	Molecular weight [kg/mol]	No. of corresponding atoms	Density (CG) [g/cc]
PU15	15.27	702	33.31	65,962	1.223
PU21	21.28	1,053	35.87	69,823	1.258
PU32	32.46	1,872	41.84	78,832	1.319
PU45	45.68	3,276	52.07	94,276	1.378
PU50	50.52	3,978	57.19	101,998	1.381
PU60	60.20	5,850	70.83	122,590	1.355
PU70	70.23	9,126	94.71	158,626	1.261

2.2.1 Crystallinity of the SMPU

In order to examine how semi-crystalline polymers behave thermodynamically, it is necessary to define the level of crystallization, or crystallinity, of the polymer models at a mesoscopic level. We utilized the same approach as Deng et al. [60], who applied a method for simulating semi-crystalline polymers. We introduced the orientational order parameter (S) as a means of measuring the degree of molecular alignment. This parameter can be calculated using the following equation:

$$S = \langle P_2(\cos\theta) \rangle = \left\langle \frac{3\cos^2\theta - 1}{2} \right\rangle \quad (2.8)$$

The symbol θ represents the angle formed between the reference axis and the

direction vector, and $\langle \cdot \rangle$ indicates the average value for all the beads. The reference axis vector for each bead in a polymer chain is defined as the vector that connects it to its neighboring beads. This is also done for another bead in the same manner. Figure 2.13 illustrates the calculation process in detail. The orientational order parameter is determined by averaging the values of beads within a certain distance (four times the bond length) from a particular bead (i). If the averaged value is greater than 0.6, then that bead (i) is considered crystalline. The level of crystallinity is assessed by calculating the ratio of crystalline beads to the overall number of beads present in the system.

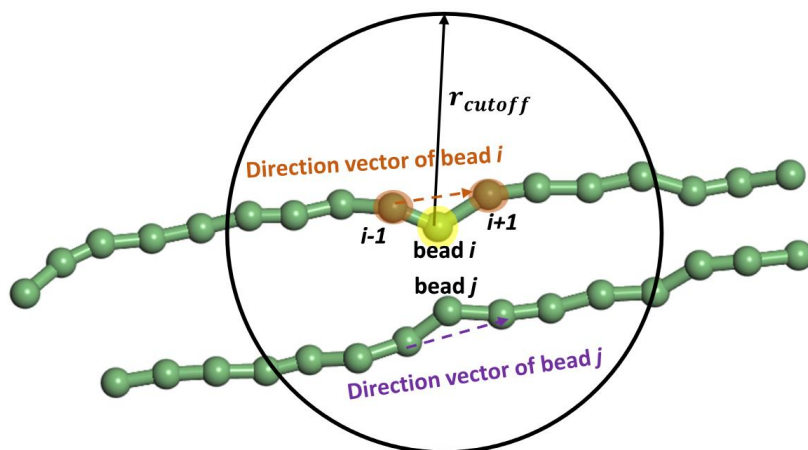


Figure 2.13 A depiction of the reference axis and direction vector within the polymer, which were used to define the crystallinity in the CG model.

Our investigation focused on the crystallization process of SMPU copolymers and how the relaxation time of simulations affects their structural changes. The results, shown in Figure 2.14, demonstrate how the crystallinity of linear block copolymers varies with different HSCs during the NPT ensemble at the room

temperature (300 K). As the models relaxed, the non-crystalline structures began to form crystalline polymers in the soft segment. Notably, we found that the content of the hard segments is critical on the morphological behavior. Increasing the concentration of MDI groups from 15 wt% to 70 wt% decreased the crystallinity of the equilibrium state from 0.383 to 0.003 due to the strong adhesion between the diisocyanates of the hard-segment beads, which inhibits the crystallization of the soft flexible chains. Our findings align with similar experimental studies [8,61,62] that suggest the chain-folding behavior of soft-segment mainly contributes to the crystallinity of segmented polyurethane, and the content of hard blocks significantly affects micromorphology. The corresponding structure according to the segment ratio will also affect the thermo-elastic behavior of the SMPU materials.

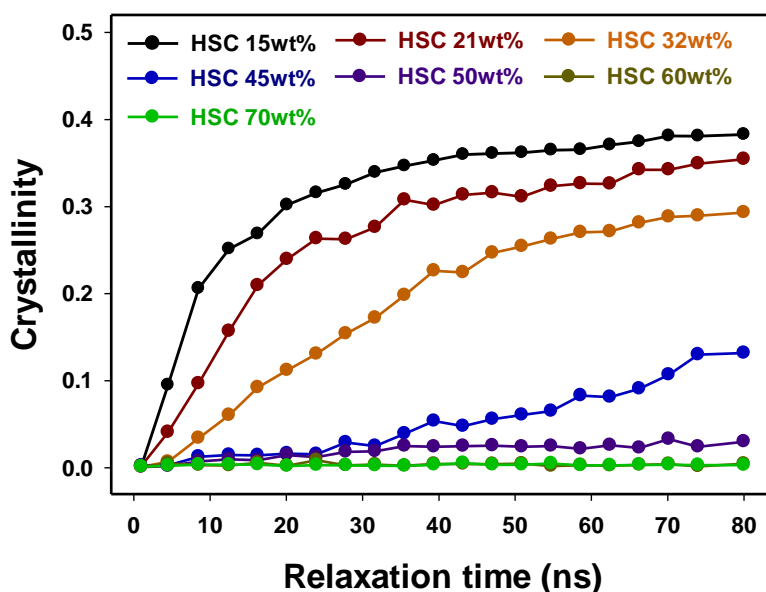


Figure 2.14 Crystallinity of the pristine SMPU copolymers with various hard-segment contents (HSCs) during the 80 ns of relation at 300 K.

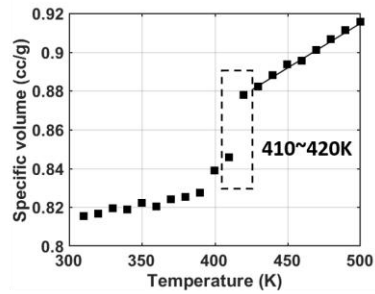
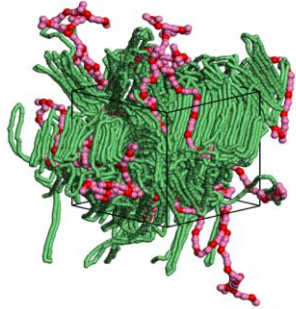
2.2.2 Melting temperature

The differences in crystallinity of SMPU copolymers based on HSC can have an impact on their thermal transition behavior. To investigate this, the melting temperature was evaluated by gradually increasing the temperature from 300 to 500 K at a rate of 10 K/20 ns and observing the specific volume change. As shown in Figure 15, the CG configurations of three different models with varying HSC were analyzed, and it was found that the most clearly folded polymer chains were observed in the PU15 model with the highest crystallinity. However, higher HSCs were found to destabilize the crystalline phase. During the simulated heating process, semi-crystalline polymers maintained a well-developed layered structure before quickly softening at the melting point. The specific volume was observed to increase significantly at the melting point, regardless of the HSC. It was observed that the melting temperature decreased with increasing polymer HSC, meaning that SMPU copolymers with low crystallinity have low melting temperatures. This phenomenon must be considered when modeling the actuation behavior of thermo-responsive block copolymers, as the melting point is the operating temperature of shape-recovery effect. The heat-activation temperature can be controlled by modifying the HSC of the hard-soft copolymer system.

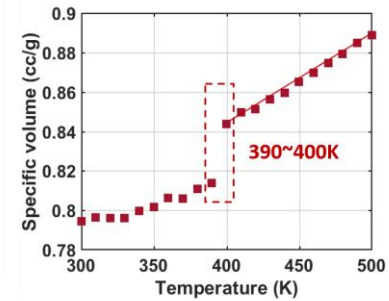
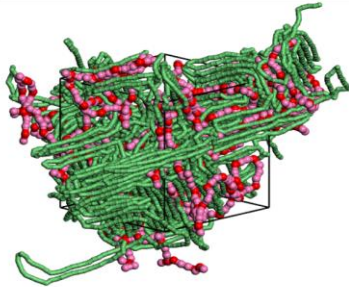
2.2.3 Mechanical behaviors

Mechanical loads under various conditions were applied to examine the structural evolution of each segment. Figure 2.16 presents the CG configurations of

(a) PU15 (HSC 15 wt. %)



(b) PU21 (HSC 21 wt. %)



(c) PU32 (HSC 32wt. %)

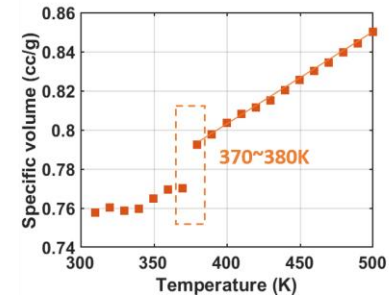
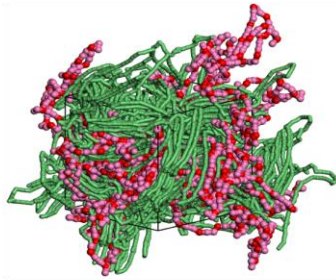


Figure 2.15 CG MD configurations of semi-crystalline SMPU with (a) HSC = 15 wt.%, (b) HSC = 15 wt.%, and (c) HSC = 32 wt.% and their specific volume change during the heating-up simulation.

PU15 (HSC 15 wt.%) under uniaxial tensile deformation at two different temperatures. When the temperature was below the melting point ($T=300$ K), the

soft segment had randomly oriented lamellar layers of polymer crystallites before any load was applied. During tensile deformation, the crystalline layers became uniaxially oriented (Figure 2.16a). However, when the temperature was above the transition temperature (ex. $T=410$ K), the amorphous and isotropic polymer chains exhibited flexible deformation (Figure 2.16b).

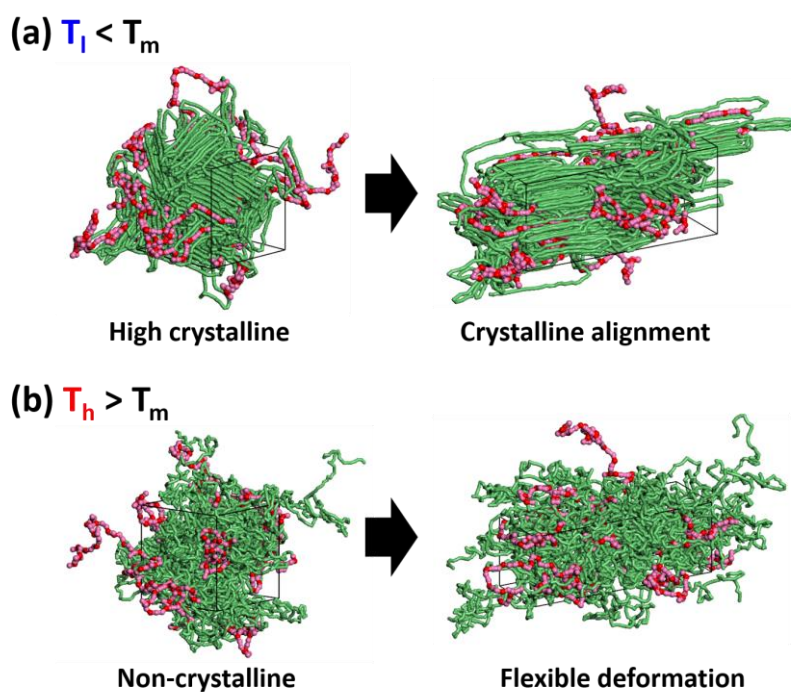


Figure 2.16 CG configurations of PU15 (HSC: 15 wt.%) undergoing uniaxial tensile deformation at (a) $T=300$ K and (b) 410 K.

The crystallinity and orientational order parameter of the PU15 were shown in Figure 2.17a as a function of the applied strain. When the strain was applied at 300 K, stretching resulted in further crystallization, so the fraction of the crystalline beads

slightly increased to approximately 34% at 150% strain. However, the orientational order parameter was nearly zero in the initial non-deformed state, even though the crystallinity was relatively high (0.383). As the strain increased to 150%, the order parameter of the soft segments sharply increased to 0.575, indicating that the crystallites were re-oriented parallel to the loading direction. Under the condition of a temperature of 410 K, the crystallinity and order parameter were zero in the initial un-deformed state, and although a large amount of strain was applied, the crystallinity remained near zero (0.003), and the order parameter increased to 0.117. At high temperatures, soft polymer chains remained amorphous regardless of the fraction of hard blocks. Therefore, under these conditions, the influence of the soft-segment itself on the mechanical property of the SMPU according to HSC will be insignificant.

However, regardless of the temperature, as HSC increases, the RDF peak between hard-segments increases (Figure 2.17b), which means that relatively stable hard-segment domains are formed in polymer network system. Therefore, both external temperature and molecular composition affect the structure of each hard segment and soft segment of the SMPU copolymers, and the resulting micromorphology will also affect their mechanical behaviors.

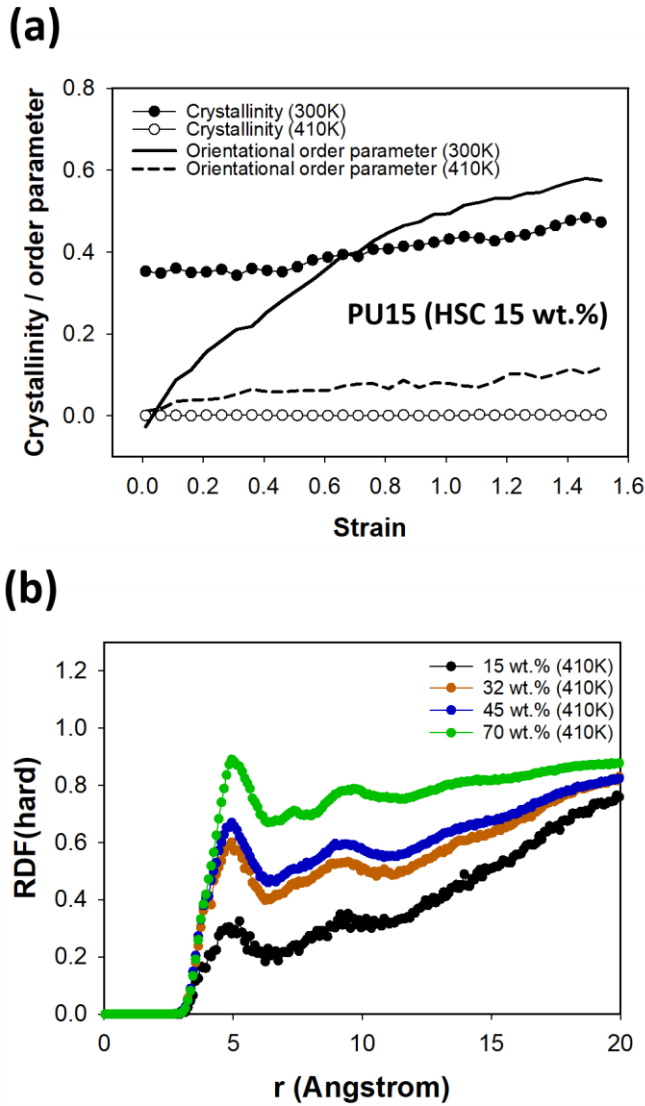


Figure 2.17 (a) Crystallinity and orientational order parameter of PU15 (HSC: 15 wt.%) under the uniaxial tensile test at $T=300$ K and 410 K. (b) RDF of the hard segment beads with different HSCs at $T=410$ K.

The graph in Figure 2.18 shows how the elastic modulus of SMPU copolymers changes based on the microstructures depending on the temperature and HSC. To determine the elastic modulus, we employed the gradient of the stress-strain graph

in its linear elastic range, spanning from 0 to 2%. The calculated values (38.4–607.9 MPa) were comparable to experimentally measured values (2.2–540 MPa) [63-67] for segmented thermoplastic polyurethanes. At a temperature of 300 K, increasing the concentration of hard segment from 15% to 70% decreased the elastic modulus by about 78%. However, at a temperature of 410 K, increasing HSC actually increased the elastic stiffness. At lower temperature, there was a greater difference in the elastic moduli, indicating that the increased stiffness was due to soft-segment crystallization caused by the hard-soft phase-separated structure. This phenomenon was shown to be significant in enhancing elastic stiffness. However, when the HSC was increased, the lamellar microstructure was disrupted, leading to a degradation in mechanical properties under the condition $T = 300$ K.

On the other hand, at higher temperatures where the soft polymer chain remained amorphous, the non-crystalline segment has sufficient molecular mobility to mix with the hard segment. Increasing HSC led to larger hard aggregations and this hard domain contributes more to the improved resistance to external load. These results were consistent with previous experimental studies [66,67] on the influence of crystallinity on elastic stiffness of semi-crystalline polyurethanes. The findings also supported unique relationships between elastic modulus and HSC at the two external temperatures, consistent with previous experimental reports [8]. The CG potential used in the study was derived from a reference state of 300 K and HSC of 65 wt%, but the model showed reasonable transferability for a wide range of temperature and molecular composition. The study suggests that modifying intrinsic

polymer architecture or thermo-mechanical history can easily modulate the mechanical properties of SMPU copolymers.

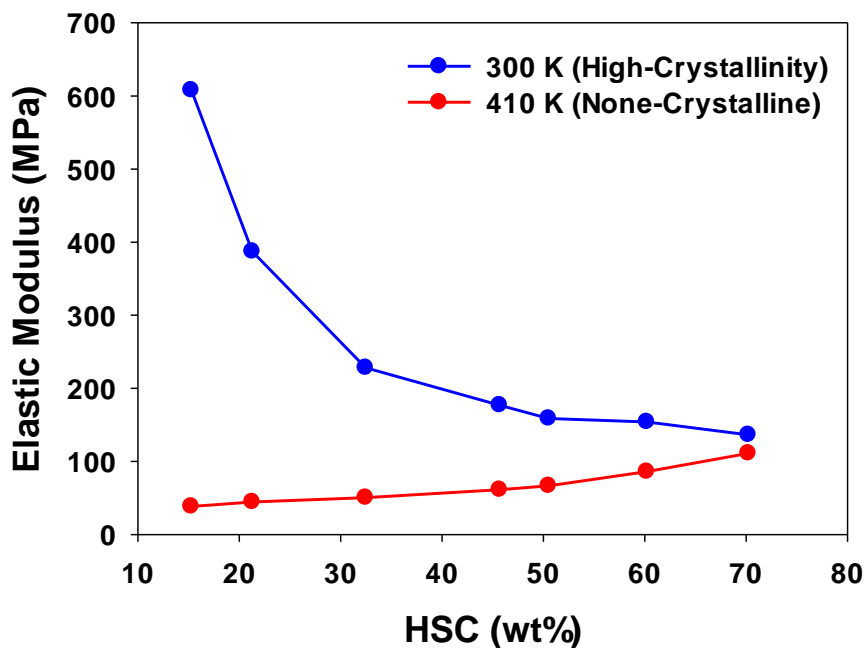


Figure 2.18 Elastic modulus results of the SMPU copolymers according to HSCs and external temperatures.

2.2.4 Shape-memory properties

To simulate the mesoscopic shape-memory thermo-mechanical cycle, the CG models were utilized and the LAMMPS code was implemented with the developed CG potentials to carry out sequential simulations as described in Figure 2.19. The shape-memory cycle comprises four steps, including loading, cooling, unloading, and reheating. Figure 2.19 displays the mesoscopic morphology and unit cell shape variations of the SMPU model during the shape-memory cycle. Before the first

loading step, the CG bulk unit cell is geometrically optimized and equilibrated in the NPT ensemble for 40 ns under 370 K and 0.1 MPa conditions, while the polymer chains of the original shape ($\varepsilon = \varepsilon_0$) remain in a non-crystalline isotropic state. Afterward, uniaxial tensile loading is applied in the x-axis direction of the unit cell up to strain of 200% ($\varepsilon = \varepsilon_t$) with a nominal strain rate of $10^8/s$. Cooling maintains the temporary deformed shape while the external temperature decreases to 300 K through an NVT ensemble for 20 ns, and polymer crystallization occurs during this process. An NPT ensemble is applied for 20 ns under 300 K and 0.1 MPa conditions to relax the external stress during the unloading process. Under stress relaxation, the SMPU copolymer fixes its shape with a new strain value ($\varepsilon = \varepsilon_f$), and finally, the unit cell is heated to high temperature through an anisotropic NPT ensemble for 500 ns. The activation temperature of T_m+20 K was chosen, following an experimental approach [61], to examine the structural recoveries. During heating, the polymer undergoes deformation to the recovered strain ($\varepsilon = \varepsilon_r$) after the removal of its crystalline structure

The shape-fixity ratio (R_f) and the shape-recovery ratio (R_r) are the two crucial characteristics that reflect the shape-memory performance of the thermo-mechanical cycle, which can be expressed through equation (2.9).

$$\begin{aligned}
 R_f &= \frac{\varepsilon_f}{\varepsilon_t} \\
 R_r &= \frac{\varepsilon_t - \varepsilon_r}{\varepsilon_t}
 \end{aligned}
 \tag{2.9}$$

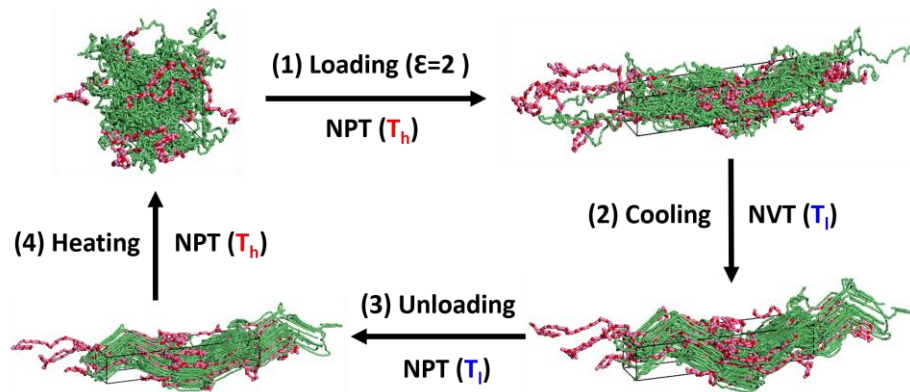


Figure 2.19 CG simulation process of the 4-step shape-memory thermo-mechanical cycle.

The 3D results of the shape-memory thermo-mechanical cycle of an SMPU with an HSC of 15 wt% are displayed in Figure 2.20, depicting the crystallinity–temperature–strain relationship. The four differently colored lines represent the four steps of the cycle. During the first step, the SMPU copolymer was subjected to tensile loading with a maximum strain of 200%, and the crystallinity value barely increased due to the relatively high external temperature ($T = 370$ K). However, as the system cooled to $T = 300$ K, the level of strain was maintained, and the crystallinity value sharply increased, indicating a transformation of the amorphous soft phase into the crystalline phase. After the load was removed, the crystallinity of the SMPU copolymer slightly increased. During the heating phase, the temperature increased to $T_m + 20$ K, and the strain and crystallinity values significantly decreased, indicating the shape-recovery behavior of the SMPU copolymer was primarily activated by the crystalline–amorphous transition of the soft segments.

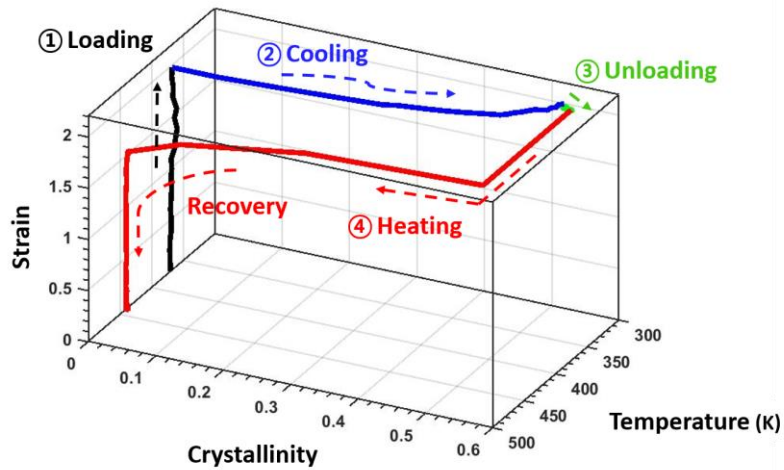


Figure 2.20 3-D plot (strain-temperature-crystallinity) of the SMPU with HSC = 15 wt.% during the 4-step thermo-mechanical shape memory cycles.

Figure 2.21 compares the 3D results for SMPU copolymers with three different HSCs, with the black, blue, and green lines representing SMPU copolymers with HSCs of 15, 45, and 70 wt%, respectively. The ratio of hard to soft segments affects the entire shape-memory curve, with the CG model possessing the lowest HSC showing the most distinct crystalline structure during the cooling period, despite all three SMPU copolymers having the same deformation history (Figure 2.21, top-right inset). This result aligns with the observations discussed in Section 3.1.1. Moreover, the copolymer with the lowest HSC value fixed the temporary shape best during the stress relaxation step, owing to the formation of the rigid crystalline structure (Figure 2.21, bottom-right inset). Increasing the HSC led to a decrease in the activation temperature and degree of shape-recovery during the reheating phase.

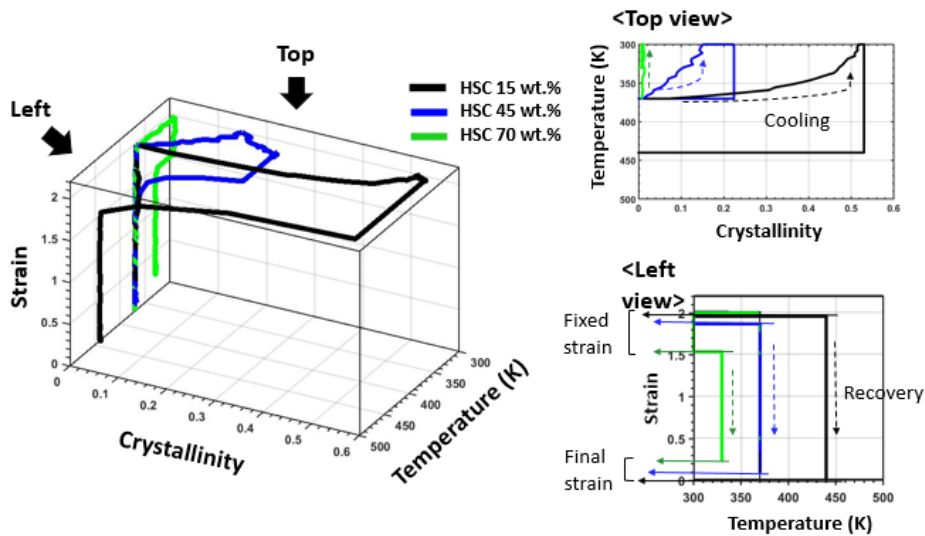


Figure 2.21 Shape-memory 3-D plots of the SMPU with three different HSCs (15, 45, and 70 wt.%).

Table 2.6 presents the shape-fixity ratio, shape-recovery ratio, and crystallinity values obtained after the unloading step for each model. The impact of the high HSC on various macroscale shape-memory performance metrics can be attributed to microstructural differences. As shown in Table 2.6 and Figure 2.21, increasing the HSC results in a decrease in the shape-fixity ratio. In semi-crystalline polymers, a higher fraction of crystalline molecules is advantageous for retaining the pre-deformed shape during the unloading step due to limited conformational molecular mobility in densely packed polymer chains within crystallites, compared to the amorphous state [4,8,61]. Furthermore, an increase in HSC corresponds to a decrease in the shape-recovery ratio, with the SMPU copolymer having an HSC of 15 wt% showing nearly 100% shape-recovery performance. Generally, good shape-recovery performance can be achieved with SMPU copolymers having a polymer chain HSC

of up to 50 wt%, but increasing HSC beyond 50 wt% tends to reduce the shape-recovery ratio to below 90%. This suggests that higher HSC in SMPU polymer chains hinders the shape-recovery process, as localized irreversible deformation of the hard-segment domains is a major contributor to residual strain in SMPU copolymers [8,32,61]. Specifically, plastic deformation of the hard-segment domains may not be fully corrected, even when the crystalline polymer of the soft segment is released above the melting temperature.

Table 2.6 Shape-memory performances and crystallinity during the shape-memory cycle.

Model	HSC [wt. %]	R_f (%)	R_r (%)	Crystallinity after cooling	Crystallinity after fixing
PU15	15.27	97.17	99.3	0.4956	0.5186
PU21	21.28	99.56	95.29	0.4107	0.4476
PU32	32.46	97.81	94.32	0.3320	0.3964
PU45	45.68	96.41	93.27	0.1394	0.2357
PU50	50.52	95.18	93.07	0.0821	0.1421
PU60	60.20	92.41	88.66	0.0194	0.0314
PU70	70.23	76.85	87.24	0.0099	0.0086

To investigate how well the hard phase recovers its shape in SMPU copolymers, we analyzed the behavior of polymer chains during the heating phase. Figure 2.22 and 2.23 displays the changes in the radius of gyration (R_g) and mean square displacement (MSD) of the hard segment during the shape-recovery process. In

Figure 2.22, the dashed lines represent the R_g values of the hard segment in its non-deformed state. Due to the relatively larger hard-segment domain in SMPU copolymers, the radius of gyration of the hard segment in the original shape is larger. Prior to heating in the simulations, all SMPU models exhibited R_g values much larger than those of the original state, indicating that the molecules were elongated by the tensile strain. When shape-recovery behavior was activated, the polymeric conformation of the hard domain was rapidly restored. For SMPU copolymer with a hard-segment content (HSC) of 15 wt%, the hard-segment radius of gyration was fully recovered during the heating phase. However, increasing the fraction of the aggregated hard-segment domain hindered the SMPU copolymer from returning to its initial state. These results, as shown in Figure 2.22, explain the presence of residual strain in SMPU copolymers with larger hard-segment domains after shape recovery.

Figure 2.23 displays the MSD in the loading direction (i.e., along the x-axis) of each segment in the SMPU copolymers during heating. The MSD curves for the polymer chains can be calculated using equation (2.10).

$$MSD_x(\Delta t) = \frac{1}{N} \sum_{i=1}^N \langle |r_{i,x}(t - \Delta t) - r_{i,x}(t)|^2 \rangle$$

$$MSD_x = \frac{1}{N} \sum_{i=1}^N \langle |r_{i,x}(t) - r_{i,x}(0)|^2 \rangle$$
(2.10)

Here, the x-axis position of atom i at time t is denoted as $r_{i,x}(t)$, with N representing the total number of atoms and $\langle \bullet \rangle$ indicating the ensemble average. The MSD curves for the soft and hard segments are illustrated in Figure 2.23 using dotted and

solid lines, respectively. Previous studies have suggested that the high mobility of polymer chains in the loading direction during heating is an important point in the shape recovery of shape memory polymers (SMPs) [51,68]. For instance, the SMPU copolymer with a HSC of 15 wt%, the mobility of the hard segment was observed to be higher than that of the soft segment due to incomplete formation of the segregated hard domain. On the other hand, a relatively high HSC was found to constrain the overall movement of the polymer chain due to strong adhesion between the hard segments, resulting in reduced mobility of the hard segment. This reduced mobility can also explain the less desirable shape recovery performance of polymer chains with higher HSCs.

The simulation results suggest that the macroscopic shape of the thermo-responsive SMP actuator can be controlled by modifying the mesoscopic polymer architecture of the material, along with the diffusivity of the constituent polymer chains.

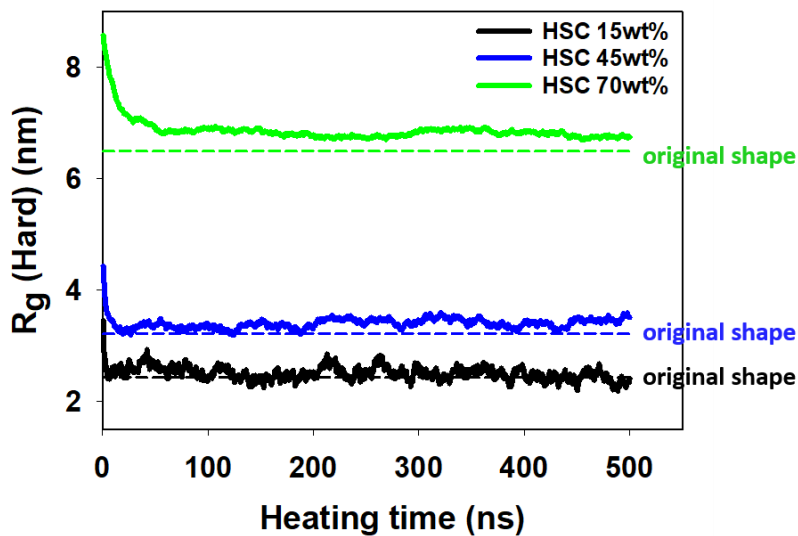


Figure 2.22 Changes in the radius of gyration (R_g) of the hard segment during shape recovery.

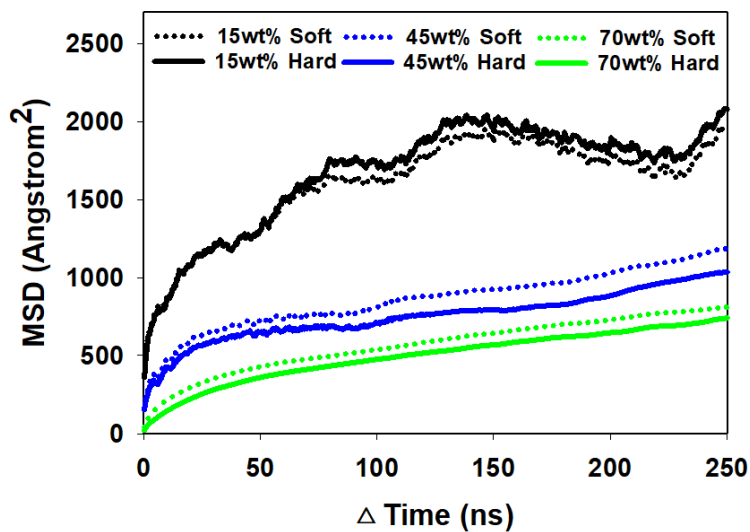


Figure 2.23 Changes in the mean square displacement (MSD) in the loading direction (x-axis) of each segment of the SMPU copolymer during shape recovery.

2.3 Effect of incorporation of silica nanofiller

2.3.1 SMPU microstructure on silica surface

First, a single silica nanoparticle was added to four different HSC (15, 32, 50, and 70 wt.%) SMPU matrices. To investigate the microstructure around the silica surface, silica with a radius of 30 angstroms composed of a core and a shell bead was constructed. Figure 2.24 shows the unit cells of SMPU-silica CG nanocomposite models containing a single nanoparticle equivalent to 10 wt.%.

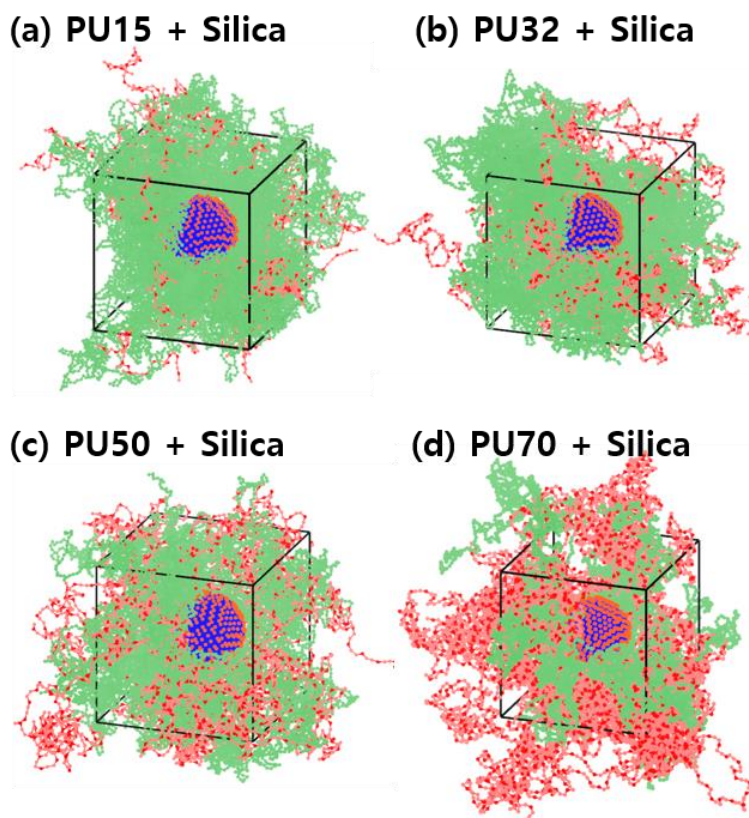


Figure 2.24 CG configurations of the SMPU nanocomposites with different HSCs (15, 32, 50, 70 wt.%) containing single silica nanoparticles with a radius of 30 Å .

It is known that the silica surface has strong interactions with both the soft segment ether (C-O-C) polyol and the hard domains (N-H, C=O). Looking at the radial density originating from the core of a silica nanoparticle in Figure 2.25, the presence of a high-density peak in the interphase around the silica surface was well simulated [69-71]. It can be seen that the aspect of the high-density peak varies depending on the HSC. As the interphase thickness decreases as the HSC increases, it seems that the silica surface is more compatible with the low-HSC SMPU, forming a more stable and thicker interphase.

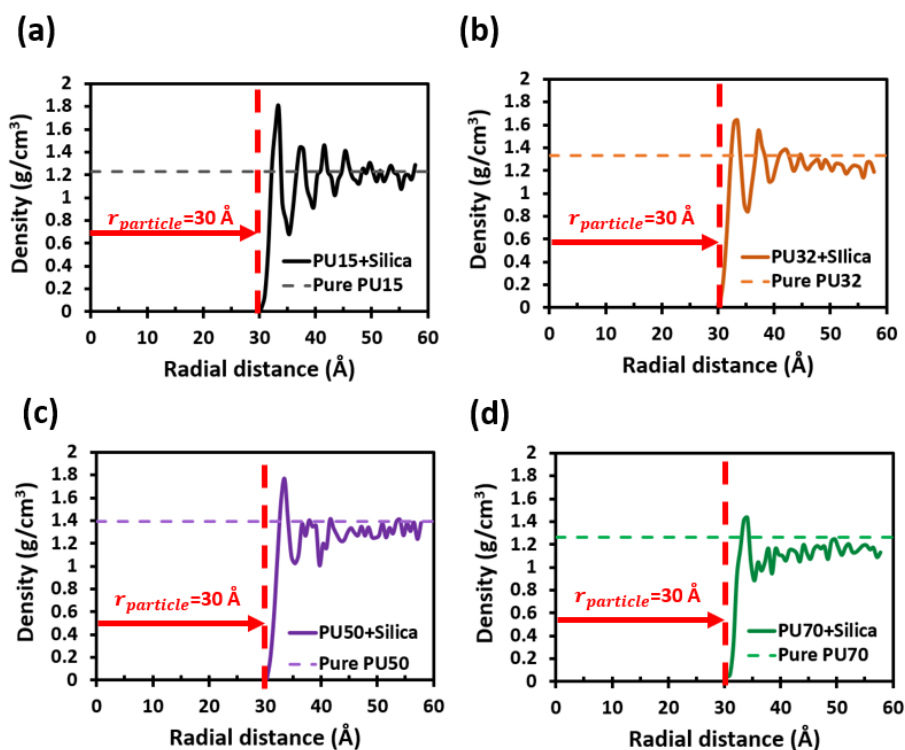


Figure 2.25 Radial density of the SMPU matrix and the high-density interphase region

To further investigate the polymer structure around the surface of the nanoparticles in nano level, the crystallinity was calculated in the radial direction of the nanoparticle starting from its center. Figure 2.26 shows the orientational order parameter (S) (equation (2.8)) for each and every bead of crystalline PU15 model at 300 K. The orientational order parameter (S) was calculated in the same way as in section 2.2.1, and a bead with this value of 0.6 or more is defined as a crystalline bead, and the crystallinity of the system is the number of crystalline beads per total number of beads. The S value of each bead is represented by the color of the range shown in the color bar, and the dark red area is the area where crystalline is strongly formed. As shown in Figure 2.26, the average S value of all beads is 0.451, while the average S value of beads in the interphase region 10 Å thick from the surface of the silica nanoparticle is 0.231. This means that there are almost no crystalline beads around the nanoparticle surface. Using the calculated order parameter, the degree of crystallinity was obtained by partitioning the section radially from the nanoparticle center.

Figure 2.27 compares the radial crystallinity of pristine SMPU and SMPU-silica nanocomposites at 15, 32 and 50 wt.% of HSCs. Radial distances were measured from the center of unitcell for pristine SMPUs and from the center of mass of silica nanoparticles for SMPU nanocomposites. As in section 2.2.1, the crystallinity of the SMPU tends to decrease as the ratio of hard-segment increases. It can be seen that the pristine SMPU has a uniform crystallinity distribution inside the unit cell irrespective of the radial distance. However, looking at the crystallinity

of the polymer chains around the silica surface, the soft segment in interphase region does not form a crystalline arrangement because of the strong adsorption with the silica surface. These results are consistent with the experimental results that silica nanoparticulate fillers can suppress the crystallization of thermoplastic polyurethane due to physical hindrance reducing chain mobility [72-74].

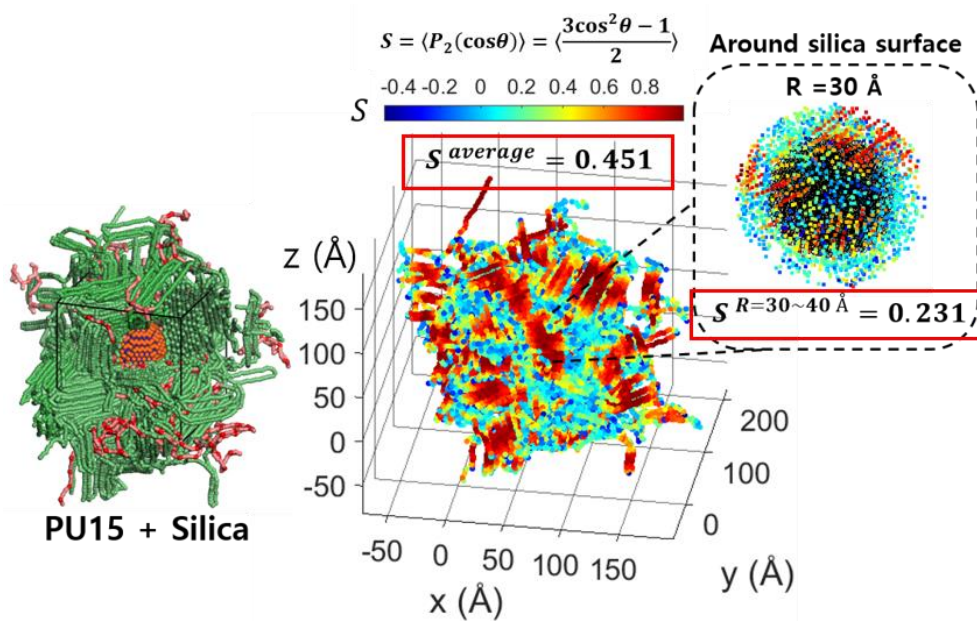


Figure 2.26 S value of each bead of SMPU matrix in PU15/Silica nanocomposite model. The average S value of the total matrix is 0.451, and the average S value of the 10 Å thick region around the silica nanoparticle is 0.231.

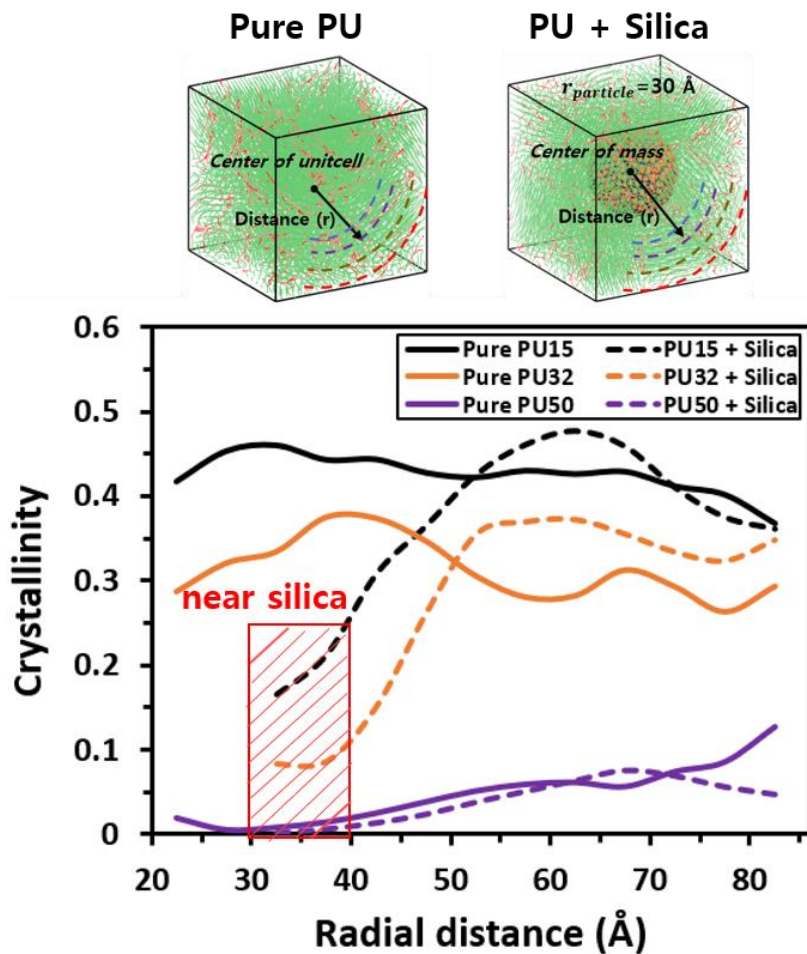


Figure 2.27 Comparisons between radial crystallinity distributions of the SMPU from the center of unitcell for pristine SMPU and from the center of the nanoparticle for SMPU/Silica nanocomposites.

2.3.2 Effect of silica nanoparticle content

More realistic SMPU nanocomposites models were constructed to investigate the shape-memory behaviors reflecting nanoparticle clustering effect as well as the interaction between matrix and nanofiller. For PU15, PU32, and PU50 (HSC 15, 32, and 50 wt.%), silica nanoparticles with a radius of 15 angstrom were added at four different contents (3, 6, 10, and 15 wt.%). The SMPU polymer chain for each HSC was used as shown in Table 2.5 in section 2.2. Table 2.7 shows the unit cell information of the corresponding SMPU nanocomposite models.

Table 2.7 Modeling of the mesoscale CG SMPU/Silica nanocomposites.

HSC [wt. %]	Silica content	No. of chains	No. of silica nanoparticles
PU15	3 wt.%	61	3
	6 wt.%	59	7
	10 wt.%	57	11
	15 wt.%	54	16
PU32	3 wt.%	49	3
	6 wt.%	47	7
	10 wt.%	45	11
	15 wt.%	43	16
PU50	3 wt.%	36	3
	6 wt.%	35	7
	10 wt.%	33	11
	15 wt.%	31	16

A shape-memory cycle was also performed on the SMPU-silica nanocomposite model. The high temperature of the loading step and heating step was 500K, which was the same for all unit cells, and the low temperature was 300K. The unit cell deformed to strain 2 at high temperature was cooled at 300 K for 100 ns, and an unloading step at 300 K and 0.1 MPa for 50 ns was performed. Final heating was performed with an anisotropic NPT ensemble at 500K and 0.1 MPa for 100 ns.

Table 2.8 Shape-fixity ratio (R_f) of the SMPU/Silica nanocomposites according to HSC (15, 32, and 50 wt.%) and silica content (3, 6, 10, 15 wt.%).

Silica Content (wt.%)		R_f (%)				
		0	3	6	10	15
SMPU	HSC					
PU15 (HSC 15 wt.%)		90.48	87.50	88.11	89.20	89.13
PU32 (HSC 32 wt.%)		89.51	87.72	88.66	90.07	92.68
PU50 (HSC 50 wt.%)		88.87	88.25	90.94	93.57	93.99

Table 2.9 Shape-recovery ratio (R_r) of the SMPU/Silica nanocomposites according to HSC (15, 32, and 50 wt.%) and silica content (3, 6, 10, 15 wt.%).

Silica Content (wt.%)		R_r (%)				
		0	3	6	10	15
SMPU	HSC					
PU15 (HSC 15 wt.%)		89.33	88.97	88.77	89.63	86.42
PU32 (HSC 32 wt.%)		89.20	89.46	90.17	89.55	85.81
PU50 (HSC 50 wt.%)		86.14	85.98	79.29	74.60	39.25

Table 2.8 and 2.9 show the shape-memory performances according to the silica content for SMPUs of three different HSCs. In this shape-memory cycle, all SMPU and SMPU/Silica nanocomposites models show good shape-fixity properties around 90%. According to section 2.2, the aggregated hard-segment domains make it difficult for the SMPU chain to recover its initial state and degrade the shape recovery ratio. Similar to the previous results, the recovery performance of PU50 is lower than that of PU15 or PU32 in all silica contents. According to Table 2.9, when the silica content in PU15 and PU32 increases to 15 wt.%, the shape recovery performance slightly deteriorates. From this, it can be seen that not only HSC but also silica nanoparticles affect the shape-memory performance.

To investigate the effect in more detail, the free volume change during the shape-memory cycle of the SMPU nanocomposite was investigated. Figure 2.28 and Table 2.10 shows the fractional free volume (FFV) of the PU15, PU32, and PU50 for the silica contents of 3 wt.% and 15 wt.%. FFV is calculated as the ratio of free volume to total unit cell volume. Common to all models, FFV increases at high temperature (500K) than at room temperature (300K), and it increases slightly when mechanical deformation is applied. In addition, the FFV is further increased by the free volume created between the semi-crystalline network chains and nanoparticles [75] during the cooling step, as shown in Figure 2.29. However, looking at the models of 3 wt.% silica in Figure 2.28 and Table 2.10, the free volume due to these crystalline structures and nanoparticles is completely recovered as the deformed-

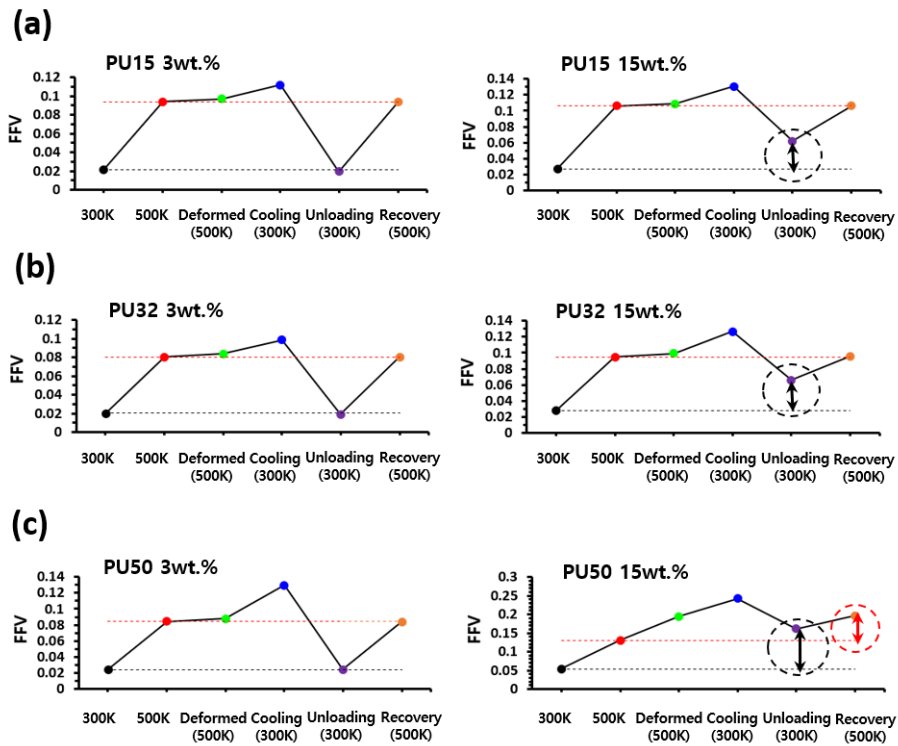


Figure 2.28 Changes in fractional free volume (FFV) during shape-memory cycles for silica content 3 wt.% and 15 wt.% of the (a) PU15, (b) PU32, and (c) PU50 nanocomposites.

Table 2.10 Fractional free volume (FFV) change during the shape-memory thermo-mechanical cycle.

Model	300K	500K	Deformed (500K)	After cooling (300K)	After Unloading (300K)	After Recovery (500 K)
PU15 3 wt. %	0.022	0.094	0.097	0.112	0.020	0.093
PU32 3 wt. %	0.020	0.080	0.084	0.099	0.019	0.080
PU50 3 wt. %	0.026	0.084	0.088	0.130	0.024	0.084
PU15 15 wt. %	0.027	0.106	0.109	0.131	0.062	0.106
PU32 15 wt. %	0.027	0.095	0.099	0.127	0.066	0.096
PU50 15 wt. %	0.054	0.131	0.164	0.242	0.157	0.198

strain changes to fixed strain in the unloading step. Therefore, it has a FFV value similar to that of the state before deformation at 300 K. In the silica 3 wt.% model, the strain was not completely recovered even after heating was completed, but it had the same value as the FFV at 500K before deformation.

It is known that excessive silica deteriorates the particle distribution and hinders chain motion, and the free volume of SMPU/silica nanocomposites increases as the silica content increases [76,77]. Comparing the 15 wt.% silica models of PU15, PU32, and PU50 with each 3 wt.% model in Figure 2.28, it can be seen that they have larger FFVs in all steps of the shape-memory cycle. When the content of silica is 15 wt.%, it is noteworthy that the FFV is not completely recovered despite the completion of the unloading step and has a larger free volume than the undeformed state at 300K.

Figure 2.30 shows the deformed shape at high temperature with various silica weight percent in PU15 nanocomposites. Looking at each CG MD configuration, an evident observation is that with the rise in silica content, nanoparticles tend to form concentrated aggregates within a specific region. In the spaces between these adjacent nanoparticles, intercalation of polymer chains becomes more difficult, and voids are formed [48,70]. Therefore, the formation of vacancy by nanoparticle aggregation can cause residual deformation after shape recovery in high-content silica models, and several experiments [73,76,89] have also shown that the shape-recovery ability is degraded as the amount of silica increases. This may also explain the slightly higher shape-fixity ratio in the high-content silica model in Table 2.8,

which has also been observed in experimental study [78].

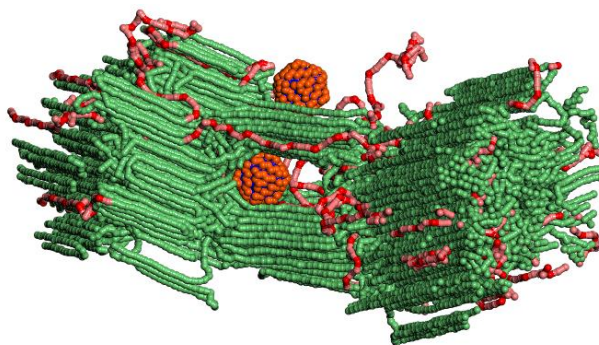
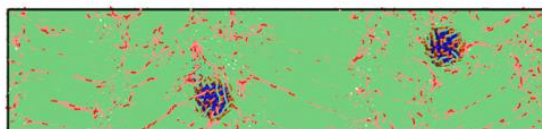
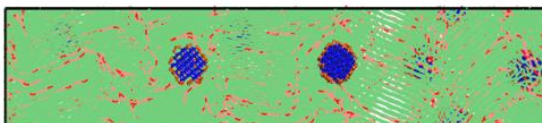


Figure 2.29 Formation of free volume by nanoparticles in semi-crystalline polymer chains.

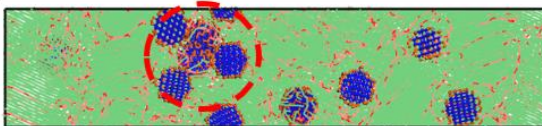
(a) PU15 3wt.%



(b) PU15 6wt.%



(c) PU15 10wt.%



(d) PU15 15wt.%

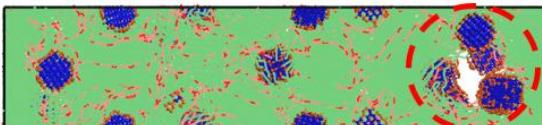
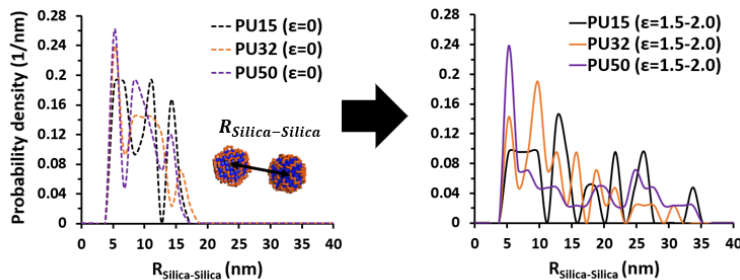


Figure 2.30 Nanoparticle agglomeration according to silica content and consequent formation of vacancy zone.

One more point to note here is that, in particular, in the PU50 (HSC 50wt.%) model, the degree of shape recovery decreases as the amount of silica gradually increases from 3 wt.% to 15 wt.%. This phenomenon means that the clustering behavior of nanoparticles can be affected not only by the content of silica but also by the interaction with the polymer matrix, that is, the hard-soft ratio of SMPU. Therefore, we further investigated the probability density of the distance between silica nanoparticles ($R_{Silica-Silica}$) for SMPU models with different HSCs (15, 32, and 50 wt.%) and silica contents (6 and 15 wt.%)

(a) Silica 6 wt.%



(b) Silica 15 wt.%

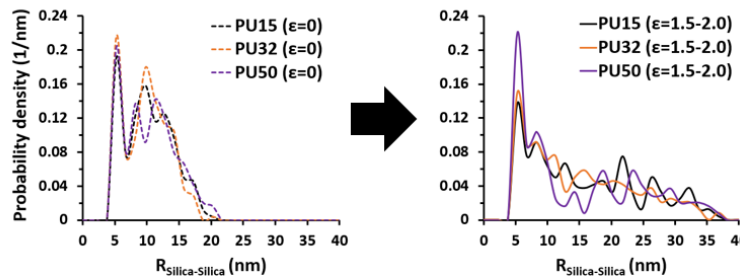


Figure 2.31 Probability distribution of $R_{Silica-Silica}$ (the distance between silica nanoparticles) for silica content (a) 6 wt.% and (b) 15 wt.% in undeformed and deformed shapes.

Table 2.11 Characterization of the probability distribution (Figure 2.31) of $R_{\text{Silica-Silica}}$

Model	Undeformed state ($\varepsilon = 0$)		Deformed state ($\varepsilon = 1.5 - 2.0$)	
	peak location (nm)	Max. peak height (nm ⁻¹)	peak location (nm)	Max. peak height (nm ⁻¹)
PU15 6 wt.%	6.0, 11.25	0.19	12.75	0.143
PU32 6 wt.%	5.25	0.238	9.75	0.190
PU50 6 wt.%	5.25	0.262	5.25	0.238
PU15 15 wt.%	5.25	0.192	5.25	0.138
PU32 15 wt.%	5.25	0.217	5.25	0.150
PU50 15 wt.%	5.25	0.204	5.25	0.221

Figure 2.31 shows the probability density of the distance between silica nanoparticles before and after deformation, and Table 2.11 shows the maximum peak height and corresponding location. In the undeformed state of PU15 with a silica content of 6 wt.%, there are three clear peaks and two maximum peaks (6.0, 11.25 nm). On the other hand, PU32 and PU50 have a maximum peak at 5.25 nm, and the peak height is slightly larger in PU50. From this, it can be seen that the distribution of silica nanoparticles spreads relatively uniformly in the SMPU matrix with a larger percentage of the soft segment of the SMPU. This silica clustering behavior can also be observed in mechanically deformed shapes. When strain is applied to the nanocomposite, the distance between the nanoparticles increases accordingly, and the probability density drops to a low value in a wide range. The maximum peak location moved to 12.75 nm in PU15 and to 9.75 nm in PU32, and the heights also decreased. However, PU50 maintained a quite high peak at the same 5.25 nm

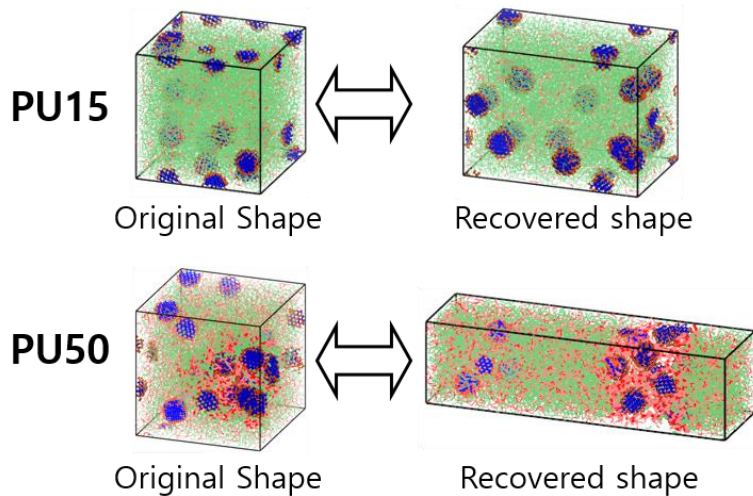
position.

In the undeformed state of the models containing 15 wt.% silica, the high maximum peak at 5.25 nm was shown regardless of HSC due to the high silica contents. Also, even when deformed by $\varepsilon = 1.5 - 2.0$, regardless of HSC, it has the same maximum probability of interparticle distance at 5.25 nm. The nanoparticle agglomeration behavior is more pronounced when mechanical strain is applied to PU50 with 15 wt.% of silica. In the HSC 50wt.% and Silica 15wt.% models, the maximum peak height in the deformed shape was even increased than before deformation.

Figure 2.32a shows the shape recovery performance according to different HSCs as the final result of these phenomena described above. Despite the same 15 wt.% silica content, nanoparticle agglomeration is more severe in PU50 than in PU15, and the region where nanoparticles are agglomerated inside the hard domain prevents the polymer system from recovering to its initial shape. It can be seen from the MSD graph in Figure 2.32b that the strong immobility of the nanoparticle cluster in hard domain [79] is maximized at high HSC and high silica content.

Looking at the behavior of the silica nanoparticles, as the HSC of the SMPU increases, the compatibility between the silica nanoparticles and the polymer matrix decreases, so that a stable interphase region between the particles and the matrix cannot be formed and the nanoparticles are more agglomerated. By conducting CG MD of SMPU-silica nanocomposites, we observed that there is a trade-off between the increased stiffness due to the nanofiller and the decreased ability to recover strain.

(a)



(b)

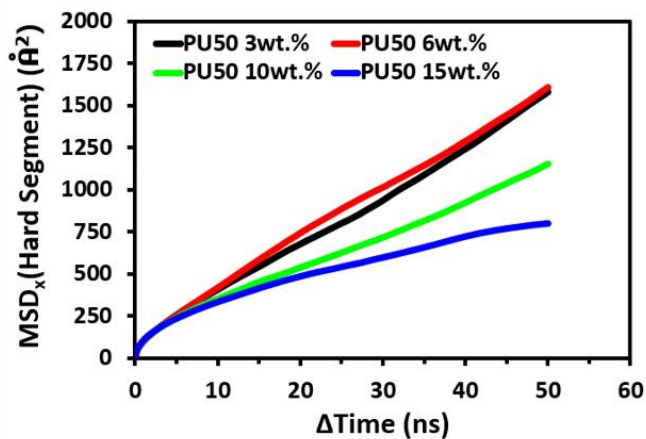


Figure 2.32 (a) Comparison between the original shape and recovered shape of PU15 and PU50 with 15 wt.% of silica. (b) Changes in the mean square displacement (MSD) in the loading direction (x-axis) of the hard segment of PU50/Silica nanocomposites.

These findings can serve as valuable guidelines for designing nanocomposites that strike a balance between recovery stress and recovery strain through the strategic use of fillers. Additionally, a more detailed study in solubility and phase separation through dissipative particle dynamics is required to more specifically understand the mixing and aggregation behaviors between these dissimilar materials, which will be performed in sections 3 and 4.

Chapter 3

Phase separation behaviors of SMPU

In Chapter 2, we investigated the mesoscale behavior of hard and soft segments of SMPU and their thermo-mechanical and shape-memory characteristics through CG models. In addition, performance change and particle agglomeration phenomena according to the addition of silica nanoparticles were also noticed. However, in order to perfectly design desired polymer nanocomposites, it is essential to comprehend not only the role of each segment, but also the phase-separated architectures of the SMPUs on a larger nanoscale. In addition, it is necessary to understand the material properties according to the distribution of silica nanoparticles and to have design skills that can directly control this clustering behavior. To this end, it is necessary to understand the phase separation behavior through differences in solubility parameters of each component of SMPU nanocomposites.

3.1 Dissipative particle dynamics (DPD) simulation

A Dissipative particle dynamics (DPD) proposed by Groot and Warren [80] serves as a meso-scale simulation method designed to replicate the dynamic and rheological characteristics of both uncomplicated and intricate fluids. In other words, DPD treats a large number of atoms as one bead and focuses on molecular behavior on the mesoscale, such as polymer dissolution by solvent or phase separation. At this time, every DPD bead adheres to Newton's equation of motion, and the r_i , v_i , m_i , and f_i represent each particle's position, velocity, mass, and force acting on the bead :

$$\frac{dr_i}{dt} = v_i \quad , \quad m_i \frac{dv_i}{dt} = f_i = \sum_{j \neq i} (F_{ij}^C + F_{ij}^D + F_{ij}^R) + F_{ij}^S \quad (3.1)$$

The bead i experiences a combined force (f_i) comprising conservative (F_{ij}^C), dissipative (F_{ij}^D), random (F_{ij}^R), and spring (F_{ij}^S) forces. Equation 3.2 expresses the conservative force, characterized as a soft repulsive force that operates along the line connecting the beads' centers. and gradually diminishes to zero as the distance between the beads reaches a specific cutoff radius, r_c .

$$F_{ij}^C = \begin{cases} a_{ij} \left(1 - \frac{r_{ij}}{r_c}\right) \hat{\mathbf{r}}_{ij} , & (r_{ij} < r_c) \\ 0, & (r_{ij} > r_c) \end{cases} \quad (3.2)$$

In other words, the polymer chains are not entangled with each other due to a rather simple and weak non-bond interaction, and the amount of computation is reduced due to the reduced degree of freedom. Therefore, DPD simulation dramatically

increases the time scale and enables intensive investigation of the phase mixing and separation behavior of polymers. The repulsion parameter (a_{ij}) is the most important factor to describe interactions between DPD beads, so we embraced the theory proposed by Groot and Warren [37] and AA MD simulation scheme to derive the precise values for the parameter.

The repulsion parameters between different types of bead were obtained through the Flory-Huggins parameter (χ) which can be calculated by the solubility (δ) difference between each molecular components. Solubility parameters are chemical and physical properties of a material, and the concept predicts the heat of mixing for liquids and amorphous polymers. The dissimilarity in solubility ($\delta_i - \delta_j$) between two substances has commonly been used to assess the ability of a binary system to mix when there is no significant specific interaction, like non-combinatorial entropy effect or hydrogen bonding.

The dissipative force (F_{ij}^D) is directly related to the relative velocity between particles and results in a decrease in their momentum. Conversely, the random force (F_{ij}^R) acts as a counterbalance to the energy lost due to the dissipative force. These two force terms can be given by equation (3.3).

$$F_{ij}^D = -\gamma\omega^D(r_{ij})(\hat{\mathbf{r}}_{ij} \cdot \mathbf{v}_{ij})\hat{\mathbf{r}}_{ij} \quad , \quad F_{ij}^R = \sigma\omega^R(r_{ij})\frac{\xi_{ij}}{\sqrt{\Delta t}}\hat{\mathbf{r}}_{ij} \quad (3.3)$$

The frictional and random forces are characterized by their respective weight functions, $\omega^D(r_{ij})$ and $\omega^R(r_{ij})$, and the amplitude coefficients, γ and σ . According to the theory of Español and Warren [81], the two weight functions have

a mutual dependence on each other, and they are related to the Boltzmann constant and temperature of the system as shown in equation (3.4).

$$\omega^D(r_{ij}) = [\omega^R(r_{ij})]^2 \quad , \quad \sigma = \sqrt{2\gamma k_B T} \quad (3.4)$$

ξ_{ij} represents a randomly generated value with a mean of 0 and a variance of 1 independently for all pairs of interacting particles at all time steps.

According to the Groot et al., the weight functions can be simplified in such a way that $\omega^R(r_{ij})$ has the same form as the conservative force :

$$\omega^D(r_{ij}) = [\omega^R(r_{ij})]^2 = \begin{cases} \left(1 - \frac{r_{ij}}{r_c}\right) \hat{\mathbf{r}}_{ij} , & (r_{ij} < r_c) \\ 0, & (r_{ij} > r_c) \end{cases} \quad (3.5)$$

The final force term is the spring force (F_{ij}^S) related to the bonded harmonic potential energy (U_i^S) than can be expressed as equation (3.6)

$$U_i^S = \sum_b \frac{1}{2} C_b (r_b - r_{b,0})^2 \quad , \quad F_{ij}^S = -\frac{\partial U_i^S}{\partial \mathbf{r}_{ij}} \quad (3.6)$$

In this study, the spring constant (C_b) was established as 4 and the equilibrium bond length ($r_{b,0}$) was set to 0.1 Å for the beads connected to each other in the SMPU polymer chains.

3.2 Derivation of solubility parameters for SMPU copolymer

According to the Flory-Huggins theory, all beads must be modeled to have the same or similar volume in DPD simulations. The volume of monomer, which is a unit of MDI and PEO, each hard and soft segment of SMPU, is shown in Table 3.1. Therefore, 1 MDI and 5 ethylene oxide units are mapped with DPD beads of hard segment and soft segment, respectively, having the same volume (about 250 Å³).

Table 3.1 DPD bead modeling with similar molecular volume for each segment of the SMPU.

	$V_{monomer}$ [Å ³]	No. of monomer per DPD bead	DPD V_{bead} [Å ³]
MDI (Hard segment)	243.65	1	243.65
PEO (Soft segment)	51.03	5	255.15

The cohesive energy (E_{coh}) of each type of DPD was calculated by using AA MD simulation for the solubility theory. The Theodorou-Suter technique available in Material Studio 2016 package was utilized to produce the amorphous unit cells, consisting of MDI and PEO (Figure 3.1 and Table 3.2). Geometry optimization (conjugate gradient), 1ns of NPT ensemble (300 K, 0.1 MPa), and 1 ns of NVT ensemble (300 K) were sequentially performed on each unit cell by using COMPASS (ab initio Condensed-phase Optimized Molecular Potential for Atomistic Simulation

Studies) forcefield [82].

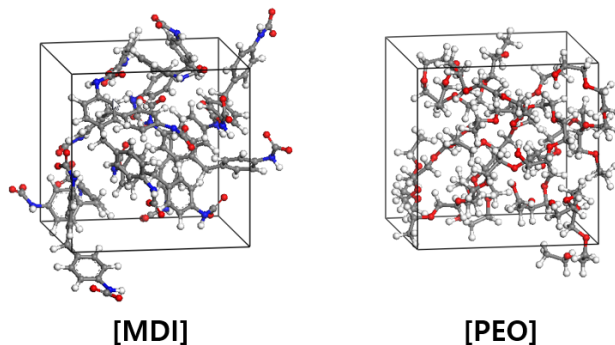


Figure 3.1 Atomistic configurations of pure MDI and PEO MD unit cells. A detailed information is listed in Table 3.1.

Table 3.2 Information on the AA MD unit cells of each segment component of the SMPU copolymer (see atomistic configuration in Figure 3.1).

Unit cell	No. of constituents	Density (g/cm ³)
MDI	10 MDI monomer (10 MDI beads)	1.29
PEO	10 ethylene oxide (EO) pentamers (10 PEO beads)	1.06

The energy values for individual molecules ($E_{isolated,i}$, $i=1-N_{molecule}$) and the bulk system (E_{bulk}) were obtained through a single-point-energy calculation using the fully equilibrated MD unit cell, as described in equation (3.7).

$$E_{coh} = \frac{(\sum_{i=1}^{N_{molecule}} E_{isolated,i}) - E_{bulk}}{N_{molecule}} \quad (3.7)$$

Using the derived cohesive energy (E_{coh}), the solubility parameter (δ in equation

(3.8)) and χ -parameter (equation (3.9)) were calculated sequentially. The variables include the molar volume of the MD unit cell (V), the volume of the DPD bead (V_{bead}) with a 252 \AA^3 , the Boltzmann constant (k_B), and the temperature (T).

$$\delta = \sqrt{E_{coh}/V} \quad (3.8)$$

$$\chi_{ij} = \frac{V_{bead}}{k_B T} (\delta_i - \delta_j)^2 \quad (3.9)$$

Then, the repulsion parameter for two different beads was derived by using the obtained χ -parameter. Equation (3.10) was developed by Groot. et al. [80] under the condition of a dimensionless bead density ($\rho = 3$). To achieve the same compressibility of water, the repulsion parameter between the same type of beads was fixed to $a_{ii} = 25$ [80].

$$a_{ij} = a_{ii} + \frac{\chi_{ij}}{0.286} \quad (a_{ii} = 25, \rho = 3) \quad (3.10)$$

Therefore, in the DPD simulation, how much the repulsion parameter between different beads is greater than or less than 25 is very important for the mixing behavior of dissimilar materials. Tables 3.3 and 3.4 show the derived solubility parameters and the resulting repulsion parameter values.

Here, only the self interaction parameter between urethanes was used as 22.5 instead of 25 as an exception, meant to represent the hydrogen bonding between MDIs [83,84].

Table 3.3 Solubility parameter (δ) of pure MDI and PEO system cacluated from AA MD simulations.

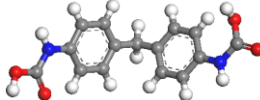
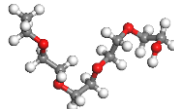
Solubility parameter δ ($\sqrt{J/cm^3}$)	
MDI	PEO
	
28.71	23.14

Table 3.4 Repulsion parameter (a_{ij}) between SMPU DPD beads.

a_{ij}	MDI	PEO
MDI	22.5	
PEO	31.59	25

Additionally, in order to conduct the DPD simulation, it is necessary to establish the reduced units for mass, length, and energy scales. The unit of mass is represented by the average mass of the DPD particles. The unit of length is defined as the length at which the dimensionless bead density of a cube of unit length is 3 ($\rho = 3$). The unit of energy is established as $k_B T$ set to 1. It is possible to calculate the reduced time scale using these defined unit quantities. The formula for the reduced units and the values calculated in this work are shown in Table 3.5.

Table 3.5 Information on the reduced units of DPD simulation

DPD unit	Equation	Reduced unit
Length scale	$L = (V_{bead} * 3)^{\frac{1}{3}}$	9.1112 Å
Mass scale	$M = M_{bead}^{avg}$	230 – 264 amu
Energy scale	$E = k_B T$ (300 K)	0.59616 kcal/mol
Time scale	$t = L\sqrt{M/E}$	8.75 – 9.37 ps

The mass scale used the average mass of beads according to the HSC (15 – 50 wt.% in section 3.3) of the SMPU, and the time scale value was determined accordingly. The values of reduced unit at each scale in Table 3.5 are all defined as 1, which is a unit scale, in DPD simulation. In the dissertation, all MD and DPD simulations were performed using a high performance computing (HPC) cluster, specifically an Intel Xeon E5-2650 Octa Core 2.2 GHz CPU with 16 cores. When the same 10 ns ensemble simulation was performed for the unit cells used in this study through reduced degrees of freedom and increased time steps in mesoscale models, the computational time, which was 40 hours (all-atom MD), drastically reduced by 3.4 hours (CG MD) and 0.6 hour (DPD).

3.3 Morphologies of phase-separated SMPU

SMPU DPD models with a much higher molecular weight ($3.33 \sim 5.72 \times 10^5$ g/mol) than the polymer chains of the existing all-atom and CG model was constructed for 5 different HSCs (15, 21, 32, 45, 50 wt.%). As shown in Figure 3.2,

while the number of MDI beads was changed according to HSC, the number of PEO beads was fixed,

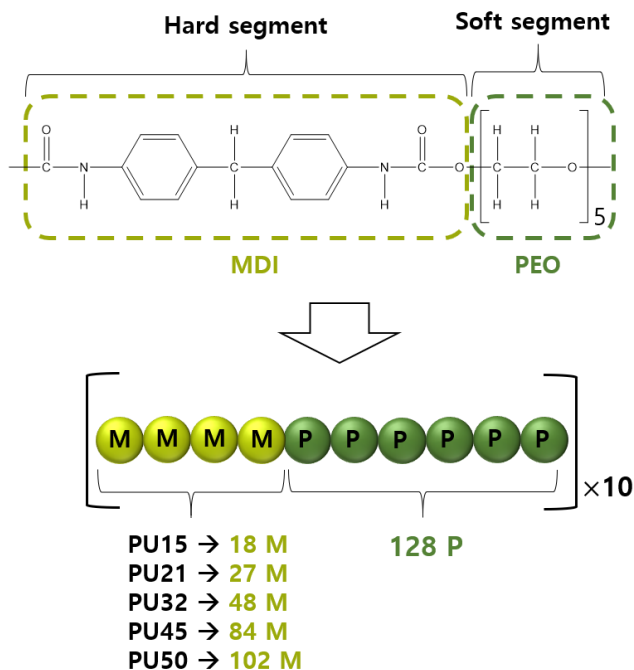


Figure 3.2 Modelling of the SMPU copolymer chains for DPD simulations.

The DPD unit cells were constructed using the SMPU chains. All unit cells were modeled to have a size of $30L \times 30L \times 30L$ ($27.3 \text{ nm} \times 27.3 \text{ nm} \times 27.3 \text{ nm}$) through DPD reduced unit. The time scale of the DPD simulation was set to $\tau = 0.05t$, the energy scale (temperature) to 1, the cutoff distance to 1, and the total simulation time to $2 \times 10^5 \tau$.

Since the dimensionless bead density is 3 ($\rho = 3$), the corresponding unit cell is composed of about 8×10^4 DPD beads. The unit cell size and total simulation time used in this simulation were used with values larger than sufficient values to reach

the equilibrium state used in several DPD studies [85-88].

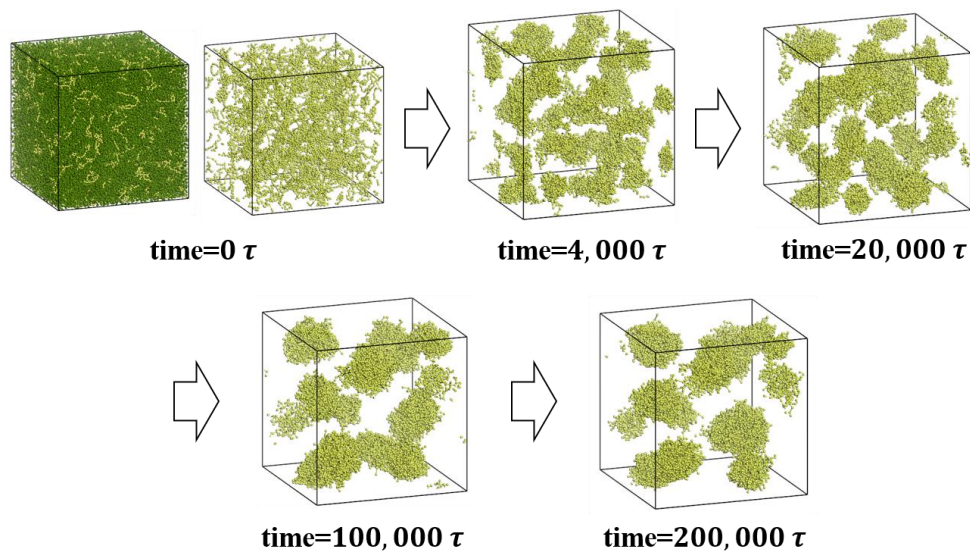


Figure 3.3 Phase separation morphology of PU15 according to time step by DPD simulation. Yellow bead represents MDI bead and green bead represents PEO bead. To illustrate the phase domain more effectively, green PEO beads are hidden from the unit cell.

Figure 3.3 shows the architectural evolution of the phase domains according to the time step as a result of the DPD simulation of the PU15 model. Here, yellow beads represent MDI beads and green beads represent PEO beads. After the initial configuration, the PEO bead was hidden from view to visualize the morphology of the hard phase domain. The MDI beads, initially spread in the hard-soft mixed phase, gradually aggregated, showing a phase morphology that reached an almost equilibrium state after $t = 100,000\tau$. The hard phase in the final configuration builds a "Spherical-shape" domains and the phase architecture of MDI is completely

distinct from the overall shape memory polyurethane morphology. The phase-separated SMPU is the result of DPD simulation, which comprehensively reflects MDI's hydrogen bonding ($a_{ii} = 22.5$) and hard-soft incompatibility ($a_{ij} = 31.59$).

According to a reference [90,91], when the content of hard segments increases in SMPU block copolymers, the hard segments tend to aggregate more and form domains. The MDI-based shape memory polyurethanes is primarily determined by MDI, which holds a permanent shape. Figure 3.4 displays the structural evolution of the MDI phase in our systems with varying HSCs in the simulation box. To illustrate the phase domain connections and distributions more effectively, we show the phase domains in the $2 \times 2 \times 2$ unit cell with periodic boundary conditions (PBC).

As described above, as shown in Figure 3.3 and 3.4, the MDI phase at 15 wt.% of HSC exists in the shape of spherical particles. It exists as an isolated domain area in the middle of the soft phase domain, and each domain area is not connected. SMPU is a copolymer chain that consists of a hard segment and a soft segment, but this phase architecture looks like a nanofiller added to a polymer matrix with different properties. This result is also aligns well with the experimental results [92-94] showing spherical hard segment domains in polyurethane with low hard segment content, which validates our DPD model.

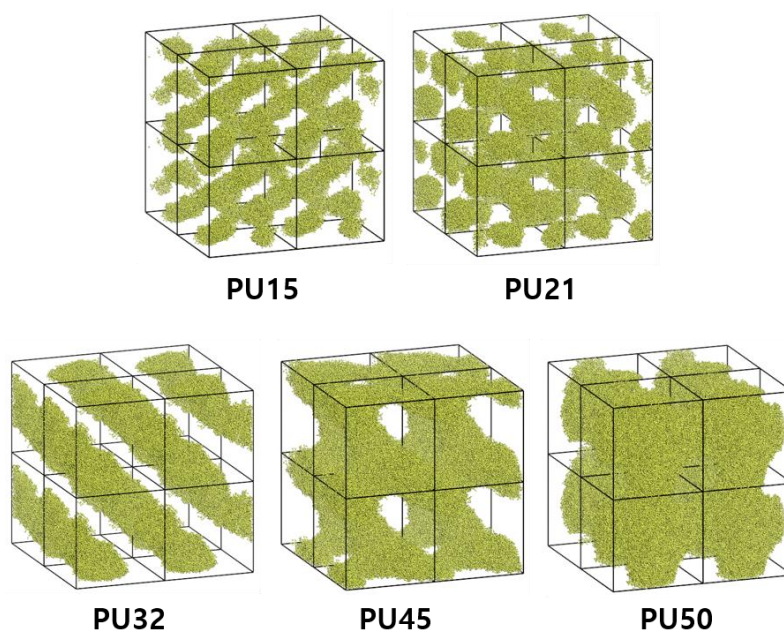


Figure 3.4 Hard domain connections and distributions of the SMPU according to the HSCs (15, 21, 32, 45, and 50 wt.%) in $2 \times 2 \times 2$ periodic unit cells.

In the HSC 21 wt.% model, similar phase domains were formed, and worm- or rod-shape domains [95,96] with slightly larger hard clusters were additionally formed. In the case of PU32, it was found that a stronger connection was formed between the MDI beads in a specific direction. Therefore, it was found that the hard segment in a single unit cell existed in the form of several cylindrical shapes [96-98], and this structure formed an alternating hard-soft lamellar structure in a $2 \times 2 \times 2$ periodic unit cell. In this structure, the lamellar thickness and interlamellar space can be changed by the molecular composition or chain length of SMPU [94,98,99], and this microdomain structure can have a great effect on the thermomechanical properties of segmented polyurethane copolymer. In PU45 with a larger HSC, a

stronger interconnection between hard domains was created, and the hard domain in PU50 was found to exist as a continuous area that links and dominates the entire system, which align well with earlier research [97].

The MDI topological architectures can represent the netpoints of networks similar to shape-memory polyurethane models. As the HSC increases, the network gains greater strength and resilience. In this specific range of HSC (Hard-Segment Content), the hard-segment phase undergoes a transition from being isolated and discontinuous to becoming interconnected and continuous. In addition to the basic mechanism of each segment found in the CG model in section 2, the phase structure in the microdomain can be understood through the repulsion by the clearer solubility difference of the DPD simulation.

Figure 3.5 summarizes the architectural evolution of MDI (hard domain) according to the SMPU's molecular composition, and shows the resulting overall hard-soft phase-separated morphology. To view the phase morphology in Figure 3.4 more efficiently, Figure 3.5 shows a specific side view or inside cross-section view. Our proposal is that the architectural evolution of the phase domain in a unit cell, as demonstrated in Figure 3.5, can represent the SMPU model with varying hard segment contents. As the HSCs increase from 15 wt.% to 50 wt.%, the isolated spherical MDI structure transitions into a rodlike structure, followed by cylindrical/lamellar and finally an interconnected/continuous configuration. The mesoscale result through DPD simulation is consistent with the experimental result [100] that the hard segment of thermoplastic polyurethane develops from an isolated

phase to an interconnected phase according to HSC. It is also consistent with previous studies [97,122,123] that alternating hard and soft lamellar structures with interdomain spacings of approximately 10–20 nm appear in HSCs greater than about 30 wt.%.

The block copolymer's different chemical components serve different roles in the molecular mechanism of the dual-segment system. The MDI domain functions as the netpoint, while the PEO phase functions as the switch. With varying HSCs, the components may exhibit different phase architectures. In our CG study in section 2, we observed that SMPUs with lower HSCs exhibited better shape fixing ability. This is because, with lower HSCs, the PEO phase acts as a filling matrix without interconnections among the spherical MDI domains, leading to excellent shape fixation. Conversely, for higher HSCs, the PEO and MDI form linked-continuous phases, resulting in lower shape fixity. The decrease in shape-recovery performance may be attributed to the hard-segment phase changing from spheres to continuous domain. In terms of shape memory performance, the model in which the soft-segment is the major matrix phase and the hard-segment forms the isolated phase is the optimized design. In this design, the crystalline polymer provides excellent fixing and unfixing performance, and the hard-domain also hardly reduces recovery performance. Our structural shape-memory model (Figure 3.5) involves the full description of phase domains for the two segments in SMPU and covers all the phase morphologies in the literatures [90-100] to verify the rationality of the DPD models and highlight the specific characteristics of shape memory polymers.

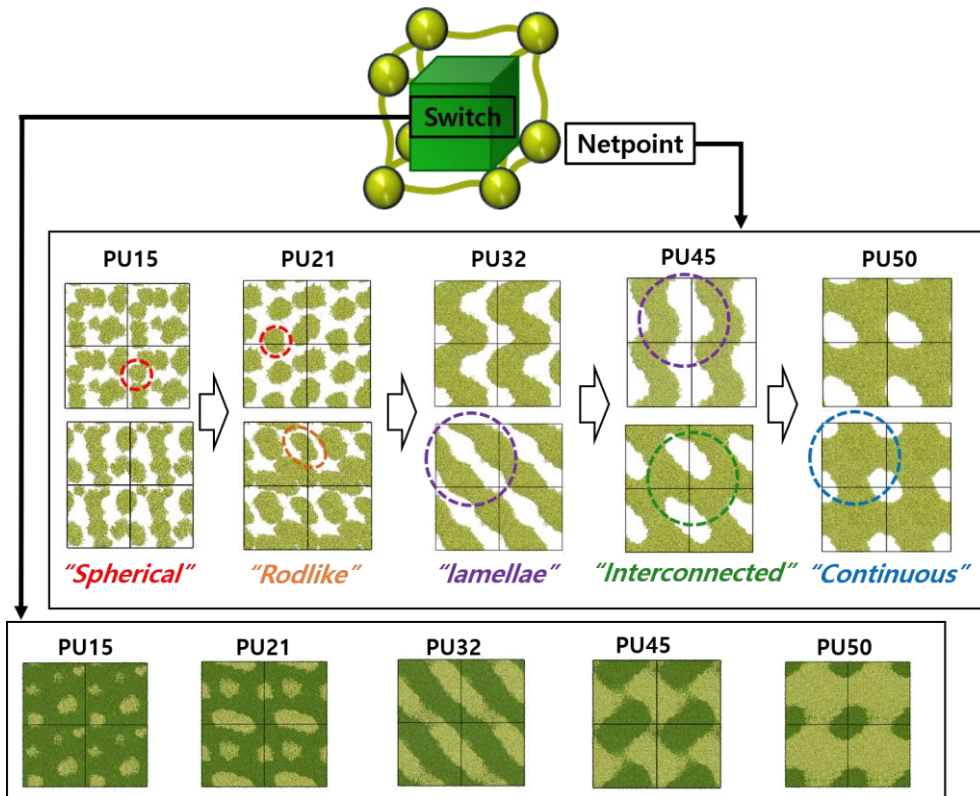


Figure 3.5 Summarization of the architectural evolution of phase morphologies according to HSC of the SMPU.

Chapter 4

Multiple phase separation behaviors of SMPU – Silica nanocomposites

4.1 Morphologies of phase-separated SMPU nanocomposites

4.1.1 Mixing energy and Flory-Huggins parameters between silica nanoparticle and polymer

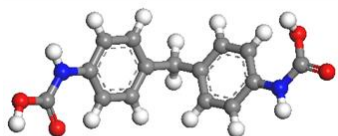
The distribution and clustering behaviors of silica nanoparticles can greatly affect the thermo-mechanical properties or electrical conductivity properties of SMPU nanocomposites. Therefore, silica nanoparticles also need to be applied to DPD simulation to observe multi phase separation behavior.

As in section 3.2, the DPD bead should be defined to have a volume similar to 250 \AA^3 for silica nanoparticles. Therefore, as shown in Table 4.1, five SiO_2 , which

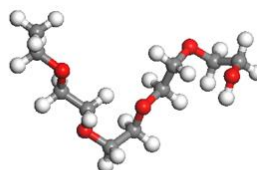
is a constituent unit of silica nanoparticles, are defined as one bead. Here, in owing to accurately capture the interaction between silica nanoparticle and SMPU polymer matrix and reflect it with different repulsion parameters, the core part of the nanoparticle and the shell part containing the hydroxy silanol group (Si-O-H) were divided. Figure 4.1 shows four different bead systems defined in DPD simulation of SMPU-Silica.

Table 4.1 DPD bead modeling of silica nanoparticle system.

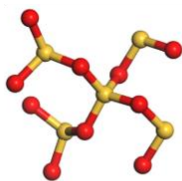
	$V_{monomer}$ [Å ³]	No. of monomer per DPD bead	DPD V_{bead} [Å ³]
SiO ₂ (Silica nanoparticle)	51.52	5	257.6



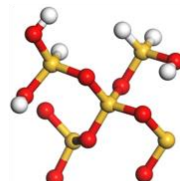
[MDI bead]



[PEO bead]



[Core bead]



[Shell bead]

Figure 4.1 Molecular unit segments constituting each bead of DPD.

In section 3, we established the DPD repulsion parameters for the segment components of the SMPU by using a relationship between well-known Flory-Huggins theory and the solubility parameter of polymer materials. However, this method is not suitable for deriving the interaction between solid SiO₂ particles and polymers, and a general theory has not been established.

Hence, we have chosen to use a blend method that merges a modified Flory-Huggins model with Monte Carlo simulation. This technique allows us to compute the χ parameters by directly analyzing the mixing energy between different types of beads. This method has been successfully used in other DPD studies [101-103] to calculate the interaction of gold nanoparticles or any binary systems. We used the blend module of Material Studio 2016 package.

Based on the work of Ryikinaet et al. [103], the average interaction energy among bead pairs can be determined by computing the mixing energy of two corresponding fragments:

$$E_{ij}^{mix} = \frac{1}{2} (Z_{ij} \langle E_{ij}(T) \rangle + Z_{ji} \langle E_{ji}(T) \rangle - Z_{ii} \langle E_{ii}(T) \rangle - Z_{jj} \langle E_{jj}(T) \rangle) \quad (4.1)$$

The Z_{jj} refer to the calculated coordination numbers of each pair of fragments. The average pair interaction energy ($\langle E_{ij}(T) \rangle$) was calculated using Monte Carlo sampling, considering 10,000 possible conformations of a pair of molecules in contact at a temperature of 300 K:

$$\langle E_{ij}(T) \rangle = \frac{\int dE_{ij} P(E_{ij}) E_{ij} \exp(-E_{ij}/k_B T)}{\int dE_{ij} P(E_{ij}) \exp(-E_{ij}/k_B T)} \quad (4.2)$$

where k_B is Boltzmann constant. Each pairs of mixing energiey between differencnt types of beads (Figure 4.1) was averaged with 1,000,000 energy smaples calculated from the cluster samples, and the Flory-Huggins parameter ($\chi_{ij}(T)$) between bead i and j was obtained by

$$\chi_{ij}(T) = \frac{E_{ij}^{mix}}{RT} \quad (4.3)$$

The repulsion parameters (a_{ij}) between each beads were calculated by equation (3.10) in the same way, and the derived χ_{ij} and a_{ij} valules are shown in Table 4.2 and 4.3, respectively.

Table 4.2 Flory-Huggins parameter (χ_{ij}) between DPD beads of SMPU/Silica nanocomposites.

χ_{ij}	MDI	PEO	Core	Shell
MDI				
PEO	1.884			
Core	17.96	3.259		
Shell	11.18	2.454	0.729	

Table 4.3 Repulsion parameter (a_{ij}) between DPD beads of SMPU/Silica nanocomposites.

a_{ij}	MDI	PEO	Core	Shell
MDI	22.50			
PEO	31.59	25		
Core	87.81	36.40	25	
Shell	64.11	33.58	0.729	25

Looking at the calculated repulsion parameter value, it seems that a higher affinity of the silica particle towards the soft segment PEO in comparison to the hard segment MDI, which is consistent with the experimental finding [104] that polyols strongly interact with nanosilica. These DPD models derived through solubility and mixing energy are more efficient in observing the phase separation and nanoparticle distribution of SMPU nanocomposites than the coarse-grained model that accurately simulates the structure of each segment through the IBI method in section 2.

4.1.2 Nanoparticle clustering behaviors

The distribution and dispersion characteristics of silica nanoparticles can greatly affect the thermo-mechanical properties or electrical conductivity properties of SMPU nanocomposites. Therefore, silica nanoparticles also need to be applied to DPD simulation to observe multi phase separation behavior. We constructed DPD silica nanoparticle with a radius of 30 angstroms. The silica segments in Figure 4.1c and 4.1d were treated as each beads, and the bond length between the beads in the

nanoparticles was 5.3261 Å. The spring constant between the silica beads was set to 350 to prevent the size change of nanoparticles during DPD simulation ($C_b = 350, r_b = 5.3261 \text{ Å}$). Here, the time step was modified to $\tau = 0.04t$ for more stable relaxation of the unit cell with strong bonded potentials, and the total simulation time to $2.5 \times 10^5 \tau$. Similar to the CG model in section 2.3, we added three different amounts of silica nanoparticles, which are 3 wt.%, 6 wt.%, and 10 wt.%, to PU15, PU32, and PU50 in section 3.3.

First, we modeled a nanoparticle composed of only core beads assuming humed silica nanoparticles whose surface was not doped with silanol groups (S-OH) [105-106]. Figure 4.2 shows the architectural evolution according to the time step as a result of the PU15 with 10 wt.% of silica nanoparticles. Here, yellow beads are MDI beads, green beads are PEO beads, and navy beads are silica Core beads. What is noteworthy here is that all silica nanoparticles are distributed in the soft-segment (PEO) domain region. This finding is the result of the DPD repulsion parameters between silica and MDI ($a_{ij} = 87.81$), and between silica and PEO ($a_{ij} = 36.40$), which reflects the mixing energy derived by considering the chemical interaction at the atomistic level.

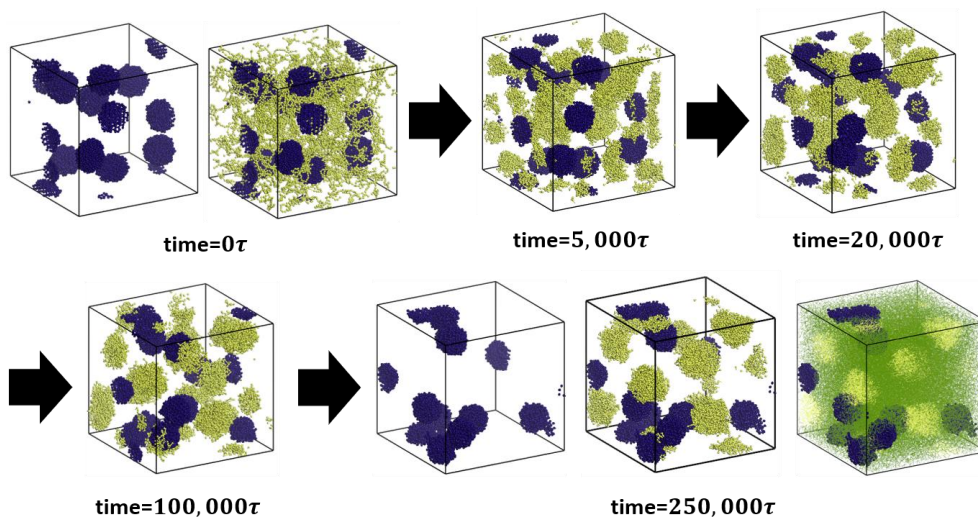


Figure 4.2 Multiple phase separation morphology of PU15/Silica nanocomposite according to time step by DPD simulation. Yellow bead represents MDI bead, green bead represents PEO bead, and navy beads represent silica Core beads..

These results add reliability to the compatibility issue between nanoparticles and each segment of the polymer matrix predicted through the CG models in section 2.3, and the resulting nanoparticle clustering behaviors and shape-memory performances. In addition, DPD simulation reflecting the solubility parameter and mixing energy provides a more accurate breakthrough in understanding and designing the realistic distribution of nanoparticles.

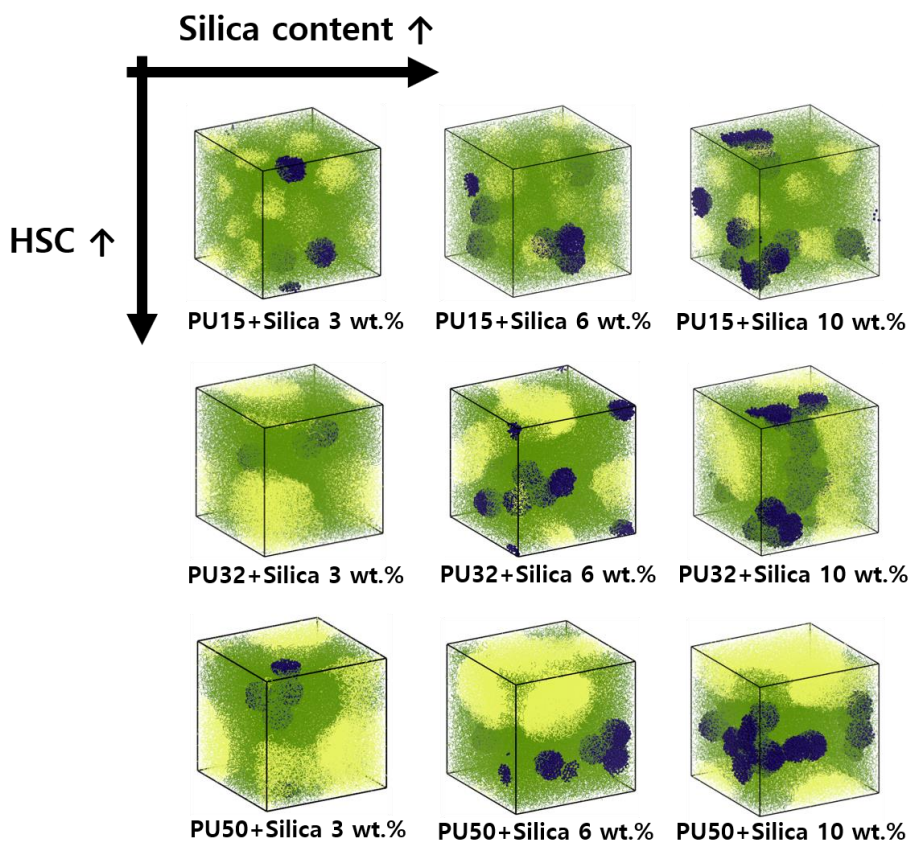


Figure 4.3 Final snapshots of DPD simulation results for different HSCs and silica nanoparticle contents (Silica with only Core beads).

Figure 4.3 shows the final phase morphologies of 9 different SMPU nanocomposites according to the HSC and silica content of the DPD unit cell. The phase domains of the polymer matrix in nanocomposites follow the segment morphology of the pristine SMPU copolymer in section 3.3. As the HSC of SMPU increases, the hard domain has an extended area from spherical shape to continuous domain. As in the previous Figure 4.2, all silica nanoparticles exist in the soft domain in all models. Figure 4.4 illustrates the phase morphologies acquired from $2 \times 2 \times 2$

cells with PBC, aiming to present the interconnections and distributions in the phase domain more effectively. As shown in Figure 4.4a, in PU15, silica nanoparticles are evenly distributed in the soft matrix area except for the hard spherical filler area. In PU32, since the hard and soft segment regions form an alternating lamellar shape, the nanoparticles tend to be distributed along the wave line of the soft domain (Figure 4.4b). According to Figure 4.4c, in PU50, silica nanoparticles seem to be relatively aggregated in the soft region outside the continuous hard domain region. This is the result of multiple phase separation due to differences in compatibility between different components (MDI, PEO, Core) of SMPU nanocomposites.

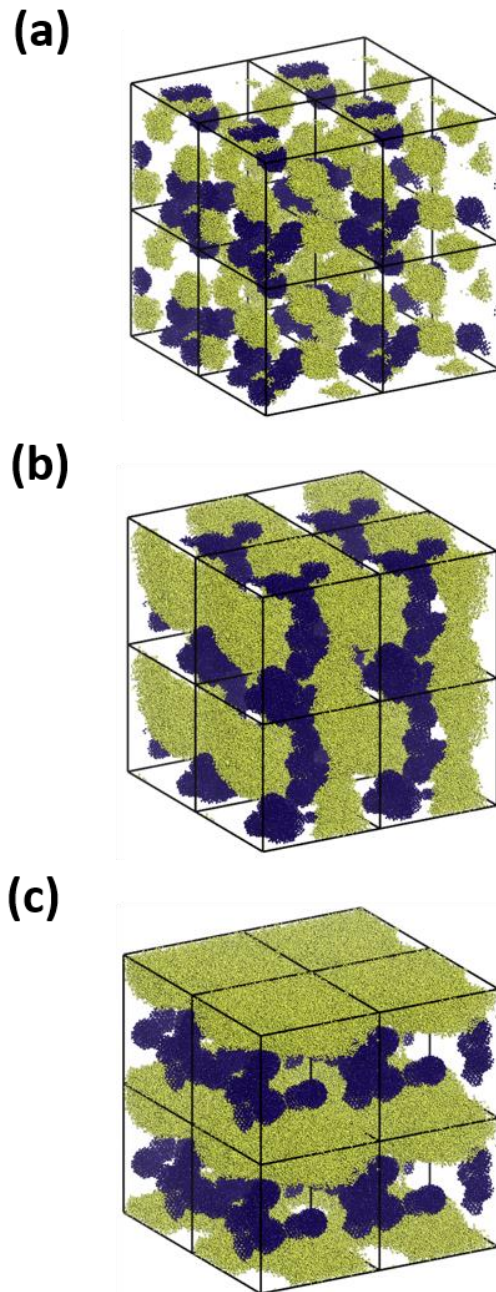


Figure 4.4 Phase domain morphologies of the SMPU matrix and silica nanoparticle distributions (10 wt.%) for HSC (a) 15 wt.%, (b) 32 wt.%, and (c) 50 wt.% in $2 \times 2 \times 2$ periodic unit cells.

To further investigate the nanoparticle clustering behaviors, we quantified the extent of nanoparticle agglomeration at the nanoscale. We derived the clustering density (C) derived from the volume fraction of the interphase region in the actual unit cell (V_{real}) compared to the ideal well-dispersed case ($V_{well-dispered}$). To calculate the clustering density, we assumed an interphase region with a thickness of 10 Å from the nanoparticle surface.

$$C = A \times \left(1 - \frac{V_{real}}{V_{well-dispered}} \right) \quad (4.4)$$

Here, a normalization constant ($A=3.23$) was utilized to scale the clustering density to 1 when the 10 wt.% of silica nanoparticles were perfectly agglomerated. The difference in nanoparticle agglomeration can be clearly seen through the clustering density according to HSC and silica content in Figure 4.5. It can be seen that the higher the silica content in each HSC, the higher the clustering density. As the nanoparticle content increases, particle aggregation becomes an inherent phenomenon, leading to a reduction in surface free energy. This occurs as the particles adhere to one another, leading to a growth in their size and a reduction in their surface area [107].

In addition, as expected from our results, even if the silica content is the same, it can be confirmed quantitatively that the clustering density increases as the HSC increases. It can be seen that nanoparticles are excessively aggregated in PU50 due to incompatible solubility between silica nanoparticles and MDI. We propose a silica surface treatment strategy to improve this nanoparticle clustering phenomenon in section 4.2.

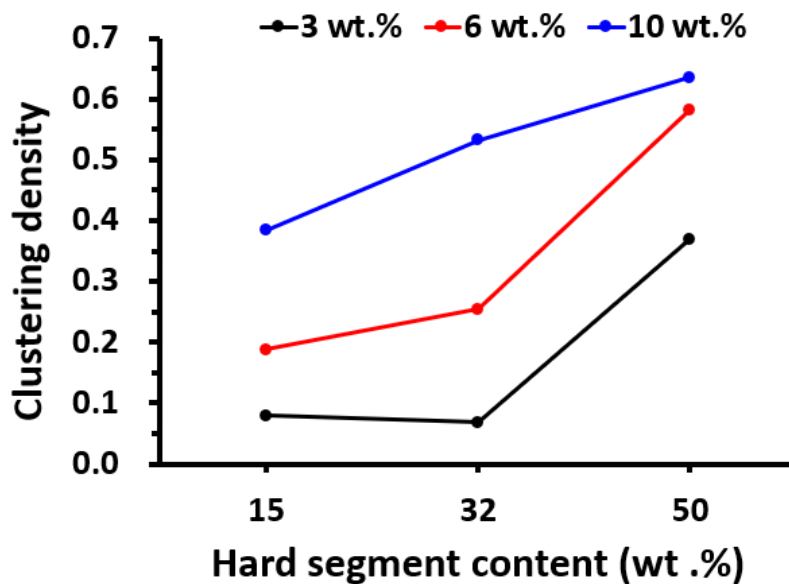


Figure 4.5 Clustering density results as a function of HSC at different silica contents.

4.2 Effect of silica nanoparticle surface treatment

The region between nanoparticles and a polymer matrix, known as the interphase region, can differ based on the properties of the nanoparticle and polymer surfaces. Modifying the surface of the nanoparticles can enhance the interaction and compatibility of the interphase, thereby enhancing the overall quality of nanocomposites [108,109]. Silica nanoparticles have different interactions with the polymer matrix depending on the surface treatment effect, and as a result, the degree of agglomeration of the nanoparticles can be improved.

As shown in Figure 4.6, three additional surface treatment materials were

introduced in addition to the silanol group (Shell bead) to improve the compatibility of the silica nanoparticle with the SMPUs. The materials are polydimethylsiloxane (PDMS), octylsilane (OS), and 3-aminopropyltrimethoxysilane (APTS), which have been used for silica surface treatment to reduce aggregation in several experimental studies [110-115].

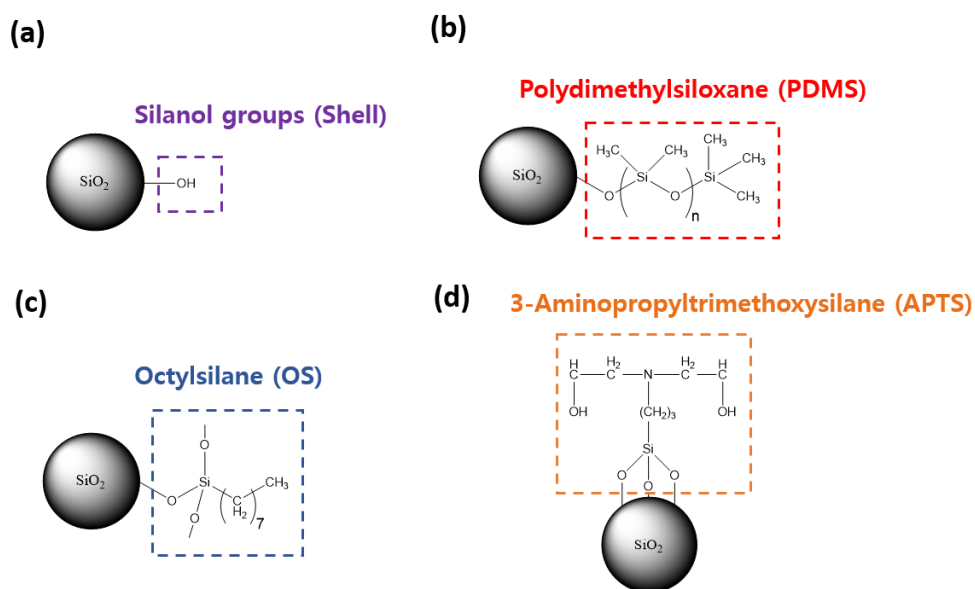


Figure 4.6 Chemical structure of silica surface treatment materials (a) silanol groups (Shell bead), (b) polydimethylsiloxane (PDMS bead), (c) Octylsilane (OS bead), and (d) 3-aminopropyltrimethoxysilane (APTS bead).

We derived the Flory-Huggins parameter and DPD repulsion parameter values through mixing energy calculation between existing bead segments (MDI, PEO, Core, and Shell) and PDMS, OS, and APTS materials via equation (4.1)-(4.3) in section 4.1.1. The derived χ_{ij} and a_{ij} values are shown in Table 4.4 and 4.5,

respectively.

Table 4.4 Flory-Huggins parameter (χ_{ij}) for silica surface treatment materials.

χ_{ij}	MDI	PEO	Core	Shell
PDMS	20.08	2.820	0.543	1.284
OS	10.18	0.901	0.692	0.169
APTS	9.029	-0.252	2.008	-0.309

Table 4.5 Repulsion parameter (a_{ij}) for silica surface treatment materials.

a_{ij}	MDI	PEO	Core	Shell
Core	87.81	36.40		
Shell	64.11	33.58	27.55	
PDMS	95.22	34.86	26.90	29.49
OS	60.60	28.15	27.42	25.59
APTS	56.57	24.12	32.02	23.92

Looking at the derived repulsion parameter results, the surface of the silica nanoparticle exhibits varying interactions with the polymer matrix (MDI and PEO) contingent upon the specific functional group introduced to the silicon dioxide. As the repulsion between the polymer matrix and the nanoparticle decreases, a more stable and wider interphase region can be formed and uniform distribution can be achieved. Basically, the silanol surface, the Shell bead, has better compatibility with the polymer matrix (smaller repulsion parameters) than the Core bead due to the

hydrogen bonding between silica surface and SMPU. The surface-treated silica with PDMS bead has rather more repulsion with MDI and PEO than the Core bead as well as the Shell bead. In this case, where the force to push each other with the hard and soft segments becomes greater, it will result in nanoparticles being more agglomerated, with poor compatibility with the polymer matrix. In OS and APTS materials, the repulsion with MDI and PEO is both reduced compared to the existing silanol-doped silica surface, and it is expected that the nanoparticle distribution can be improved by enhancing the affinity with the SMPU matrix. In particular, in APTS, the repulsion with MDI and PEO decreased the most, and the repulsion parameter with PEO was 24.12, lower than $a_{ii} = 25$, which significantly improved compatibility with soft segments. In addition, since the APTS beads increase the repulsive force with the Core beads compared to the Shell beads, further improvement in nanoparticle distribution can be expected.

Therefore, following the nanoparticle made of only the Core bead in section 4.1.2, DPD simulations were performed for the basic Shell bead and APTS bead among the surface treatment candidates. In addition, from the viewpoint of improving compatibility between SMPU and nanoparticles, MDI and PEO beads, which are the matrix itself, can be considered as one of the best candidates for surface treatment. Therefore, additional DPD simulation was performed for the models surface treated with MDI and PEO beads on the Core beads. Therefore, we constructed 10 wt.% of silica nanoparticles of five different types as shown in Figure 4.7. "Core" refers to silica nanoparticles composed of only Core beads. The

remaining "Shell", "APTS", "MDI", and "PEO" represent nanoparticles in which the surface of silica nanoparticles are replaced with other corresponding beads.

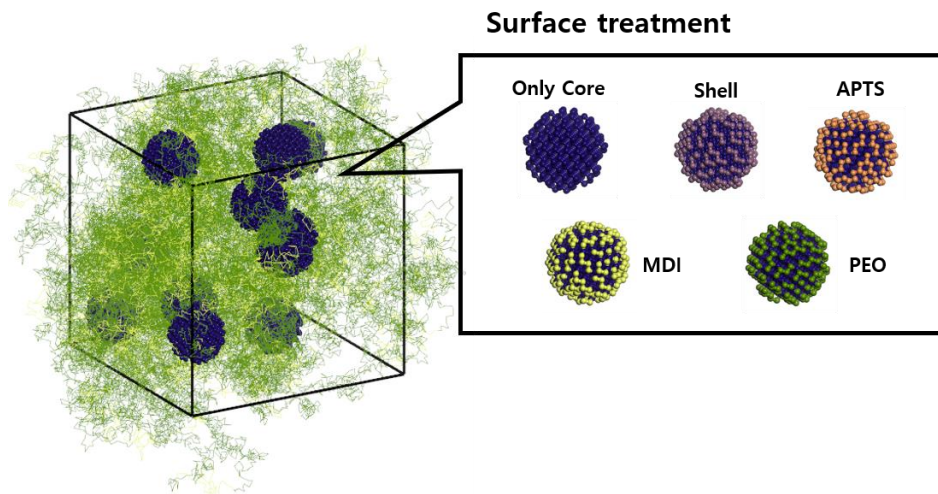


Figure 4.7 DPD modeling of silica surface treatment of SMPU/silica nanocomposites.

Figure 4.8 shows the DPD simulation results of PU15, PU32, and PU50 with various silica surface treatments (only Core, Shell, APTS, PEO, and MDI). Basically, silica nanoparticles surface-treated with Core, Shell, APTS, and PEO beads are distributed in the soft segment region of the SMPU matrix because they have better compatibility with the soft segment than with the hard segment. The Core model without surface treatment has the strongest repulsive force with the SMPU matrix, so it can be seen that the nanoparticles are agglomerated the most among themselves compared to other models as shown in Figure 4.8. Unlike the other four models, in the model treated with MDI, nanoparticles are distributed in the hard domain area,

causing additional connections between the surrounding hard domains.

Since all surface treatment materials complement the overall chemical dissimilarities between the primary Core bead and the SMPU matrix, we can expect a more uniform distribution of nanoparticles. According to Tables 4.3 and 4.5, the compatibility with the soft segment is improved in the order of Core \rightarrow Shell \rightarrow MDI \rightarrow PEO \rightarrow APTS, and the compatibility with the hard segment is improved in the order of Core \rightarrow Shell \rightarrow APTS \rightarrow PEO \rightarrow MDI. The final uniformity of silica nanoparticle distribution will be determined by the interaction between the nanoparticle and each segment and the hard-soft ratio in the SMPU matrix.

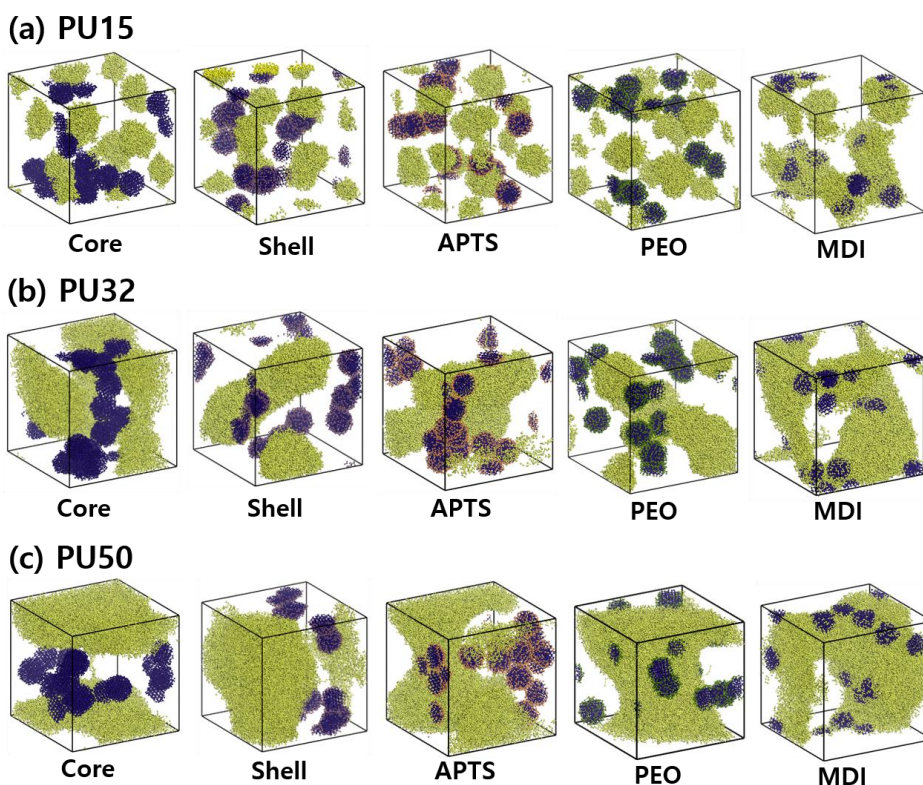


Figure 4.8 Distributions of silica nanoparticles as a result of DPD simulation

according to HSC (a) 15 wt.%, (b) 32 wt.%, and (c) 50 wt.% and silica surface treatment of SMPU/Silica nanocomposites.

Figure 4.9 shows the clustering density value that quantifies the degree of improvement of nanoparticle distribution as in section 4.1.2. In SMPU with all HSCs, the clustering density decreased in all four different surface treatment materials, which means that the distribution of nanoparticles was improved. However, depending on HSC, the degree of improvement and ranking according to the surface treatment materials are different.

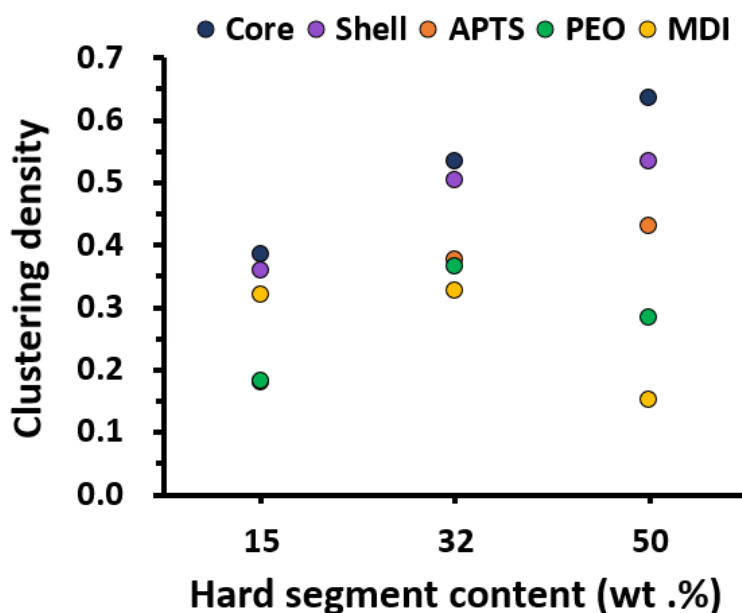


Figure 4.9 Clustering density change according to nanoparticle surface treatment of SMPU/Silica nanocomposites.

In PU15 (HSC 15 wt.%), the soft segment is dominant in the SMPU matrix.

Therefore, the degree of repulsion between the silica nanoparticle and PEO (soft segment) is important at this time. As a result, the clustering density decreased as the repulsion parameter between the PEO and the surface bead decreased. The distribution of nanoparticles gradually improved in order from Core to Shell, MDI, PEO, and APTS, and the APTS surface treatment, which had the best affinity with the soft segment ($a_{ij} = 24.12$), showed the lowest clustering density.

In PU32 (HSC 32 wt.%), however, the APTS surface treatment had a higher clustering density than the PEO and MDI surface treatments. The reason is that APTS has the best affinity with the soft segment, while its repulsion with the hard segment is relatively strong. Since the repulsion between APTS and MDI ($a_{ij} = 56.57$) is a stronger repulsive force than the repulsion between hard and soft matrices ($a_{ij} = 31.59$), the APTS model overall has less affinity with the SMPU matrix than the model using MDI or PEO itself for surface treatment. Even though the content of the is still higher than that of the hard segment in the PU32, the reason why MDI surface treatment has more uniform nanoparticle distribution than PEO surface treatment is that the very strong repulsion between the existing Core bead and hard segment ($a_{ij} = 87.81$) is improved to strong adhesion ($a_{ii} = 22.5$) between MDIs.

In PU50, the clustering pattern is similar to that in PU32, and the order of clustering density according to the surface treatment is also the same. However, in SMPU with HSC 50 wt.%, the hard segment with a much higher proportion than PU32 forms a continuous domain, so the improvement effect on nanoparticle agglomeration is maximized in the MDI surface treatment model. In other words, it

can be seen that the improvement effect of nanoparticle agglomeration in a phase-separated copolymer system such as SMPU matrix is maximized when one segment occupies a dominant portion in the polymer matrix and compatibility with the domain is the best. This explanation is verified in Figure 4.9 by showing that the lowest value of clustering density in each HSC of the SMPU is smaller in PU15 and PU50 than in PU32. Figure 4.10 shows the improvement effect of nanoparticle distribution through optimal surface treatment on PU15 and PU50 in more detail. The highly aggregated silica nanoparticles are spread relatively uniformly in the polymer matrix through surface treatment, and this change has a critical effect on forming a wider and more stable interphase region in terms of nanocomposite performance.

The DPD simulation of this study presents a very innovative design technique in terms of nanoparticle distribution in polymer nanocomposites. If only the solubility difference or mixing energy between various heterogeneous materials can be derived, the nanoparticle distribution can be predicted through the repulsion parameter. Nanocomposite design through testing and development of these surface treatment materials is time-consuming and has limitations on accurate distribution analysis in the nanometer level through experiments. If we analyze the clustering tendency in Figure 4.9 according to the value of the repulsion parameter in Table 4.5, we can predict the particle distribution even without DPD run if only the solubility difference or mixing energy with the components is derived for any unknown material. We can expect that the octylsilane (OS) model will have an intermediate

clustering density of the Shell and APTS models. This mesoscale simulation-based multiscale analysis technique is an essential research for the completion of nanocomposite design.

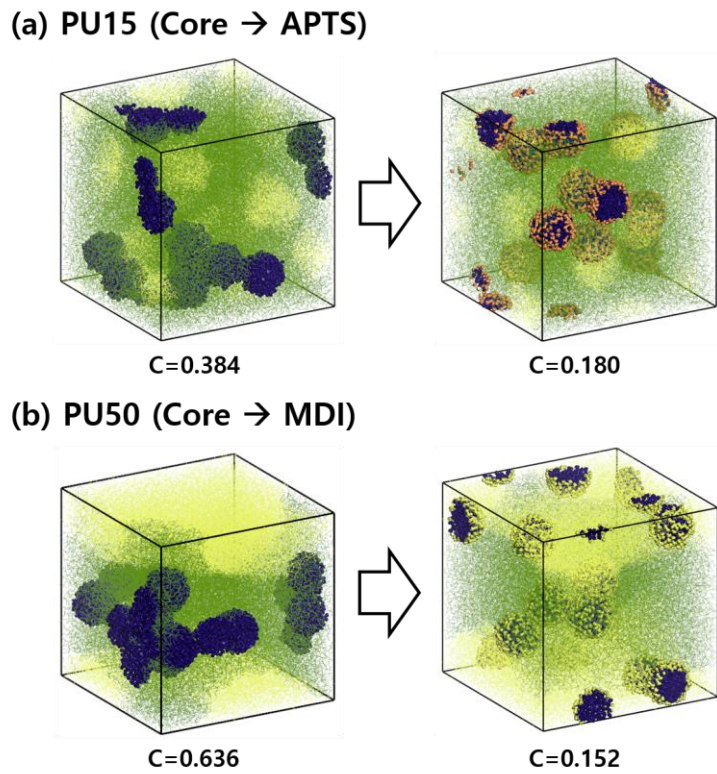


Figure 4.10 Nanoparticle distribution improvement effect by optimal silica surface treatment in (a) PU15 and (b) PU50.

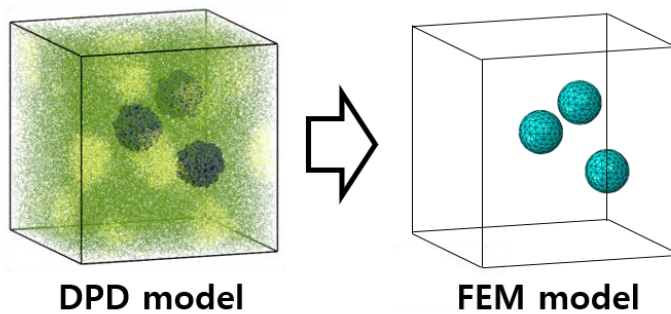
4.3 Multiscale continuum model for mechanical properties

4.3.1 Multiscale two-phase homogenization and verification

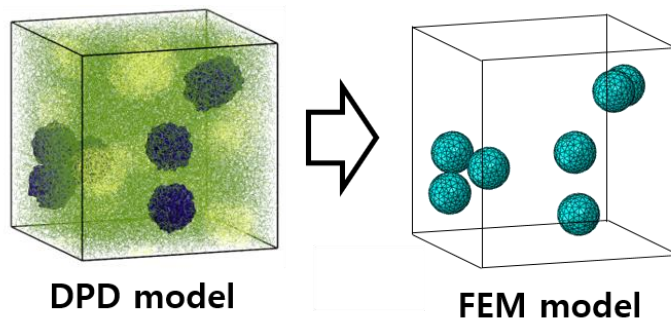
To examine how nanoparticle distributions influence the homogenized mechanical properties of nanocomposites, we developed finite element models for continuum scale. The nanoparticle coordinates within the unit cell were derived from the nanocomposites final geometry, obtained through DPD simulations. To perform finite element analysis, we employed commercial software tools DIGIMAT and ABAQUS, and integrated the acquired geometry data into CAD modeling. This continuum modeling method does not randomly generate the position and distribution of nanoparticles to simulate the degree of clustering that is targeted, as in the existing multi-scale models [47,48]. This is a strong reason why mesoscale-based simulation is essential for nanocomposite design.

We first analyzed the mechanical properties depending on the silica content for a model composed of two phases: nanoparticles and polymer matrix. The DPD simulation results of unit cells with 3, 6, and 10 wt.% silica nanoparticles added to PU15 and the equivalent FEM models are shown as examples in Figure 4.11. 10-node tetrahedral elements were used in all finite element analyses, and each model had about 40,000-80,000 elements.

(a) PU15 + silica 3 wt.%



(b) PU15 + silica 6 wt.%



(c) PU15 + silica 10 wt.%

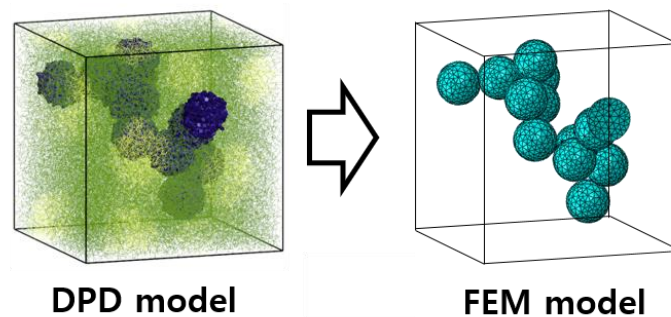


Figure 4.11 Configurations of DPD model of PU15/Silica nanocomposites and equivalent finite element model: (a) silica 3 wt.%, (b) silica 6 wt.%, and (c) silica 10 wt.%.

We derived the Young's modulus through the solution of a mathematical homogenization model integrating the microstructure of nanoparticles and a given matrix by using the following equation :

$$\mathbf{C}_H = \frac{1}{|V_y^c|} \int_{V_y^c} (\mathbf{C} - \mathbf{C} : \nabla_y \chi) dV_y \quad (4.5)$$

where \mathbf{C}_H represents the homogenized fourth-order elastic stiffness tensor of the nanocomposite, and $|V_y^c|$ is the volume of a homogenized microscopic unit cell. The χ tensor characterizes how the unit cell behaves under elastic conditions and can be calculated through numerical methods like finite element discretization. :

$$\int_{V_y^c} \nabla_y v(\mathbf{y}) : \mathbf{C} : \nabla_y \chi dV_y = \int_{V_y^c} \nabla_y v(\mathbf{y}) : \mathbf{C} dV_y \quad (4.6)$$

Here, v is the virtual displacement. We conducted computational homogenization analysis using our FEM code, incorporating periodic boundary conditions. For a deeper understanding of the mathematical formulas and finite element discretization, refer to our prior research [116]. To determine the elastic modulus of the nanocomposite, we applied a minor longitudinal strain of 0.3% to the FEM model. The mechanical properties of the polymer matrix, obtained through CG MD simulation (Figure 2.18), were then scaled up to the input data of the continuum FEM during this process. Hill's approach [117] was employed to characterize the effective elastic modulus of the nanocomposite unit cell, representing it as an isotropic elastic property in the context of polycrystalline structures.

Figures 4.12 show the change in Young's modulus and shear modulus according to silica content of PU15, PU32, and PU50, and the resulting values are listed in

Tables 4.6. The reinforcing effect on the elastic modulus of the SMPU nanocomposite increases with the silica content. The two-phase FE homonization results show that the tendency of property enhancement according to the weight percent of the nanofiller can be predicted without considering the interphase region.

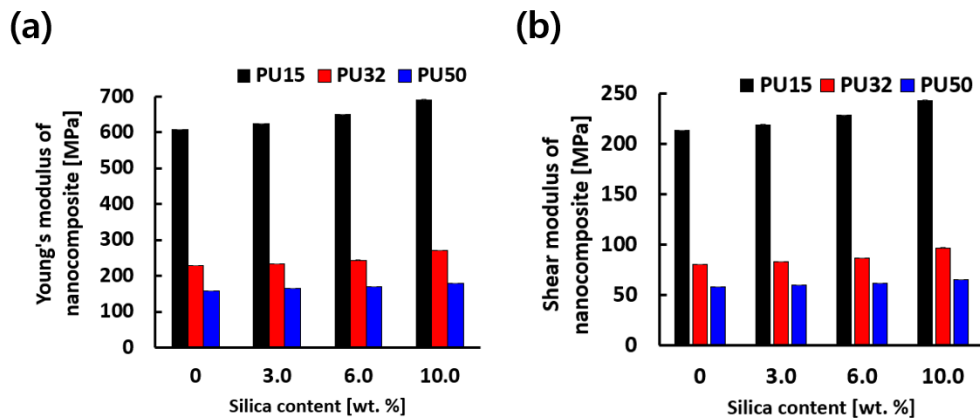


Figure 4.12 Homogenized (a) Young's modulus and (b) shear modulus of neat SMPU and nanocomposites with the silica contents without considering interphase.

Table 4.6 Young's modulus and shear modulus of SMPU/Silica nanocomposites with the Mori-Tanaka model (Unit: MPa).

Model		Silica content [wt. %]			
		0	3	6	10
PU15	Young's modulus	607.9	624.4	649.8	690.1
	Shear modulus	213.1	219.0	228.2	242.9
PU32	Young's modulus	228.0	234.1	243.6	270.6
	Shear modulus	80.8	83.0	86.5	96.6
PU50	Young's modulus	158.7	164.7	169.6	178.6
	Shear modulus	57.9	60.2	62.0	65.5

4.3.2 Development of interphase for nanoparticulate agglomeration effect

We derived the distribution change of nanoparticles according to the silica surface treatment in section 4.2. To accurately investigate the effect of the nanoparticle distributions in the same silica content on the mechanical properties, it is essential to introduce the concept of interphase region at the nanoscale. In order to develop an interphase model for three-phase homogenization, it is necessary to know the thickness and properties of the interphase region between the nanofiller and the polymer matrix.

To determine the mechanical properties of the interphase region, we utilized an inverse multiscale approach which combined a 3-phase micromechanics model with our CG MD simulation model. This approach involves comparing the characteristics of nanocomposites, which are derived from CG MD simulations, with the mathematical homogenization models or analytical solutions in micromechanics. These models are employed to predict the overall characteristics of composites by taking into account the attributes of individual phases.

The elastic modulus and shear modulus of the nanocomposites were obtained using the CG models shown in Figure 2.24 (a)-(c). To create the nanocomposite models, we added a single silica nanoparticle ($r=30$ angstroms) to the PU15, PU32, and PU50 matrix while keeping the nanofiller volume fraction constant at 0.06. We calculated the elastic modulus of the nanocomposites in the 1% strain range, which is the linear elastic region of the tensile stress-strain curve, and presented the corresponding values in Table 4.7.

Table 4.7 Young's modulus and shear modulus of neat SMPU and nanocomposites calculated from CG MD and Mori-Tanaka models.

MD Model	Young's modulus [MPa]	Shear modulus [MPa]
PU15	607.9	213.1
PU32	228.0	80.8
PU50	158.7	57.9
PU15 + Silica	826.5	291.1
PU32 + Silica	309.8	110.8
PU50 + Silica	200.3	73.9
PU15/Silica M-T	692.0	243.3
PU32/Silica M-T	262.1	93.3
PU50/Silica M-T	182.0	66.7

Table 4.7 shows the calculated young's modulus and shear modulus of each CG MD unit cells for SMPU and SMPU nanocomposites with conventional 2-phase Mori-Tanaka solution. The reinforcement effect of the nanofiller becomes evident as the mechanical properties of the nanocomposite models surpass those of the pure SMPU model. We compared the CG results with the values predicted by conventional two-phase Mori-Tanaka (M-T) micromechanics that do not consider interphase. It can be seen that the values calculated through our simulation is greater than the values of the Mori-tanaka solution. The difference between the two results can be attributed directly to the characteristics of the interphase region, and provides an insight that it is essential to consider the interphase effect to precisely predict the nanocomposites properties according to nanoparticle dispersion on a continuum scale.

We also defined the thickness of the interphase in each matrix through the radial density profile derived through CG MD. As seen in advance in Figure 2.25 in section 2.3, a high-density interphase region exists between the polymer matrix and nanoparticles, and the interphase thickness is defined as the point at which the radial density converges to the pure matrix density.

Given the known properties and volume fractions of composites, the features of the interphase region become implicit variables of interest. To address this, the multi-inclusion model, as outlined in references [118,119], offers a potential micromechanics approach for the reverse characterization of the interphase region. This continuum model takes into account the finite matrix effect by incorporating a fictitious infinite medium. The multi-inclusion model is comprised of three coaxial inclusions representing the matrix, particle, and interphase. These phases are considered to be isotropic and homogenous, and are embedded in an infinite medium, assuming a perfect bond with each other. The overall stiffness of the present three-phase nanocomposite (\mathbf{C}) can be solved using equation (4.7), and the interphase property (\mathbf{C}_i) can be calculated through the inverse process of equations (4.8)-(4.9). A detailed description of the micromechanics can be found in the Reference [118].

$$\mathbf{C} = \mathbf{C}_\infty [\mathbf{I} + (\mathbf{S} - \mathbf{I})(\sum_{r=1}^N f_r \Phi_r)] [\mathbf{I} + \mathbf{S}(\sum_{r=1}^N f_r \Phi_r)]^{-1} \quad (4.7)$$

$$\Phi_r = [(\mathbf{C}_\infty - \mathbf{C}_r)^{-1} \mathbf{C}_\infty - \mathbf{S}]^{-1} \quad (4.8)$$

$$\mathbf{C}_i = \mathbf{C}_\infty [\mathbf{I} - (\mathbf{f}_r \mathbf{B}^{-1} (\mathbf{C}_\infty^{-1} \mathbf{C} \mathbf{S} - \mathbf{S} + \mathbf{I}) + \mathbf{S})^{-1}]^{-1} \quad (4.9)$$

Table 4.8 Properties of interphase region for different HSCs of the SMPU.

Model	Interphase Property		
	Thickness [Å]	Young's modulus [MPa]	Shear modulus [MPa]
PU15 + Silica	20	1426.1	500.9
PU32 + Siliac	15	729.5	268.2
PU50 + Silica	10	500.8	188.7

The interphase properties (thickness and mechanical properties) derived through the corresponding processes are shown in Table 4.8. Finally, FE homogenization calculations were performed for 3-phase models with interphase regions as shown in Figure 4.13, and it was simplified by assuming that the characteristics of the interphase remained constant regardless of the surface treatment applied to silica.

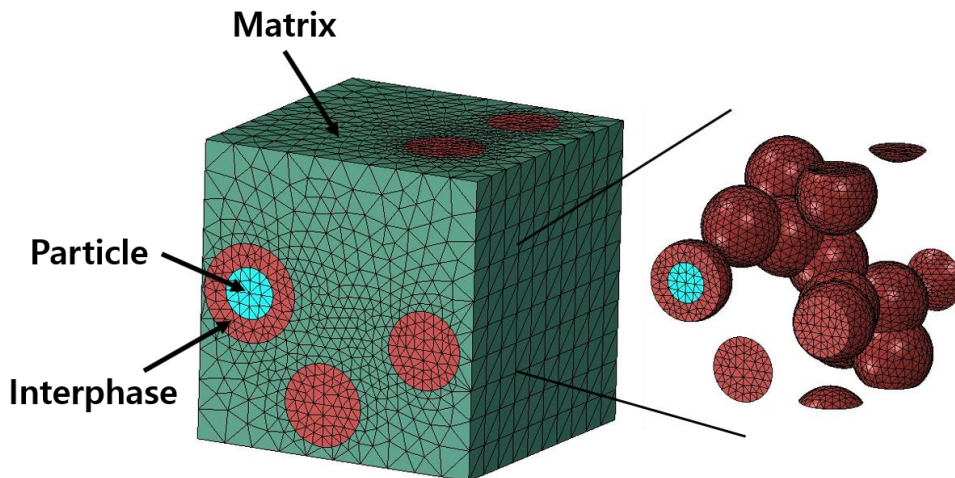
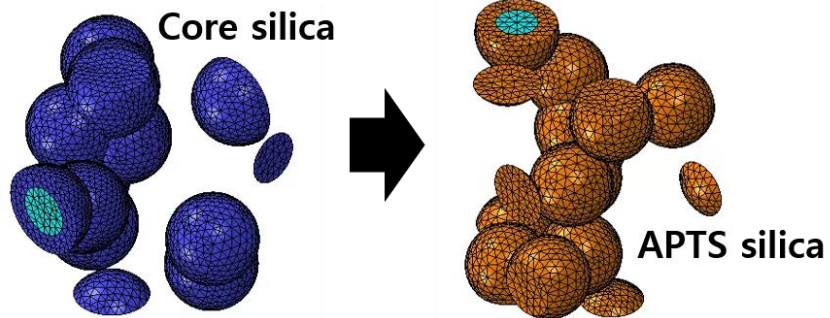


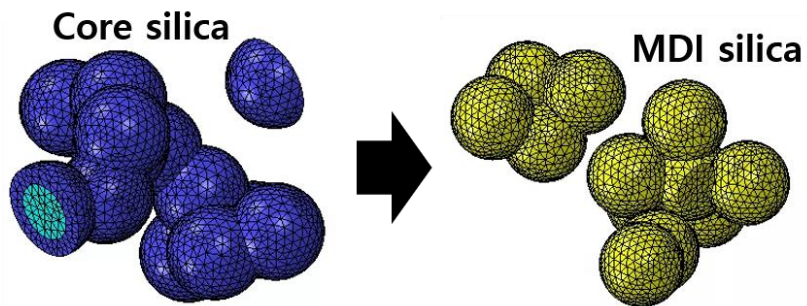
Figure 4.13 Equivalent finite element model for 3-phase (matrix, particle, and interphase) systems.

Figure 4.14 shows the change in particle distribution and interphase area according to the surface treatment of silica. As the compatibility between the nanoparticles and the matrix improves, the nanoparticles form an interphase with a wider area in a more dispersed form. Figure 4.15 shows the interphase volume fraction of the models and the resulting enhancement of mechanical properties. The reinforcing effect of 2-phase model (matrix and nanoparticle) was confirmed in section 4.3.1. Considering the interphase region between the polymer and the nanoparticles, which has stronger physical properties than the polymer matrix, the reinforcement effect of the nanocomposite can be more accurately predicted. Therefore, the homogenized Young's modulus of the nanocomposite considering the interfacial area showed a remarkable difference from the 2-phase model. In addition, as the distribution of nanoparticles was improved through the surface treatment of silica, the total volume ratio of the interphase region clearly increased, and the mechanical properties were further improved accordingly. These results show that the nanocomposite design we derive from mesoscale simulations can be used to predict realistic material properties. gradually increased.

(a) PU15



(b) PU32



(c) PU50

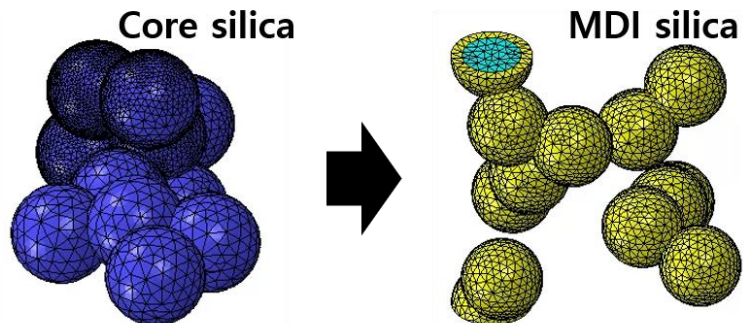
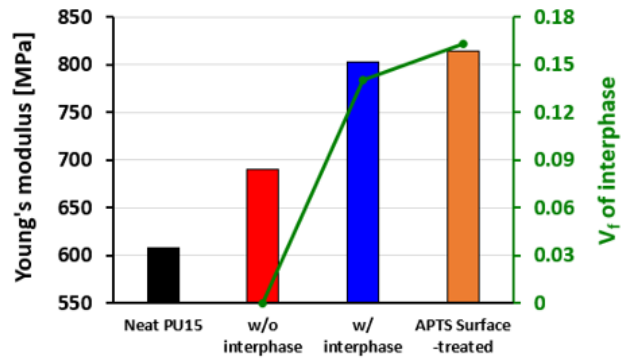
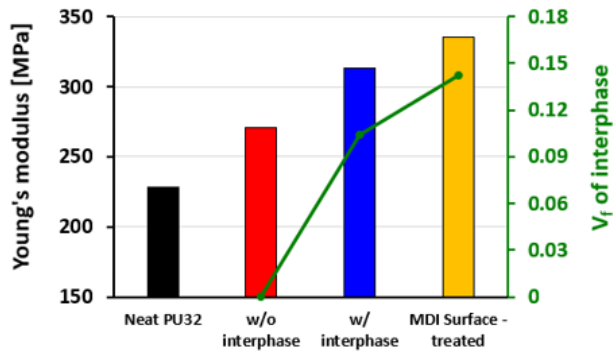


Figure 4.14 Changes of particle distribution and interphase area in 3-phase FEM model according to the surface treatment for (a) PU15, (b) PU32, and (c) PU50.

(a) PU15



(b) PU32



(c) PU50

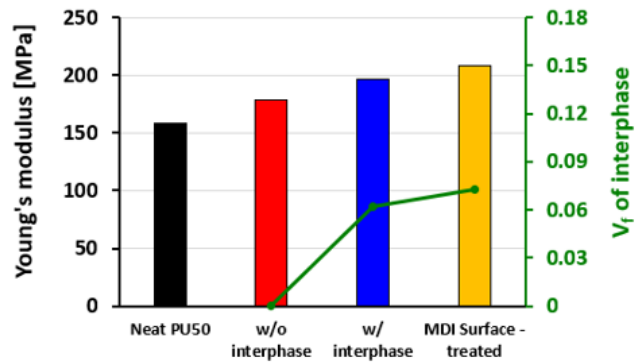


Figure 4.15 Homogenized Young's modulus of SMPU nanocomposites and volume fraction of interphase region considering interphase effect and silica surface treatment for (a) PU15, (b) PU32, and (c) PU50.

4.3.3 Reinforcement effect of anisotropic nanofiller

We confirmed the improving of the mechanical properties of SMPU nanocomposites through a 3-phase multiscale model that can reflect changes in the distribution of nanoparticles according to the silica surface treatment. The 3-phase nanocomposites unit cells showed a stronger elastic modulus by forming a more stable interphase region when the nanoparticles were uniformly distributed. Regardless of the degree of improvement in mechanical properties, these nanoparticulate models have isotropic characteristics, with the longitudinal modulus of the nanocomposites being almost similar in three axes due to the characteristics of spherical particles. Therefore, in this section, DPD simulation and FE homogenization were additionally performed on cylinder-shaped nanoparticles to investigate the reinforcement effect of the anisotropic nanofiller.

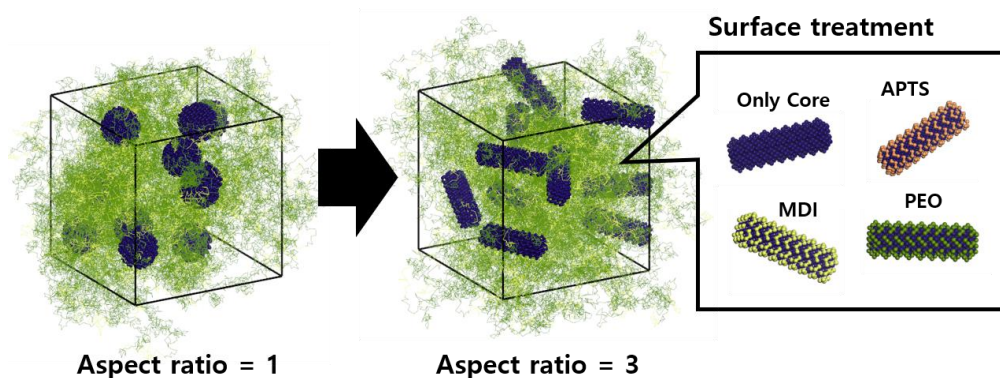


Figure 4.16 DPD modeling of silica surface treatment of cylindrical nanofiller.

As shown in Figure 4.16, we modeled a cylindrical nanofiller with an aspect ratio of 3. The cylinder has a diameter (D) of about 36.3 Å and a height ($h=3D$) of 109 Å, so that it has the same volume as the previous nanoparticle with a radius of 30 Å. As in section 4.2, various surface treatments were applied to the nanofiller, and DPD simulations were performed for models with a silica content of 10 wt.% for PU15, PU32, and PU50. The clustering density was calculated using equation (4.4), assuming an interphase region with a thickness of 6 Å between the cylindrical nanofiller and the matrix. Similarly, a normalization constant ($\Lambda=2.84$) was used to adjust the clustering density to 1 when 10 wt% of the silica nanoparticles were perfectly aggregated.

Figure 4.17 shows the clustering density results according to the HSC and silica surface treatment of the cylindrical nano-filler. The trend of the result is the same as that of the nanoparticle model in Figure 4.9. The degree of nanoparticle clustering of the untreated cylinders is a little higher than that of the nanoparticles. When the aspect ratio of the nano-fillers increases, the surface area increases and the nano-fillers become more aggregated. In the surface treatment results, as in the previous results, the APTS model for PU15 and the MDI model for PU32 and PU50 showed the most optimal nanoparticle distribution. Figure 4.18 shows the DPD configurations showing the optimal nanofiller distribution change in PU15 and PU50. In the Core model of PU15, nanofillers are agglomerated to form some clusters, whereas in the model with improved compatibility with the soft segment through APTS surface treatment, they are evenly distributed over a relatively wide area of

the matrix. In PU50, the ratio of the hard phase is increased so that the nanofillers are strongly aggregated in the center like one large spherical cluster. On the other hand, in the model with MDI-surface treatment, it can be confirmed that the nanofiller is evenly distributed in the continuous hard segment domain, and the clustering density is significantly improved.

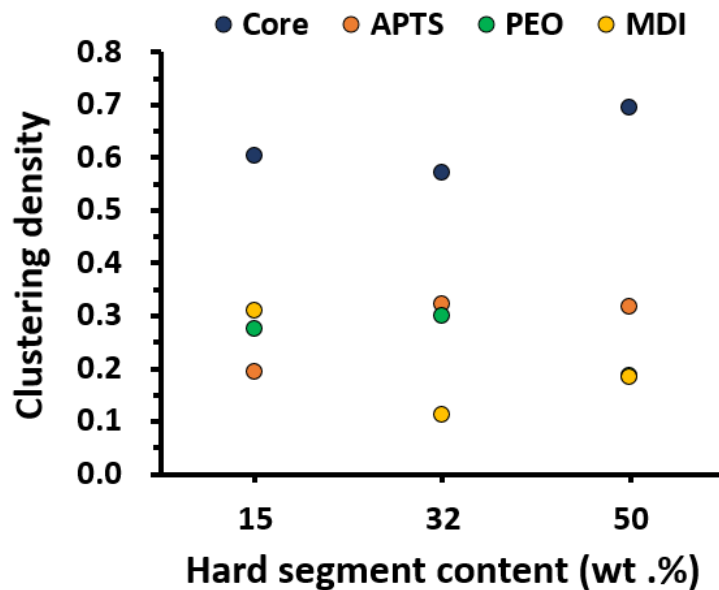


Figure 4.17 Clustering density change of cylindrical nanofiller.

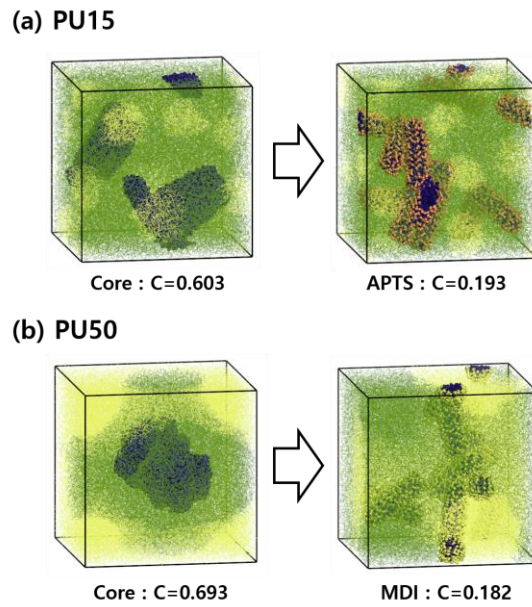


Figure 4.18 Cylinder distribution improvement by optimal surface treatment in (a) PU15 and (b) PU50.

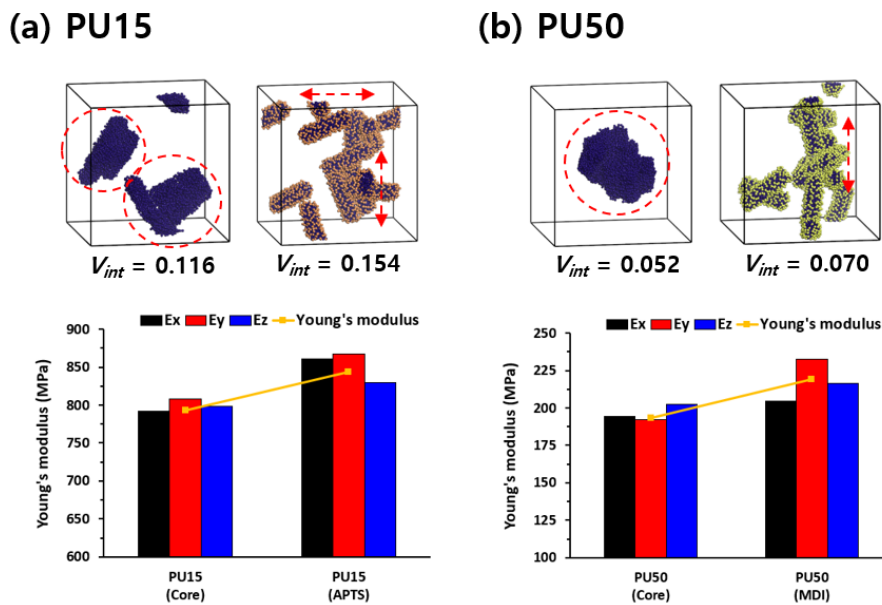


Figure 4.19 Distributions of cylindrical nanofillers, and corresponding volume fraction of interphase (V_{int}) and mechanical properties for (a) PU15 and (b) PU50.

The homogenized Young's modulus was calculated to derive the mechanical properties reflecting the the distribution of the cylindrical nanofiller obtained through DPD simulation. Here, as well, the interphase characteristics of the nanofiller should be considered. In this study, it was modeled assuming that a single cylinder has an interphase region of the same volume as a single particle in each HSC.

Figure 4.19 shows the nanofiller distribution of each model, the interphase volume fraction in that distribution, and the derived mechanical properties. Here, as the mechanical properties, not only young's modulus, which is an effective isotropic property, but also elastic stiffness in each axial direction, E_x , E_y , and E_z , are also shown. As a uniform distribution was obtained through the surface treatment of silica, the volume fraction of the high-density interfacial area increased, and the young's modulus of the nanocomposite is also significantly improved. An additional point to be noted in the strengthening effect of the cylindrical nanofiller is the anisotropy of the nanocomposite. Since the cylinder-shaped nanofiller has an aspect ratio of 3, the orientation of the longitudinal axis exists, but when the nanofillers are agglomerated, the anisotropic properties do not significantly exist because the cylinders form new clusters. However, when the nanofillers have a well-dispersed distribution, it is advantageous to have an arrangement leading in a specific direction, which can maximize the enhancement of mechanical properties in that direction. Therefore, the deviation of elastic stiffness in each direction of the untreated nanofiller model was 3~6% compared to the properties of the neat matrix, whereas

the deviation was 6~17% in the surface treated model.

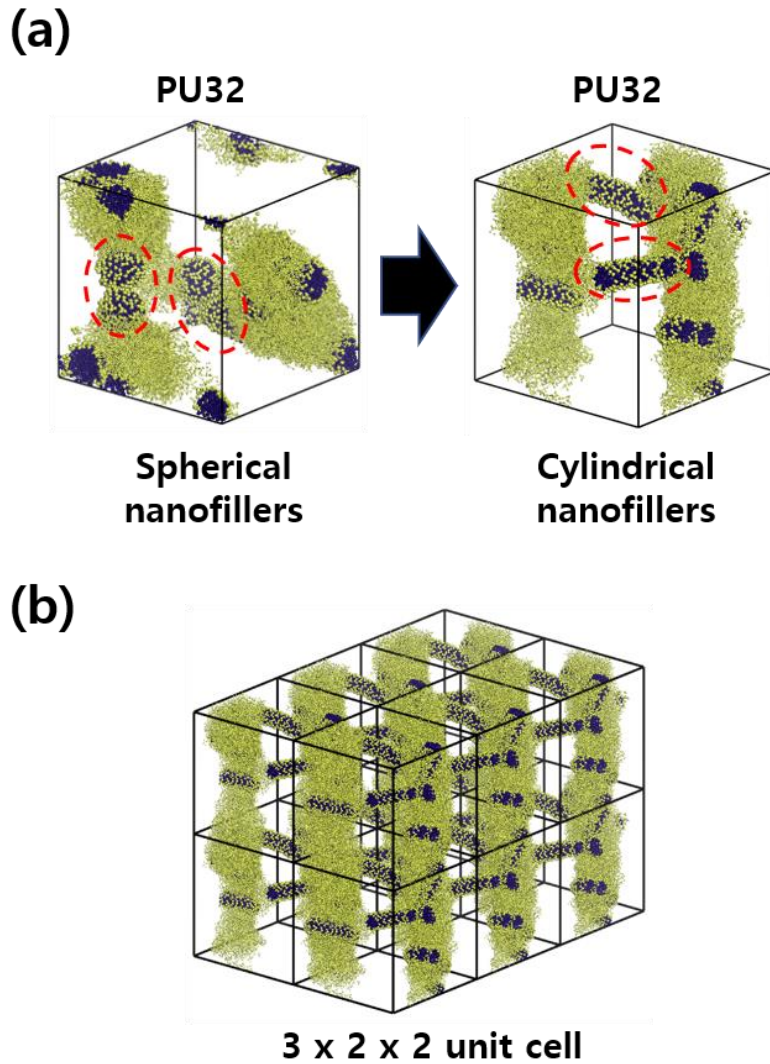


Figure 4.20 (a) Bridging architectural morphology of cylindrical nanofillers in lamellar structure, and (b) $3 \times 2 \times 2$ periodic unit cells.

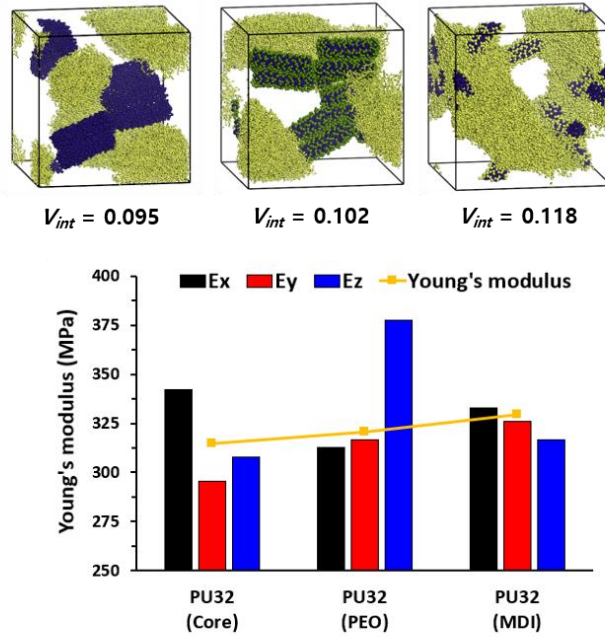
The difference in characteristics between spherical nanoparticles and cylindrical nanoparticles is most prominent in the PU32 matrix. First, looking again at the clustering density in Figures 4.9 and 4.17, in PU15 and PU50, where either soft-segment or hard-segment dominates in spherical nanoparticles, the distribution improvement effect was better, whereas in cylindrical nanofiller, PU32 showed the most uniform distribution. This is related to the phase separated morphology of the PU32 matrix, that is, the hard domain of PU32 takes the form of alternating lamellae like a thin strip. Figure 4.20(a) compares nanoparticle models treated with MDI on PU32. The surface treatment model is characterized by connecting adjacent hard domains due to strong attraction between MDI beads. However, in the case of a long nanofiller with an aspect ratio of 3, it can be seen that a single free nanofiller can connect alternating lamellar hard domains like a "bridge". As such, the nano-filler distribution of PU32 is further enhanced due to the free nano-filler effect, which exists as the lamellar hard domains strongly hold the ends of the cylinder. Figure 4.20(b) shows the microstructure through $3 \times 2 \times 2$ periodic unit cells of the model.

We also calculated the homogenized mechanical properties for three different models (Core, PEO, and MDI surface-treated) of PU32/silica nanocomposites as shown in Figure 4.21(a). As in PU15 and PU50, the volume fraction and Young's modulus of the interphase region increase as the clustering density decreases. However, the anisotropy of the nanocomposite of PU32 is greatest in the well-aligned models along the lamellar wave direction of the soft domain, regardless of the degree of dispersion of the nanofiller. As confirmed in Figure 4.20(a), the MDI-

cylinder has a complex distribution along the hard domain, and the basic core model has relatively strong agglomeration characteristics even though nanofillers exist in the soft segment region. The PEO-surface treated nanofillers showed the greatest anisotropy because they were well dispersed along the wave line of the lamellar soft matrix with improved compatibility as shown in Figure 4.21(b). Therefore, the elastic stiffness variation in each direction increased by 28% in PEO-cylinders in PU32.

Trough this section, we confirmed the surface treatment method for improving the nanoparticle distribution and mechanical properties in SMPU/silica nanocomposites, as well as the aspect ratio effect of nanofiller. Through this, it was examined that in the design of nanocomposites where phase separation occurs, such as SMPU copolymer, not only the compatibility between the nanofiller and each segment of the polymer matrix, but also the phase-separated morphology of the polymer matrix itself should be considered.

(a)



(b)

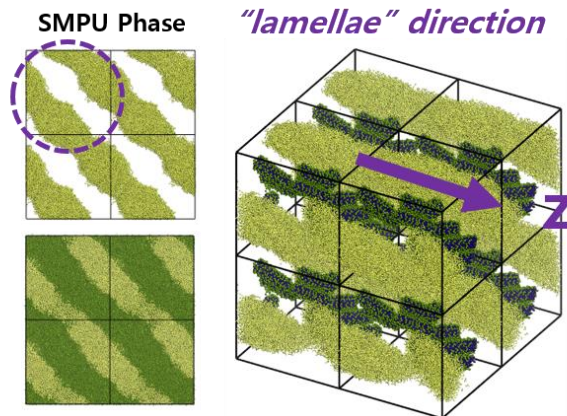


Figure 4.21 (a) Distributions of cylindrical nanofillers, and corresponding volume fraction of interphase (V_{int}) and mechanical properties for PU32 nanocomposites, and (b) Anisotropy of nanocomposites.

Conclusions

This study employed a mesoscale simulation-based multiscale analysis to investigate the thermo-mechanical behavior and phase separation of semi-crystalline SMPU/silica nanocomposites with different HSC. While conventional AA MD simulation accurately reproduces material structures, it is computationally demanding and limits the exploration of global macromolecular movements, such as crystalline phase formation and aggregation of linear copolymer system's hard domains. To overcome these limitations, we utilized a CG bead system to reduce the degrees of freedom, enabling extended simulation timescales and length scales.

Furthermore, a dissipative particle dynamics simulation model was developed to examine phase separation and nanoparticle distribution in polyurethane nanocomposites. By incorporating molecular-level solubility calculations as simulation parameters, the model accurately predicted polymer phase shapes and actual nanoparticle distributions based on segment ratios. Additionally, surface treatments were applied to silica nanoparticles to optimize their distribution.

Finally, a continuum model was created based on the geometry obtained from the phase separation simulation of the polyurethane nanocomposite. To predict mechanical properties based on nanoparticle dispersion, a finite element-based homogenization technique was introduced. This paper presents a design methodology for various nanocomposites and anticipates that this mesoscale simulation-based multiscale analysis will drive further research for practical

nanocomposite design and targeted property attainment. The dependence of thermo-mechanical properties on HSC in SMPU copolymers facilitates the identification of a continuum mechanics constitutive relation, enabling molecular-level simulation of large deformations. Therefore, this study provides valuable insights into the microstructure-dependent behavior of shape-memory polymer nanocomposites and aids in the custom design of advanced stimuli-responsive materials.

Bibliography

- [1] J. Leng, X. Lan, Y. Liu, S. Du, Shape-memory polymers and their composites: stimulus methods and applications. *Prog. Mater. Sci.*, 2001, 56, 1077–1135.
- [2] Q. Song, H. Chen, S. Zhou, K. Zhao, B. Wang, P. Hu, Thermo- and pH- sensitive shape memory polyurethane containing carboxyl groups. *Polym. Chem.*, 2016, 7, 1739-1746.
- [3] J. Hu, Y. Zhu, H. Huang, J. Lu, Recent advances in shape-memory polymers: structure, mechanism, functionality, modeling and applications. *Prog. Polym.*, 2012, 37, 1720–1763.
- [4] A. Lendlein, R. Langer, Biodegradable, Elastic Shape-Memory Polymers for Potential Biomedical Applications. *Science*, 2002, 296, 1673-1676.
- [5] D. J. Maitland, M. F. Metzger, D. Schumann, A. Lee, T. S. Wilson, Photothermal properties of shape memory polymer micro-actuators for treating stroke. *Lasers Surg. Med.*, 2002, 30, 1–11.
- [6] H. Meng, G. Li, A review of stimuli-responsive shape memory polymer composites. *Polymer*, 2013, 54, 2199–2221.
- [7] F. Li, X. Zhang, J. Hou, M. Xu, X. Luo, B. Kim, Studies on thermally stimulated shape memory effect of segmented polyurethanes. *J. Appl. Polym. Sci.*, 1997, 64, 1511–1516.
- [8] B. Kim, S. Lee, M. Xu, Polyurethanes having shape memory effects. *Polymer*, 1996, 26, 5781–5793.
- [9] M. F. Sonnenschein, Z. Lysenko, D. A. Brune, B. L. Wendt, A. K. Schrock,

- Enhancing polyurethane properties via soft segment crystallization. *Polymer*, 2005, 46, 10158–10166.
- [10] S. Thakur, J. Hu, Polyurethane: a shape memory polymer (SMP). Intechopen. 2017, 69992. uch as d Mater
- [11] T. Takahasahi, N. Hayashi, S. Hayashi, Structure and properties of shape-memory polyurethane block copolymers. *J. Appl. Polym. Sci.*, 1996, 60, 1061–1996.
- [12] J. Lin, K. Chen, Study on shape-memory behavior of polyether-based polyurethanes. I. Influence of the hard-segment content. *J. Appl. Polym. Sci.*, 2), pp. 5115-51261998, 69, 1563–1574.
- [13] F. Li, J. Hou, W. Zhu, X. Zhang, M. Xu, X. Luo, D. Ma, B. Kim, Crystallinity and morphology of segmented polyurethanes with different soft-segment length. *J. Appl. Polym. Sci.*, 1998, 62, 631–638.
- [14] B. Dittrich, K. A. Wartig, R. Mülhaupt, B. Schartel, Flame-retardancy properties of intumescent ammonium poly (phosphate) and mineral filler magnesium hydroxide in combination with graphene. *Polymers*, 2014, 6(11), 2875-2895.
- [15] W. Sokolowski, A. Metcalfe, S. Hayashi, J. Raymond, Medical applications of shape memory polymers. *Biomedical Materials*, 2007, 2(1), S23.
- [16] K. Gall, M.L. Dunn, Y. Liu, D. Finch, M. Lake, N.A. Munshi, Shape memory polymer nanocomposites. *Acta Materialia*, 2002, 50(20), 5115-5126.
- [17] K. Gall, M. Mikulas, N. A. Munshi, F. Beavers, M. Tupper, Carbon fiber reinforced shape memory polymer composites. *Journal of intelligent material*

- systems and structures*, 2000, 11(11), 877-886.
- [18] A. Lendlein, A. M. Schmidt, R. Langer, AB-polymer networks based on oligo (ϵ -caprolactone) segments showing shape-memory properties. *Proceedings of the National Academy of Sciences*, 2001, 98(3), 842-847.
- [19] Z. G. Wei, R. Sandström, S. Miyazaki, Shape-memory materials and hybrid composites for smart systems: Part I Shape-memory materials. *Journal of materials science*, 1998, 33, 3743-3762.
- [20] M. A. Fonseca, B. Abreu, F. A. M. M. Gonçalves, A. G. M. Ferreira, R. A. S. Moreira, M. S. A. Oliveira, Shape memory polyurethanes reinforced with carbon nanotubes. *Composite Structures*, 2013, 99, 105-111.
- [21] F. Li, L. Qi, J. Yang, M. Xu, X. Luo, D. Ma, Polyurethane/conducting carbon black composites: structure, electric conductivity, strain recovery behavior, and their relationships. *Journal of Applied Polymer Science*, 2000, 75(1), 68-77.
- [22] B. Yang, W. M. Huang, C. Li, J. H. Chor, Effects of moisture on the glass transition temperature of polyurethane shape memory polymer filled with nano-carbon powder. *European Polymer Journal*, 2005, 41(5), 1123-1128.
- [23] K. Gall, M. L. Dunn, Y. Liu, G. Stefanic, D. Balzar, Internal stress storage in shape memory polymer nanocomposites. *Applied Physics Letters*, 2004, 85(2), 290-292.
- [24] S. Mondal, H. J. LIAN, Shape memory studies of functionalized MWNT-reinforced polyurethane copolymers. 2006, 135-142.
- [25] H. Koerner, G. Price, N. A. Pearce, M. Alexander, R. A. Vaia, Remotely actuated

- polymer nanocomposites—stress-recovery of carbon-nanotube-filled thermoplastic elastomers. *Nature materials*, 2004, 3(2), 115-120.
- [26] A. Koyama, T. Yamamoto, K. Fukao, Y. Miyamoto, Molecular dynamics studies on local ordering in amorphous polyethylene. *J. Chem. Phys.*, 2001, 115, 560–566.
- [27] A. Koyama, T. Yamamoto, K. Fukao, Y. Miyamoto, Molecular dynamics simulation of polymer crystallization from an oriented amorphous state. *Phys. Rev. E.*, 2002, 65, 050801.
- [28] T. Yamamoto, Molecular dynamics simulation of polymer crystallization through chain folding. *J. Chem. Phys.*, 1997, 107, 2653–2663.
- [29] T. Yamamoto, Molecular dynamics simulation of polymer ordering. II. Crystallization from the melt. *J. Chem. Phys.*, 2001, 115, 8675–8680.
- [30] M. S. Uddin, J. Ju, Enhanced coarse-graining of thermoplastic polyurethane elastomer for multiscale modeling. *J. Eng. Mater. Technol.*, 2017, 139, 011001.
- [31] J. Hu, C. Zhang, X. Li, J. Han, F. Ji, Architectural evolution of phase domains in shape memory polyurethanes by dissipative particle dynamics simulations. *Polym. Chem.*, 2017, 8, 260–271.
- [32] B. C. Abberton, W. K. Liu, S. Keten, Coarse-grained simulation of molecular mechanisms of recovery in thermally activated shape-memory polymers. *J. Mech. Phys. Solids*, 2013, 61, 2625–2637.
- [33] Z. Cui, C. Brinson, Thermomechanical properties and deformation of coarse-grained models of hard-soft block copolymers. *Phys. Rev. E*, 2013, 88, 022602.

- [34] J. Hu, C. Zhang, F. Ji, X. Li, J. Han, Y. Wu, Revealing the morphological architecture of a shape memory polyurethane by simulation. *Sci. Rep.*, 2016, 6, 29180.
- [35] L. Vaisman, H.D. Wagner, The role of surfactants in dispersion of carbon nanotubes. *Adv. Colloid Interface Sci.*, 2006, 128, pp. 37-46
- [36] T. Glaskova, M. Zarrelli, A. Borisova, K. Timchenko, A. Aniskevich, M. Giordano, Method of quantitative analysis of filler dispersion in composite systems with spherical inclusions. *Compos. Sci. Technol.*, 2011, 71, pp. 1543-1549
- [37] J. Liu, Y. Gao, D. Cao, L. Zhang, Z. Guo, Nanoparticle dispersion and aggregation in polymer nanocomposites: insights from molecular dynamics simulation. *Langmuir*, 2011, 27, pp. 7926-7933
- [38] D. Weidt, L. Figiel, Effect of CNT waviness and Van der Waals interaction on the nonlinear compressive behavior of epoxy/CNT nanocomposites. *Compos. Sci. Technol.*, 2015, 115, pp. 52-59.
- [39] J. Jancar, J.F. Douglas, F.W. Starr, S.K. Kumar, P. Cassagnau, A.J. Lesser, Current issues in research on structure–property relationships in polymer nanocomposites. *Polymer*, 2010, 51 (15), pp. 3321-3343
- [40] L. Vaisman, H.D. Wagner, G. Marom, The role of surfactants in dispersion of carbon nanotu. *Adv. Colloid Interface*, 2006, 128, 37.
- [41] C. Lu, J.M.P. Almeida, N. Yao, C. Arnold, Fabrication of uniformly dispersed nanoparticle-doped chalcogenide glass. *Appl. Phys. Lett.* 2014, 105, 261906.

- [42] J. Liu, Y. Gao, D. Cao, L. Zhang, Z. Guo, Nanoparticle dispersion and aggregation in polymer nanocomposites: insights from molecular dynamics simulation. *Langmuir*, 2011, 27, 7926.
- [43] L.M. Hall, A. Jayaraman, K.S. Schweizer, Molecular theories of polymer nanocomposites. *Curr. Opin. Solid State Mater. Sci.* 14 (2010) 38.
- [44] A. Pontefisso, M. Zappalorto, M. Quaresimin, An efficient RVE formulation for the analysis of the elastic properties of spherical nanoparticle reinforced polymers. *Comput. Mater. Sci.*, 2015, 96, 319.
- [45] S. Yang, S. Yu, M. Cho, Sequential thermoelastic multiscale analysis of nanoparticulate composites. *Journal of Applied Physics*, 2010, 056102.
- [46] M. Cho, S. Yang, S. Chang, S. Yu, A study on the prediction of the mechanical properties of nanoparticulate composites using the homogenization method with the effective interface concept. *International journal for numerical methods in engineering*, 2011, 85(12), 1564-1583.
- [47] K. Baek, K., H. Shin, H., T. Yoo, M. Cho, Two-step multiscale homogenization for mechanical behaviour of polymeric nanocomposites with nanoparticulate agglomerations. *Composites Science and Technology*, 2019, 179, 97-105.
- [48] K. Baek, H. Shin, M.Cho, Multiscale modeling of mechanical behaviors of Nano-SiC/epoxy nanocomposites with modified interphase model: Effect of nanoparticle clustering. *Composites Science and Technology*, 2021, 203, 108572.
- [49] V. Agrawal, G. Arya, J. Oswald, Simultaneous iterative Boltzmann inversion for coarse-graining of polyurea. *Macromolecules*, 2014, 47, 3378–3389.

- [50] J. Zhang, J. Su, Y. Ma, H. Guo, Coarse-grained molecular dynamics simulations of the phase behavior of the 4-cyano-4'-pentylbiphenyl liquid crystal system. *J. Phys. Chem. B*, 2012, 116, 2075–2089.
- [51] J. Moon, B. Kim, M. Cho, Multiscale study of relationship between photoisomerization and mechanical behavior of azo-polymer based on the coarse-grained molecular dynamics simulation. *Macromolecules*, 2019, 52, 2033–2049.
- [52] G. Milano, S. Goudeau, F. Müller-Plathe, Multicentered Gaussian-based potentials for coarse-grained polymer simulations: linking atomistic and mesoscopic scales. *J. Polym. Sci. Part B: Polym. Phys.*, 2005, 43, 871–885.
- [53] D. Reith, M. Pütz, F. Müller-Plathe, Deriving effective mesoscale potentials from atomistic simulations. *J. Comput. Chem.*, 2003, 24, 1624–1636.
- [54] D. Theodorou, U. Suter, Detailed molecular structure of a vinyl polymer glass. *Macromolecules*, 1985, 18, 1467–1478.
- [55] S. Plimpton, P. Crozier, A. Thompson, LAMMPS-large-scale atomistic/molecular massively parallel simulator. Sandia National Laboratories, 2007, 18, 43.
- [56] H. Sun, Force field for computation of conformational energies, structures, and vibrational frequencies of aromatic polyesters. *J. Comput. Chem.*, 1994, 15, 752–768.
- [57] A. Ghanbari, T. V. Nodoro, F. Leroy, M. Rahimi, M. C. Böhm, F. Müller-Plathe, F. Interphase structure in silica–polystyrene nanocomposites: a coarse-grained

- molecular dynamics study. *Macromolecules*, 2012, 45(1), 572-584.
- [58] T. Schneider, E. Stoll, Molecular-dynamics study of a three-dimensional one-component model for distortive phase transitions. *Phys. Rev. B*, 1978, 17, 1302.
- [59] H. J. Berendsen, J. v. Postma, W. F. van Gunsteren, A. DiNola, J. Haak, Molecular dynamics with coupling to an external bath. *J. Chem. Phys.*, 1984, 81, 3684-3690.
- [60] S. Deng, Tensile deformation of semi-crystalline polymers by molecular dynamics simulation. *Iran. Polym. J.*, 2017, 26, 903-911.
- [61] F. L. Ji, J. L. Hu, T. C. Li, Y. W. Wong, Morphology and shape memory effect of segmented polyurethanes. Part I: with crystalline reversible phase. *Polymer*, 2007, 47, 5133-5145.
- [62] M. S. Sánchez-Adsuar, Influence of the composition on the crystallinity and adhesion properties of thermoplastic polyurethane elastomers. *Int. J. Adhes. Adhes.*, 2000, 20, 291-298.
- [63] S. S. Liow, V. T. Lipik, L. K. Widjaja, S. S. Venkatraman, M. J. M. Abadie, Enhancing mechanical properties of thermoplastic polyurethane elastomer with 1,3-trimethylene carbonate, epsilon-caprolactone and L-lactide copolymers via soft segment crystallization. *Express Polym. Lett.*, 2011, 5, 897-910.
- [64] K. Kojio, M. Furukawa, Y. Nonaka, S. Nakamura, Control of mechanical properties of thermoplastic polyurethane elastomer by restriction of crystallization of soft segment. *Materials*, 2010, 3, 5097-5110.
- [65] A. Eceiza, M. D. Martin, K. de la Carba, G. Kortaberria, N. Gabilondo, M. A.

- Corcuera, I. Mondragon, Thermoplastic polyurethane elastomer based on polycarbonate diols with different soft segment molecular weight and chemical structure: mechanical and thermal properties. *Polym. Eng. Sci.*, 2008, 48, 297–306.
- [66] R. S. Waletzko, L. T. J. Korley, B. D. Pate, E. L. Thomas, P. T. Hammond, Role of increased crystallinity in deformation-induced structure of segmented thermoplastic polyurethane elastomers with PEO and PEO-PPO-PEO soft segment and HDI hard segments. *Macromolecules*, 2009, 42, 2041–2053.
- [67] M. F. Sonnenschein, Z. Lysenko, D. A. Brune, B. L. Wendt, A. K. Schrock, Enhancing polyurethane properties via soft segment crystallization. *Polymer* 2005, 46, 10158–10166.
- [68] I. A. Rousseau, T. Xie, Shape memory epoxy: composition, structure, properties and shape memory performances. *J. Mater. Chem.*, 2010, 20, 3431–3441.
- [69] S. Yu, S. Yang, M. Cho, Multi-scale modeling of cross-linked epoxy nanocomposites, *Polymer*, 50 (2009), pp. 945-952
- [70] H. Shin, S. Yang, J. Choi, S. Chang, M. Cho, Effect of interphase percolation on mechanical behavior of nanoparticle-reinforced polymer nanocomposite with filler agglomeration: a multiscale approach, *Chem Phys Lett*, 635 (2015), pp. 80-85
- [71] J. Choi, H. Shin, M. Cho, A multiscale mechanical model for the effective interphase of SWNT/Epoxy nanocomposite, *Polymer*, 89 (2016), pp. 159-171
- [72] J. Kratochvíl, I. Kelnar, Non-isothermal kinetics of cold crystallization in

- multicomponent PLA/thermoplastic polyurethane/nanofiller system. *Journal of Thermal Analysis and Calorimetry*, 2017, 130, 1043-1052.
- [73] I. S. Gunes, F. Cao, S. C. Jana, Evaluation of nanoparticulate fillers for development of shape memory polyurethane nanocomposites. *Polymer*, 2008, 49(9), 2223-2234.
- [74] S. L. Blagojević, Z. Buhin, I. Igrec, Influence of silica nanofiller on the isothermal crystallization and melting of polyurethane elastomer. *Journal of Applied Polymer Science*, 2013, 129(3), 1466-1475.
- [75] Y. Niyom, T. Phakkeeree, A. Flood, D. Crespy, Synergy between polymer crystallinity and nanoparticles size for payloads release. *Journal of colloid and interface science*, 2019, 550, 139-146.
- [76] L. Xu, Y. Fu, M. Du, Investigation on structures and properties of shape memory polyurethane/silica nanocomposites. *Chinese Journal of Chemistry*, 2011, 29(4), 703-710.
- [77] H. Oh, P. F. Green, Polymer chain dynamics and glass transition in athermal polymer/nanoparticle mixtures. *Nature materials*, 2009, 8(2), 139-143.
- [78] A. Kamyab, A. Ghasemi-Ghalebahman, A. Fereidoon, H. A. Khonakdar, Shape memory and mechanical properties of polycaprolactone/polypropylene carbonate nanocomposite blends in the presence of G-POSS nanoparticles. *Express Polymer Letters*, 2021, 15(5), 473-489.
- [79] L. Bistričić, G. Baranović, M. Leskovac, M., E. G. Bajsić, Hydrogen bonding and mechanical properties of thin films of polyether-based polyurethane–silica

- nanocomposites. *European Polymer Journal*, 2010, 46(10), 1975-1987.
- [80] R. D. Groot, P. B. Warren, Dissipative particle dynamics: Bridging the gap between atomistic and mesoscopic simulation. *The Journal of chemical physics*, 1997, 107(11), 4423-4435.
- [81] P. Espanol, P. Warren, Statistical mechanics of dissipative particle dynamics. *Europhysics letters*, 1995, 30(4), 191.
- [82] H. Sun, COMPASS: an ab initio force-field optimized for condensed-phase applications overview with details on alkane and benzene compounds. *The Journal of Physical Chemistry B*, 1998, 102(38), 7338-7364.
- [83] S. Sami, E. Yildirim, M. Yurtsever, E. Yurtsever, E. Yilgor, I. Yilgor, G. L. Wilkes, Understanding the influence of hydrogen bonding and diisocyanate symmetry on the morphology and properties of segmented polyurethanes and polyureas: Computational and experimental study. *Polymer*, 2014, 55(18), 4563-4576.
- [84] C. Danda, L. G. Amurin, P. A. Munoz, D. A. Nagaoka, T. Schneider, B. Troxell, ... J. M. Maia, Integrated computational and experimental design of ductile, abrasion-resistant thermoplastic polyurethane/graphene oxide nanocomposites. *ACS Applied Nano Materials*, 2020, 3(10), 9694-9705.
- [85] Y. R. Sliozberg, J. L. Gair Jr, A. J. Hsieh, Dissipative particle dynamics simulation of microphase separation in polyurethane urea nanocomposites. *Polymer*, 2020, 193, 122339.
- [86] W. Y. Song, H. Lu, J. W. He, Z. J. Zhu, S. Y. He, D. H. Liu, ... Y. Wang,

- Dynamics and morphology of self-assembly behavior of polymer-grafted nanoparticles: a dissipative particle dynamics simulation study. *Polymer International*, 2022, 71(11), 1330-1339.
- [87] J. Mai, D. Sun, L. Li, J. Zhou, Phase behavior of an amphiphilic block copolymer in ionic liquid: A dissipative particle dynamics study. *Journal of Chemical & Engineering Data*, 2016, 61(12), 3998-4005.
- [88] M. Kim, J. Moon, S. Park, M. Cho, Selective dissolution resistance control of EUV photoresist using multiscale simulation: rational design of hybrid system. *Macromolecules*, 2020, 53(12), 4748-4763.
- [89] H. Bhanushali, S. Amrutkar, S. Mestry, S. T. Mhaske, Shape memory polymer nanocomposite: a review on structure–property relationship. *Polymer Bulletin*, 2022, 79(6), 3437-3493.
- [90] J. Hu, C. Zhang, X. Li, J. Han, F. Ji, Architectural evolution of phase domains in shape memory polyurethanes by dissipative particle dynamics simulations. *Polymer Chemistry*, 2017, 8(1), 260-271.
- [91] J. Hu, C. Zhang, F. Ji, X. Li, J. Han, Y. Wu, Revealing the morphological architecture of a shape memory polyurethane by simulation. *Scientific Reports*, 2016, 6(1), 1-9.
- [92] A. Saralegi, L. Rueda, B. Fernández-d'Arlas, I. Mondragon, A. Eceiza, M. A. Corcuera, Thermoplastic polyurethanes from renewable resources: effect of soft segment chemical structure and molecular weight on morphology and final properties. *Polymer International*, 2013, 62(1), 106-115.

- [93] C. H. Y. Chen-Tsai, E. L. Thomas, W. J. MacKnight, N. S. Schneider, Structure and morphology of segmented polyurethanes: 3. Electron microscopy and small angle X-ray scattering studies of amorphous random segmented polyurethanes. *Polymer*, 1986, 27(5), 659-666.
- [94] C. E. Wilkes, C. S. Yusek, Investigation of domain structure in urethan elastomers by X-ray and thermal methods. *Journal of Macromolecular Science, Part B: Physics*, 1973, 7(1), 157-175.
- [95] K. Park, W. H. Lim, E. A. Ko, H. S. Lee, Effect of molecular shape of diisocyanate units on the microscopic/macrosopic phase separation structure of polyurethanes. *Journal of Polymer Science Part B: Polymer Physics*, 2011, 49(12), 890-897.
- [96] A. A. Gavrilov, Y. V. Kudryavtsev, A. V. Chertovich, Phase diagrams of block copolymer melts by dissipative particle dynamics simulations. *The Journal of chemical physics*, 2013, 139(22), 224901.
- [97] C. Li, S. L. Goodman, R. M. Albrecht, S. L. Cooper, Morphology of segmented polybutadiene-polyurethane elastomers. *Macromolecules*, 1988, 21(8), 2367-2375.
- [98] Koberstein, J. T., Galambos, A. F., & Leung, L. M. (1992). Compression-molded polyurethane block copolymers. 1. Microdomain morphology and thermomechanical properties. *Macromolecules*, 25(23), 6195-6204.
- [99] S. B. Lin, K. S. Hwang, S. Y. Tsay, S. L. Cooper, Segmental orientation studies of polyether polyurethane block copolymers with different hard segment lengths

- and distributions. *Colloid and Polymer Science*, 1985, 263, 128-140.
- [100] F. L. Ji, J. L. Hu, T. C. Li, Y. W. Wong, Morphology and shape memory effect of segmented polyurethanes. Part I: With crystalline reversible phase. *Polymer*, 2007, 48(17), 5133-5145.
- [101] Xie, X., Xu, S., Pi, P., Cheng, J., Wen, X., Liu, X., & Wang, S. (2018). Dissipative particle dynamic simulation on the assembly and release of siRNA/polymer/gold nanoparticles based polyplex. *AIChE Journal*, 64(3), 810-821.
- [102] Juan, S. C. C., Hua, C. Y., Chen, C. L., Sun, X., & Xi, H. (2005). Dissipative particle dynamics simulation of a gold nanoparticle system. *Molecular Simulation*, 31(4), 277-282.
- [103] Ryjkina, E., Kuhn, H., Rehage, H., Müller, F., & Peggau, J. (2002). Molecular Dynamic Computer Simulations of Phase Behavior of Non-Ionic Surfactants. *Angewandte chemie international edition*, 41(6), 983-986.
- [104] Z. S. Petrović, I. Javni, A. Waddon, G. Bánhegyi, Structure and properties of polyurethane–silica nanocomposites. *Journal of applied polymer science*, 2000, 76(2), 133-151.
- [105] K. Koseki, T. Arita, K. Tabata, T. Nohara, R. Sato, S. Nagano, A. Masuhara, Effect of Surface Silanol Density on the Proton Conductivity of Polymer-Surface-Functionalized Silica Nanoparticles. *ACS Sustainable Chemistry & Engineering*, 2021, 9(30), 10093-10099.
- [106] J. G. Croissant, K. S. Butler, J. I. Zink, C. J. Brinker, Synthetic amorphous

- silica nanoparticles: toxicity, biomedical and environmental implications. *Nature Reviews Materials*, 2020, 5(12), 886-909.
- [107] I. Gosens, J. A. Post, L. J. de la Fonteyne, E. H. Jansen, J. W. Geus, F. R. Cassee, W. H. de Jong, Impact of agglomeration state of nano-and submicron sized gold particles on pulmonary inflammation. *Particle and fibre toxicology*, 2010, 7(1), 1-11.
- [108] F. Mammari, E. Le Bourhis, L. Rozes, C. Sanchez, Mechanical properties of hybrid organic–inorganic materials, *J. Mater. Chem.*, 15 (2005), pp. 3787-3811
- [109] J. Lin, X. Wu, C. Zheng, P. Zhang, B. Huang, N. Guo, LY Jina, Synthesis and properties of epoxy-polyurethane/silica nanocomposites by a novel sol method and in-situ solution polymerization route, *Appl. Surf. Sci.*, 303 (2014), pp. 67-75.
- [110] S. M. Cakić, M. D. Valcic, I. S. Ristić, T. Radusin, M. J. Cvetinov, J. Budinski-Simendić, Waterborne polyurethane-silica nanocomposite adhesives based on castor oil-recycled polyols: Effects of (3-aminopropyl) triethoxysilane (APTES) content on properties. *International Journal of Adhesion and Adhesives*, 2019, 90, 22-31.
- [111] S. Zhang, M. Guo, Z. Chen, Q. H. Liu, X. Liu, Grafting photosensitive polyurethane onto colloidal silica for use in UV-curing polyurethane nanocomposites. *Colloids and Surfaces A: Physicochemical and Engineering Aspects*, 2014, 443, 525-534.
- [112] I. A. Rahman, V. Padavettan, Synthesis of silica nanoparticles by sol-gel: size-dependent properties, surface modification, and applications in silica-polymer

- nanocomposites—a review. *Journal of nanomaterials*, 2012, 8-8.
- [113] R. P. Bagwe, L. R. Hilliard, W. Tan, Surface modification of silica nanoparticles to reduce aggregation and nonspecific binding. *Langmuir*, 2006, 22(9), 4357-4362.
- [114] S. Hassanajili, M. Khademi, P. Keshavarz, Influence of various types of silica nanoparticles on permeation properties of polyurethane/silica mixed matrix membranes. *Journal of Membrane Science*, 2014, 453, 369-383.
- [115] S. Hassanajili, M. T. Sajedi, Fumed silica/polyurethane nanocomposites: effect of silica concentration and its surface modification on rheology and mechanical properties. *Iranian Polymer Journal*, 2016, 25, 697-710.
- [116] M. Cho, S. Yang, S. Chang, S. Yu, A study on the prediction of the mechanical properties of nanoparticulate composites using the homogenization method with the effective interface concept. *International journal for numerical methods in engineering*, 2011, 85(12), 1564-1583.
- [117] R. Hill, The elastic behaviour of a crystalline aggregate. *Proceedings of the Physical Society. Section A*, 1952, 65(5), 349.
- [118] B. Kim, J. Choi, S. Yang, S Yu, M. Cho, Influence of crosslink density on the interfacial characteristics of epoxy nanocomposites. *Polymer*, 2015, 60, 186-197.
- [119] B. Kim, J. Choi, S. Yang, S Yu, M. Cho, Multiscale modeling of interphase in crosslinked epoxy nanocomposites. *Composites Part B: Engineering*, 2017, 120, 128-142.
- [120] H. Zhang, H. Wang, W. Zhong, Q. Du, A novel type of shape memory polymer

- blend and the shape memory mechanism. *Polymer*, 2009, 50(6), 1596-1601
- [121] M. Aldas, E. Rayón, J. López-Martínez, M. P. Arrieta, A deeper microscopic study of the interaction between gum rosin derivatives and a Mater-Bi type bioplastic. *Polymers*, 2020, 12(1), 226
- [122] C. Li, S. L. Cooper, Direct observation of the micromorphology of polyether polyurethanes using high-voltage electron microscopy, 1990, *Polymer*, 31(1), 3-7.
- [123] L. M. Leung, J. T. Koberstein, Small-angle scattering analysis of hard-microdomain structure and microphase mixing in polyurethane elastomers. *Journal of Polymer Science: Polymer Physics Edition*, 1985, 23(9), 1883-1913.

국문 요약

형상 기억 폴리우레탄은 외부 열에 반응하여 가역적인 대변형이 발생하는 대표적인 스마트 소재로, 고분자 구조체 내부에 우레탄 결합을 포함한다. 고분자 재료의 비용 효율성, 경량성, 높은 변형률 및 가공성과 같은 장점들 때문에 센서나 액츄에이터, 바이오 재료 등 다양한 응용분야에 적용되고 있으며, 또한 낮은 기계적 물성을 보완하기 위해 나노입자를 첨가한 나노복합재 설계에 대한 연구도 활발히 진행되고 있다.

폴리우레탄 나노복합재의 열반응 형상 기억 효과를 얻기 위해서는 고분자 내 넷포인트와 분자 스위치라는 두 가지 구조적 조건이 필요하다. 물리적 얽힘, 공유 결합 또는 가교결합을 통해 본래의 모양을 기억하는 하드 세그먼트는 넷포인트 역할을, 전이 온도에서 폴리머 결정화와 같은 상 변화를 통해 형상을 복구시키는 유연한 소프트 세그먼트는 분자 스위치 역할을 한다. 두 가지 세그먼트의 물질은 본질적인 비호환성으로 인해 상분리가 일어나며, 그 비율에 따른 마이크로 구조변화는 고분자 시스템의 거동에 큰 영향을 미친다. 뿐만 아니라 고분자 매트릭스와 나노입자 사이의 화학적 비유사성으로 인한 나노입자 클러스터링 현상은 이전부터 나노복합재의 물성 개선을 위해 극복해야하는 과제로 주목받고 있다.

고분자 시스템의 구조-물성 관계를 해석하는 분자동역학 모델이나

나노입자 분포에 따른 기계적 특성을 해석하는 시뮬레이션 방법론들이 이전부터 연구가 진행되어 왔지만, 실제적인 나노복합재의 거동을 모사하고 설계하는 데에는 한계가 있었다. 이에 동기를 얻어 본 논문에서는 형상 기억 폴리우레탄 나노복합재의 고분자 결정화, 상분리 거동, 그리고 나노입자의 분포 해석을 종합적으로 모사하는 설계방법을 제시하고자 한다. 본 연구에서는 분자동역학 수준에서부터 메조스케일 시뮬레이션을 거쳐 연속체 스케일까지 이어지는 멀티스케일 해석을 수행하였다.

본 연구는 축소 분자동역학 모델을 구축하여 기존의 분자동역학 모델의 스케일의 한계를 극복하였다. 비드 모델을 통해 고분자 결정화 및 형상기억 사이클을 메조스케일 레벨에서 모사하여 고분자 내 각 세그먼트의 비율에 따른 폴리우레탄의 열-기계적 특성 및 나노입자 첨가 효과를 해석하였다. 이를 통해 실험에서 보고된 온도 및 분자조성에 따른 기계적 변형 트렌드를 정성적 및 정량적으로 비교하여 본 모델의 정합성을 검증하였다.

또한 소산 입자 역학 시뮬레이션 모델을 구축하여 폴리우레탄 나노복합재의 상분리 현상 및 나노입자 분포를 해석하였다. 분자레벨에서 계산한 각 물질들의 용해도를 해당 시뮬레이션의 매개변수로 사용하여, 세그먼트 비율에 따른 고분자의 위상 형태 및 나노복합재의 실제 나노입자 분포를 정확하게 예측하였다. 또한 실리카 나노입자에 추가적인 표면 처리 물질을 도입하여 최적의 나노입자 분포를 설계하고자 하였다.

그리고, 폴리우레탄 나노복합재의 상분리 모사를 통해 얻은 지오메트리를 그대로 반영한 연속체 모델을 구축하였다. 나노입자의 분산 정도에 따른 기계적 물성을 예측하기 위해 유한요소기반 균질화기법을 도입하였고, 본 논문에서는 이를 나노복합재의 다양한 형태를 설계할 수 있는 설계 방법론으로서 제시하였다.

본 논문에서 제시된 메조스케일 시뮬레이션 기반 멀티스케일 해석기법을 통해 앞으로 더 많은 연구가 진행되어 타겟 물성을 얻어내기 위한 실제 나노복합재 디자인 및 어플리케이션 응용에 활용될 수 있기를 기대한다.

Keywords

형상 기억 폴리우레탄, 나노복합재, 축소분자동역학, 메조스케일 시뮬레이션, 소산성 입자 역학, 나노입자 표면처리, 유한요소 균질화

Student Number : 2017-23073